A Study of the Excitation of Nucleon Resonances in Positive Pion Proton Interactions

by Gian Parkash Gopal

A thesis submitted for the degree of Doctor of Philosophy
in the University of London

Department of Physics,
Imperial College,
LONDON.

July 1970

ABSTRACT

This work describes an experimental study of positive pion proton interactions in the incident pion momentum range of 895 - 1040 MeV/c using the Saclay 82 cm. hydrogen bubble chamber. Accurate values of cross-sections for elastic scattering and single and double pion production reactions are presented.

A general discussion of the phenomenological methods employed to extract information about the nature of scattering of the incident partial waves from elastic scattering is given. The partial waves S1, P3 and D3 are reported to undergo resonant scattering in this energy region with the resonances having a strong inelastic decay. The work is mainly concerned with an attempt to determine the nature of inelastic scattering of the S1, P1, P3, D3, D5 and F5 partial waves from the experimental information obtained for single pion production - the dominant inelastic channel in this energy region.

Estimates obtained for the absorption parameters, η, for the partial waves are more accurate than those determined from studies of elastic scattering alone. The results of the analysis support the presence of resonant scattering in the S_{31}, P_{33} and D_{33} partial waves and provides evidence of considerable structure, of a resonant nature, in inelastic scattering for the P_{31} and D_{35} partial waves.

CONTENTS

CHAPTER 1

Study of Pion Nucleon Resonances

1.1 Introduction

A study of pion nucleon resonances can be undertaken in one of two ways.

(i) Formation Experiments. An incident pion with sufficient energy strikes a target nucleon at rest and excites it to a resonant state. The most basic manifestation of such resonance formation in the direct channel is the presence of structure in the variation of the total cross-section with energy. In the case of strong resonant scattering with negligible background sharp peaks are observed in the cross-section. The total positive-pion proton cross-section - Figure 1.1 - shows such a situation near a centre of mass energy of 1220 MeV corresponding to the Δ-resonance with $I = \frac{3}{2}$ and $J^P = \frac{3}{2}^+$. At higher energies the structure is more diffuse, showing a shoulder at around 1650 MeV, and a second broad peak at 1920 MeV. At these energies it seems likely that background scattering is at least of the same order of magnitude as resonant scattering. In situations where background scattering is appreciable the existence of possible resonant effects has to be deduced from a study of the final states.

A resonance excited in the direct ($\mathcal{s}$-) channel may be coupled to various inelastic final states besides the elastic one. However strongly inelastic the resonance may be, information about it can, in principle, be extracted from a study of elastic scattering using the formalism discussed in Section 1.2.

Inelastic decay modes provide another means of studying $\mathcal{s}$-channel resonances. Two-body, or quasi-two-body, decay modes are of particular interest in this respect. When one of the decay products is another resonance of lower mass we have a chain decay process.

(ii) Production Experiments. Resonances excited in the final state show up as enhancements in the invariant mass spectra of two or more particles in multiparticle final states. An enhancement not explained in terms of kinematic effects or statistical fluctuations is assumed to be caused by the decay of the resonance into the particles concerned.

A particularly interesting situation arises when a resonance produced in a final state is one of the decay products of a higher mass resonance excited in the direct channel in a formation experiment.

The present experiment, involving positive-pion proton interactions around the 'shoulder' region - that is, around c.m. energy 1610 - 1700 MeV, has the right conditions to initiate formation-and-production of pion nucleon resonances. From a study of elastic scattering the 'shoulder' in the total cross-section is deduced to result from the formation of two well-established, and one tentative, s-channel resonances which are highly inelastic. As such it should be possible to independently confirm their existence, and establish the quantum numbers, from a study of the inelastic channels. The dominant inelastic reactions in π^+p interactions over this energy range are the two single pion production processes

$$\pi^+ p \rightarrow \pi^+ p \pi^0 \qquad (1)$$

and $$\pi^+ p \rightarrow \pi^+ n \pi^+ \qquad (2)$$

We discuss briefly the formalisms used to explain the features, as observed in earlier experiments, of these reactions in Section 1.3. Section 1.4 attempts to justify doing yet another experiment in this energy range.

1.2 Elastic Scattering

At the low energies we are dealing with, it is feasible to study pion-nucleon elastic scattering in terms of the individual angular momentum waves taking part in the scattering and to decide which, if any, resonate. This is undertaken as a partial wave analysis where the original plane wave -

e^{ikz}, where k is the incoming momentum in the centre of mass (units with $\hbar = c = 1$), - is transformed by the scattering centre into a wave represented asymptotically (neglecting spin effects) by

$$e^{ikz} + f(\theta)\frac{e^{i\underline{k}.\underline{r}}}{r} \qquad (1.1)$$

The first term is the unscattered plane wave and the second is the outgoing spherical wave where θ is the centre of mass scattering angle and $f(\theta)$ is the scattering amplitude. By writing out both the incoming plane wave and the scattered wave as a sum of Legendre polynomials we can derive a series expansion for the scattering amplitude in terms of the various partial wave amplitudes

$$f(\theta) = \sum_{l=0}^{\infty} (2l+1)\, a_l\, P_l(\cos\theta) \qquad (1.2)$$

where a_l is the amplitude of the wave with orbital angular momentum l. For purely elastic scattering we can express a_l in terms of a real phase shift δ_l.

$$a_l = \frac{e^{2i\delta_l} - 1}{2ik} \qquad (1.3a)$$

In the presence of inelastic scattering the phase shift is no longer real. So we write

$$a_l = \frac{e^{2i(\delta_l + i\gamma_l)} - 1}{2ik}$$

$$= \frac{e^{-2\gamma_l} . e^{2i\delta_l} - 1}{2ik}$$

$$= \frac{\eta_l e^{2i\delta_l} - 1}{2ik} \qquad (1.3b)$$

Unitarity requires that

$$|a_l| \leq 1/k$$

This implies that the absorption coefficient, η_l, is bounded.

$$0 \leq \eta_l \leq 1$$

The differential cross-section for elastic scattering is given by

$$\frac{d\sigma}{d\Omega} = |f(\theta)|^2 \tag{1.4}$$

and it is easy to show that the total elastic cross-section is

$$\sigma_{el} = 4\pi \sum_l (2l+1) \, |a_l|^2 \tag{1.5a}$$

The total inelastic cross-section is given by

$$\sigma_{inel} = \frac{\pi}{k^2} \sum_l (2l+1)(1-\eta_l^2) \tag{1.5b}$$

and thus the total cross-section is

$$\sigma_{tot} = \frac{4\pi}{k} \sum_l (2l+1) \, Im(a_l) \tag{1.5c}$$

In the case of spin 0 - spin $\frac{1}{2}$ scattering we have to consider two scattering amplitudes. These are the spin non-flip and the spin flip amplitudes. The overall scattering amplitude is written as follows

$$M = f(\theta) + ig(\theta) \, \underline{\sigma} \cdot \underline{n} \tag{1.6}$$

where $f(\theta)$ is the spin non-flip amplitude and $g(\theta)$ the spin flip amplitude. $\underline{\sigma}$ is the Pauli spin matrix for spin $\frac{1}{2}$ and $\underline{n}$ is the normal to the scattering plane, given by

$$\underline{n} = \frac{\vec{k_i} \times \vec{k_f}}{|\vec{k_i} \times \vec{k_f}|} \tag{1.6a}$$

where $\underline{k_i}$ and $\underline{k_f}$ are the initial and final centre of mass momenta.

The partial wave expansions for $f(\theta)$ and $g(\theta)$ can be readily obtained as

$$f(\theta) = \sum_{l} \left[(l+1)a_{l+} + l a_{l-}\right] P_l(\cos\theta) \qquad (1.7)$$

and

$$g(\theta) = \sum_{l} (a_{l+} - a_{l-}) \sin\theta \, P_l'(\cos\theta) \qquad (1.8)$$

where a_{l+} and a_{l-} are the scattering amplitudes for the partial waves with orbital angular momentum l and total angular momentum $J = l + \frac{1}{2}$ and $l - \frac{1}{2}$ respectively and

$$P_l'(\cos\theta) = \frac{d}{d(\cos\theta)} P_l(\cos\theta)$$

In assuming that $a_{l+} \neq a_{l-}$ we are assuming that spin dependent forces take part in the scattering. The differential cross-section is then given by

$$\frac{d\sigma}{d\Omega} = |f(\theta)|^2 + |g(\theta)|^2 \qquad (1.9)$$

and the total elastic cross-section is

$$\sigma_{el} = \frac{4\pi}{k^2} \sum_{l=0}^{\infty} \left[(l+1)|a_{l+}|^2 + l|a_{l-}|^2\right] \qquad (1.10)$$

So, for each partial wave there are in all four parameters to describe the scattering amplitude. These are δ_{l+}, δ_{l-}, η_{l+} and η_{l-}.

A determination of these parameters for all contributing partial waves starts with experimental differential cross-section distributions. A unique determination cannot, however, be made due to the Minami Ambiguity where by a transformation $f(\theta) \leftrightarrow g(\theta)$ the differential cross-section remains unchanged. Additional information required to resolve this is the polarisation ($\underline{P}$) of the final state spin $\frac{1}{2}$ particle. It is easy to show (via (1.7), (1.8) and (1.9) that

$$\underline{P} \frac{d\sigma}{d\Omega} = -2\,\mathrm{Im}\left[f^*(\theta)\, g(\theta)\right] \underline{n} \qquad (1.11)$$

and this quantity changes sign under the Minami transformation. This leaves one more ambiguity to resolve - the Generalised Yang Ambiguity[1]. The difficulties introduced by this are usually overcome by a knowledge about the threshold of the $l = 1$ partial wave[2]. So if at least one partial wave is uniquely determined it is used as a fixed reference for the higher partial waves as they appear at higher energies.

The differential cross-section distribution and the polarisation distribution are usually fitted to Legendre polynomial expansions of the type

$$\frac{d\sigma}{d\Omega} = \frac{1}{k^2} \sum_{l=0}^{2l_{max}} C_l P_l (\cos\theta) \tag{1.12}$$

and

$$P \frac{d\sigma}{d\Omega} = \frac{\sin\theta}{k^2} \sum_{l=0}^{2l_{max}} D_l P_l' (\cos\theta) \tag{1.13}$$

The Legendre polynomial coefficients C_l and D_l are related via (1.9) and (1.11) to the scattering amplitudes a_{l+} and a_{l-} up to $l = l_{max}$ where l_{max} is the order of the highest partial wave deemed to make a significantly non-zero contribution to the scattering. A table setting out this relationship can be found in reference 3).

Partial wave analysis of pion-nucleon interactions can be tackled in one of two ways. Either an energy dependent analysis can be performed by parametrising the partial amplitudes as functions of energy and fitting to all data at all the available energies, or an energy independent analysis can be performed by searching extensively at each energy for different solutions that give a statistically acceptable fit to the data at that energy and then imposing continuity on these solutions for different energies to select the most likely among the solutions found.

The former approach depends on a close study of the energy variations of the coefficients C_l and D_l to deduce which of the partial waves are most likely to have resonant solutions and which can be treated as non-resonant background. Roper et al[4] parametrised the partial wave amplitudes as a combination of resonant and non-resonant forms - viz.

$$a_{l\pm} = \varepsilon_{l\pm} a_{l\pm} \text{ (res)} + a_{l\pm} \text{ (non-res)} \tag{1.14}$$

where
$$a_{l\pm} \text{ (res)} = \frac{\frac{1}{2}\Gamma_{l\pm}^{el}}{(\omega_{l\pm}^{R} - \omega) - \frac{1}{2}i\,\Gamma_{l\pm}^{(t)}} \tag{1.15}$$

$\Gamma_{l\pm}^{el}$ is the resonance elastic width and $\Gamma_{l\pm}^{(t)}$ is the resonance total width. Specifically $\varepsilon_{l\pm}$ was set to 1 for those partial waves that were considered to be purely resonant and 0 for those that were considered to be purely non-resonant. The non-resonant amplitude is given by

$$a_{l\pm} \text{ (non-res)} = \frac{\eta_{l\pm} e^{2i\delta_{l\pm}} - 1}{2ik} \tag{1.16}$$

with $\delta_{l\pm}$ and $\eta_{l\pm}$ parametrised by

$$\tan \delta_{l\pm} = k^{2l+1} \sum_{n=0}^{l_{max}-l} (A_{l\pm})_n \, k^n \tag{1.17a}$$

or
$$\delta_{l\pm} = k^{2l+1} \sum_{n=0}^{l_{max}-l} (A_{l\pm})_n \, k^n \tag{1.17b}$$

if the phase shift approaches 90°,

with
$$\eta_{l\pm} = e^{-2V_{l\pm}} \tag{1.17c}$$

with $V_{l\pm} = 0$ for $k < k_T$ - i.e. for a purely elastic partial wave (k_T being threshold pion momentum for one-pion production) and for $k \geq k_T$

$$V_{l\pm} = (k - k_T)^{2l+1} \sum_{n=0}^{l_{max}-l} (B_{l\pm})_n \, (k - k_T)^n \tag{1.17d}$$

There are thus $2(l_{max} + 1)^2$ A parameters and an equal number of B parameters. Unitarity requirements impose the conditions

$$-\frac{1}{2k} \leq Re\,(a_{l\pm}) \leq \frac{1}{2k}$$

and $0 \leq Im(a_{l\pm}) \leq \frac{1}{k}$ for partial waves which are purely or partially resonant, over and above the restriction $0 \leq \eta_{l\pm} \leq 1$. This parametrisation ensures the correct threshold behaviour for the partial wave amplitudes but has the disadvantage of allowing no correlation[5], in their energy dependence, between $\delta_{l\pm}$ and $\eta_{l\pm}$.

A solution is found by minimising the quantity

$$M = \sum_{\text{all energies}} \sum_{\text{at each energy}}^{\text{all data}} \left(\frac{X^e - X^c}{\Delta X^e} \right)^2 \qquad (1.18)$$

where X^e is the experimental quantity and X^c is the calculated quantity for given values of the parameters and ΔX^e is the experimental error in X^e. Other energy dependent parametrisations can be considered, for example the non-resonant partial wave amplitudes $a_{l\pm}$ could be parametrised directly as functions of energy and the phase shifts and the absorption parameters calculated from the best values obtained for the partial wave amplitudes, for

$$\delta_{l\pm} = \tfrac{1}{2} \tan^{-1} \left[\frac{2k\, Re(a_{l\pm})}{1 - 2k\, Im(a_{l\pm})} \right] \qquad (1.19)$$

and

$$\eta_{l\pm} = 2k \left[(Re(a_{l\pm}))^2 + \left(\frac{1}{2k} - Im(a_{l\pm})\right)^2 \right]^{\frac{1}{2}} \qquad (1.20)$$

The second type of approach, used more widely nowadays, is the energy independent approach. In this case no a priori assumptions about the energy variation of the partial wave amplitudes are imposed. On the contrary, the existence of certain resonant partial wave states is discovered from the solutions obtained. An extensive search is made at each energy minimising the quantity M for all data at this energy. In most cases no single unique solution is found, but a range of solutions that are all equally statistically acceptable are obtained. The procedure then is to impose some form of continuity between the solutions at different energies for each partial wave. The various exponents of this technique[6], [7], [8], [9] differ in the manner they impose continuity to decide among the solutions. Saclay[7] imposed continuity on their solutions by eye. This may seem to be rather arbitrary but in the absence of an exact model for the energy dependence of the amplitudes the final result may not be too far off from the exact picture. This is supported by the large amount of agreement between their results and those from more sophisticated analyses.

The Berkeley analysis[8] removes some of this arbitrariness by using 'the shortest path' technique for imposing continuity. Since this gives an exact definition to the form of the continuity the method is available for a computer based choice of the final solution. From all the solutions for all partial waves at all the energies $(k_1 - k_n)$ a search is made for the smallest value of the quantity

$$X(k_1, k_2, \ldots k_n) = \left\{ \sum_{i=1}^{n} \sum_{l,J} \sum_{k=1}^{K_i} (J+\tfrac{1}{2}) \times \times \left| a_i^k(l,J) - a_{i-1}^k(l,J) \right|^2 \right\}^{1/2} \tag{1.21}$$

where K_i is the number of solutions at the i^{th} energy, l and J are the orbital and total angular momenta specifying the partial wave.

A more sophisticated approach has been adopted by the CERN group[6]. Here, instead of demanding any specific pattern of energy dependence of the amplitudes, one demands that the energy dependence of the amplitudes should be such as to satisfy "dispersion relations" between the real and imaginary parts of the amplitudes. A full description of this technique and the assumptions that have to be invoked for pion - nucleon case is given in (10). With this method one would calculate the experimental partial wave amplitudes from the data using random starting points and fit the results to the dispersion relation and arrive at a starting value for the dispersion relation result. If the experimental and dispersion relation results are not consistent an iterative procedure is used to arrive at a more consistent set. Failing convergence of the fit the experimental partial wave amplitudes are recalculated using the last solution as the starting values. The process is repeated until self-consistency is achieved. One, thus, obtains two sets of solutions for each partial wave - one experimental set and one dispersion relations set. It has recently been pointed out by C. Lovelace[11] that the latter set is a smoothed out set and hence quite a bit of the structure observed in the experimental data is likely to have been lost in the smoothing process.

Results from partial wave analyses are generally presented in two forms. The first is a set of plots of the phase shifts and absorption parameters of the partial waves involved as function of energy - as shown in Figure 1.3 for the partial waves S_{31}, P_{33}, and D_{33} (the notation used being the usual $l_{2I,\ 2J}$) from reference 6). The second form is the presentation of the real and imaginary parts of the actual partial wave amplitude on an Argand diagram where one plots kRe $(a_{l\pm})$ against kIm $(a_{l\pm})$ for the various energies - Figure 1.9 shows the amplitudes for the same three partial waves from the same source. This form of representation is generally preferred because it is more illustrative as to the behaviour of the partial wave concerned when looking for possible resonant scattering in the partial wave.

From (1.3b) we get

$$k \operatorname{Re} a_{l\pm} = \tfrac{1}{2}\eta_{l\pm} \sin 2\delta_{l\pm}$$

and
$$k \operatorname{Im} a_{l\pm} = \tfrac{1}{2}(1 - \eta_{l\pm} \cos 2\delta_{l\pm}) \tag{1.22}$$

Since $\eta_{l\pm}$ is bounded this implies that $ka_{l\pm}$ is bounded by a circle with centre $(0, \frac{1}{2})$ and radius $\frac{1}{2}$ - Figure 1.4a. For the upper limit of $\eta_{l\pm} = 1$ the amplitude lies on the circle and for $\eta_{l\pm} < 1$ it lies inside the circle. If a partial wave resonates, and is purely elastic ($\eta = 1$), then the amplitude goes through a maximum and the phase shift goes through $\pi/2$. The behaviour of the amplitude is then described by

$$ka = \frac{1}{(E_r - E)\,2/\Gamma - i} \tag{1.23}$$

This gives rise to

$$\sigma_{el} \sim \frac{\Gamma^2}{(E_r - E)^2 + \Gamma^2/2} \tag{1.24}$$

This is the Breit-Wigner formula with Γ as the full width of the resonance of mass E_r. Writing $\varepsilon = \dfrac{2(E_r - E)}{\Gamma}$ we have

$$Re\,(ka) = \frac{\varepsilon}{1+\varepsilon^2}$$

and
$$Im\,(ka) = \frac{1}{1+\varepsilon^2} \qquad (1.25)$$

which implies that (ka) lies on a circle of radius $\frac{1}{2}$ and centre $(0, \frac{1}{2})$. With increasing energy (E) the amplitude point moves round the boundary circle in a counter-clockwise direction. In the general case a resonance is coupled to more than one channel and so its full width must describe its decay into all possible decay channels. Hence we have $\Gamma = \Gamma_{el} + \Gamma_{reaction}$ and we define the elasticity of the resonance by $x = \Gamma_{el}/\Gamma$. Then the elastic amplitude is given by

$$ka = \frac{x}{\varepsilon - i} \qquad (1.26)$$

The amplitude still describes a circle with energy on the Argand diagram but now its radius becomes x and centre (0, x/2) - Figure 1.4. So if $x \leqslant \frac{1}{2}$ the circle never passes above the line Im (ka) $= \frac{1}{2}$ and as such $\delta = 0^\circ$ and not $\pi/2$. The elasticity x of a resonance is related to the absorptivity of the resonating partial wave. If the phase shift passes through 90° $\eta = 2x - 1$, whereas for the phase shift going through 0°, $\eta = 1 - 2x$.

It is extremely rare, in practice, to find a purely elastic resonance or to find a partial wave that scatters via a resonance alone. One generally finds that resonance scattering is superimposed on "background" scattering which has its own energy dependence. The effect of this is to shift the centre of the resonance circle away from the imaginary axis and to distort the counter-clockwise circular energy dependence of resonance scattering considerably. The Argand diagrams for the S_{31}, the P_{33} (which has one pure elastic resonance - the 1238 N^* - and one highly inelastic resonance) and the D_{33} (Figure 1.3) show just such effects.

After having determined the various partial wave amplitudes over a wide energy range one has to interpret the results by appropriately parametrising the "background" scattering in each of the partial waves to extract the presence of any resonant scattering and thus deduce the quantum numbers for the resonances present. Table 1.1[10] presents the I = 3/2 resonances, deduced by various phase shift analyses, mentioned and their proposed quantum numbers.

1.3 Single Pion Production

Below, and around, the incident pion momenta of 1 GeV/c the main inelastic channels in positive pion proton interactions are the two single pion production channels - (1) and (2). The cross-sections for these two channels at various energies around 1 GeV are shown in Figures 3.7 and 3.8 (see Chapter 3). The striking feature is the rapid rise of the cross-section for (1), whereas the cross-section for (2) rises less rapidly, from the threshold kinetic energy of around 300 MeV in the laboratory. The next feature of interest in pion production reactions appears in plots of the 2-body effective mass distributions. As will be seen in the data from the present experiment these are dominated by the Δ resonance with mass 1238 MeV/c^2 and with I = 3/2 and J = 3/2. As a result the various models proposed to explain the 3-body final states have assumed that the final state results from the decay of an intermediate quasi-two-body state - the $\pi \Delta_{3,3}$ state. The earliest model based on this assumption was the "Isobar Model" proposed by Lindenbaum and Sternheimer[12].

The basic assumptions of this model were as follows:-

(i) The process $\pi N \rightarrow \pi_1 \pi_2 N$ is a combination of two processes $\pi N \rightarrow \pi_1 \Delta^2_{33}$, the upper suffix on the Δ indicates the pion that couples with the nucleon to form the nucleon isobar, and $\pi N \rightarrow \pi_2 \Delta^1_{33}$. The isobars are assumed to be produced isotropically.

(ii) In determining the intensities and the three-body final state distributions it is assumed that the processes add incoherently.

(iii) It is assumed that the pion recoiling off the excited nucleon isobar is energetic enough to have moved out of the range of interaction before the isobar breaks up.

(iv) The intensity of Δ_{33}^{i} (i = 1, 2) excitation is assumed to be proportional to the π - N total cross-section in the appropriate I-spin state and at the appropriate centre of mass energy (equal to the coupled π - N invariant mass).

(v) The excited isobar is assumed to decay isotropically.

The model is able to explain qualitatively the two pion-nucleon invariant mass distributions but gives poor agreement with the two-pion mass distribution Moreover the model predicts a fixed value, with energy, for the ratio (R) between the cross-sections of channels (1) and (2). The angular distributions for the final state particles are inherently predicted to be isotropic, in contradiction to the observed distributions.

Bergia, Bonsignori and Stanghellini[13)] proposed an extension of this model which gives slightly better agreement with experiment as far as the energy distributions of the final state particles is concerned. All the assumptions of the Lindenbaum-Sternheimer model are retained with the exception of the assumption that the two isobar excitation processes add incoherently. Interference effects are thus introduced between the two constituent processes. Although this better explains the energy distribution of the final state particles the model still does not contain any physical concepts that explain the observed non-uniform angular distributions and the energy variation of R.

Olsson and Yodh[14)] argue that since the spin of the 1238 MeV isobar is $^3/_2$ it is unrealistic to assume, in any model attempting to explain single pion production in terms of the production of an isobar and its subsequent decay, that the isobar decays isotropically. So they modify the Lindenbaum - Sternheimer model by assuming that the decay of the isobar is a P-wave decay. The assumption of isotropic (S-wave) production of the isobar is still retained and the two isobar production processes are assumed to add coherently. The real amplitude for Δ production is the only free parameter in the model and this may be energy dependent. At a single fixed energy it is just a factor in the overall normalisation. With this model Olsson and Yodh are thus able to explain the observed energy distributions of the final state particles reasonably well. Assuming that the amplitude for Δ production is uniform over the energy region the model also predicts a slow variation of the ratio R with energy around a value of above 5. This is again an improvement on the previous isobar models.

S-wave (isotropic) production of the Δ, as assumed in all the models described above, implies that initial pion-nucleon state is assumed to be a D-wave state. However, results from phase shift analyses, as described earlier, indicate that the S, P, D partial waves and, perhaps, the $J = {}^5/_2$ F wave are inelastic around 1 GeV. So it is highly unlikely the all single pion production (the dominant inelastic channel around this energy) is due to D-wave scattering alone in the initial state. The general non-relativistic formalism to separate out the angular dependence of the reaction $\pi N \rightarrow \pi_1 \pi_2 N$, assuming that the three body final state is produced via a quasi- two-body intermediate state in a given partial wave, has been set out by Ciuli and Fischer[15]. In the general case we need to consider three types of possible intermediate states that give rise to the $\pi_1\pi_2 N$ final state. These are:

(a) $\pi N \rightarrow (\pi_1\pi_2)\ N$ .... boson-boson coupling

(b) $\pi N \rightarrow \pi_1\ (\pi_2 N)$)

(c) $\pi N \rightarrow \pi_2\ (\pi_1 N)$) .... boson-nucleon coupling

The multiplicity of such intermediate states depends on the number of different couplings (isobars) that are possible at a given centre of mass energy.

In the later modifications[16] to their model, Olsson and Yodh use this formalism to get better agreement with experiment, especially with respect to the production angle distributions of the final state particles. In doing so the possibility of boson-boson isobars is excluded as the lowest well-

established pion-pion resonance is the ρ(I=1, J=1) resonance at 765 MeV. The laboratory threshold energy for the excitation of this isobar, at its central mass, is well above the energy region under consideration. However, two possible attractive pion-nucleon couplings are considered -
(i) the I = $^3/_2$, J = $^3/_2$ Δ (1238) resonance and (ii) the I = $\frac{1}{2}$, J = $\frac{1}{2}$ S-wave re-scattering effect. The partial waves considered are the $P_{\frac{1}{2}}$ and $D_{5/2}$ and it is assumed that the former contributes only to the $\pi(\pi N)_{I=\frac{1}{2}, J=\frac{1}{2}}$ rescattered final state and the latter to the $\pi\, \Delta_{33}$ final state. So both the final states are in the S-wave. With constant values (obtained by fitting the experimental data) for the amplitudes for the two final states good fits are obtained to the overall energy variation of the cross-section for channels (1) and (2) and the energy distributions of the final state particles at various incident pion energies. This restricted model, however, failed to give good agreement to the angular distributions of the final state particles. Agreement to these were improved by the later[17] introduction of the P-wave production amplitude of the Δ_{33} (1238).

Namyslowski et al[18] using the three particle relativistic angular momentum states of Wick[19] have given a general partial wave expansion of the cross-section for three particles between which only two particle interactions take place. Deler and Valladas[20] have developed a similar formalism for the case of two spinless and one spin - $\frac{1}{2}$ particles. This formalism is similar to that developed by Ciuli and Fischer[15] with relativistic effects taken into account. A more detailed discussion of this formalism is presented in Chapter 5.

1.4 Need for a high statistics Bubble Chamber experiment

As has been described the overall cross-section for interactions shows a shoulder in the centre of mass energy region 1600 - 1700 MeV. From phase shift analysis of elastic scattering it has been ascertained that this is due to the existence of three I = $^3/_2$ nucleon resonance in this mass region.

The cross-section ($\sim$21 mb.) splits up nearly equally between the elastic and the inelastic channels. Hence more information can be obtained from a detailed study the dominant inelastic channels than has been obtained from phase shift analysis of the elastic channel alone - particularly, the inelasticity parameters for the various partial waves could be better determined. However, in the elastic channel itself the effects of the proposed resonances, if present, should be most clearly manifested in the backward (centre of mass scattering angle = 180°) direction. The data used in the various phase shift analysis have predominantly come from various counter experiments[21]. Although the accuracy of the differential cross-sections is good over most of the centre-of-mass scattering angle range, it is poor (absolute error in the differential cross-section is greater than $\pm$ 0.1) in the backward direction. It is in the backward direction that a bubble chamber experiment can hope to improve the data in the elastic channel.

For the single pion production reactions only bubble chamber experiments can hope to extract all the physical quantities for the three final state particles. The experimental data used by Olsson and Yodh came from low statistics bubble chamber experiments[22] with a statistical accuracy of the order of $\pm$ 5% and $\pm$ 12% in the overall channel cross-section for channels (1) and (2) respectively. As such any effects in single pion production processes that are of the order of a few per cent would not be detected. So the data was explained reasonably well by a judicious choice of a couple of partial waves only, in spite of the evidence from phase shift analysis that the S_{31}, P_{31}, P_{33}, D_{33}, D_{35}, and F_{35} partial waves are all reasonably inelastic. To determine the contribution of each of these partial waves one has to use experimental data that is, at least, an order of magnitude better in statistics than that used in the Olsson and Yodh fits. A description of just such an experiment is presented in the ensuing chapters.

Table 1.1

Resonating Pion Nucleon Partial Waves with $I = 3/2$

Wave $(L_{2I}, 2J)$	Ref: CERN TH838			Ref: A. Donnachie - Vienna Conference 1968		
	Mass (MeV)	Width (MeV)	Elasticity	Mass (MeV)	Width (MeV)	Elasticity
P_{33}	1236	125	1.0	1236	125	1.0
S_{31}	1635	177	0.284	1630	160	0.27
P_{33}	1688	281	0.098	1690	280	0.10
D_{33}	1691	269	0.137	1670	225	0.13
F_{35}	1913	350	0.163	1880	250	0.18
P_{31}	1934	339	0.299	1905	300	0.25
F_{37}	1946	221	0.386	1940	210	0.42

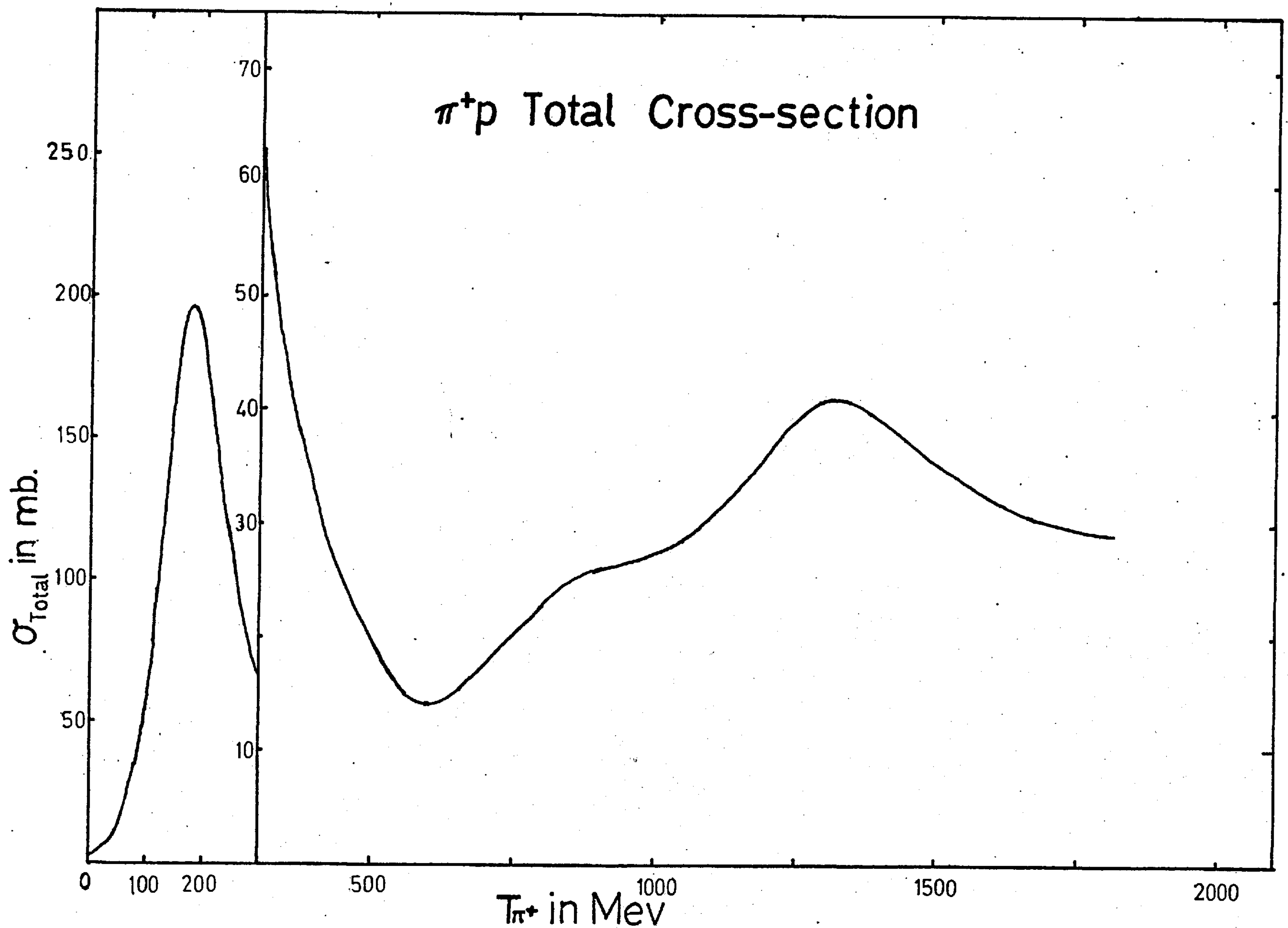
π^+p Total Cross-section
σ_{Total} in mb.
250
200
150
100
50
70
60
50
40
30
10
0
100
200
500
1000
1500
2000
T_{π^+} in Mev

Fig. 1·1

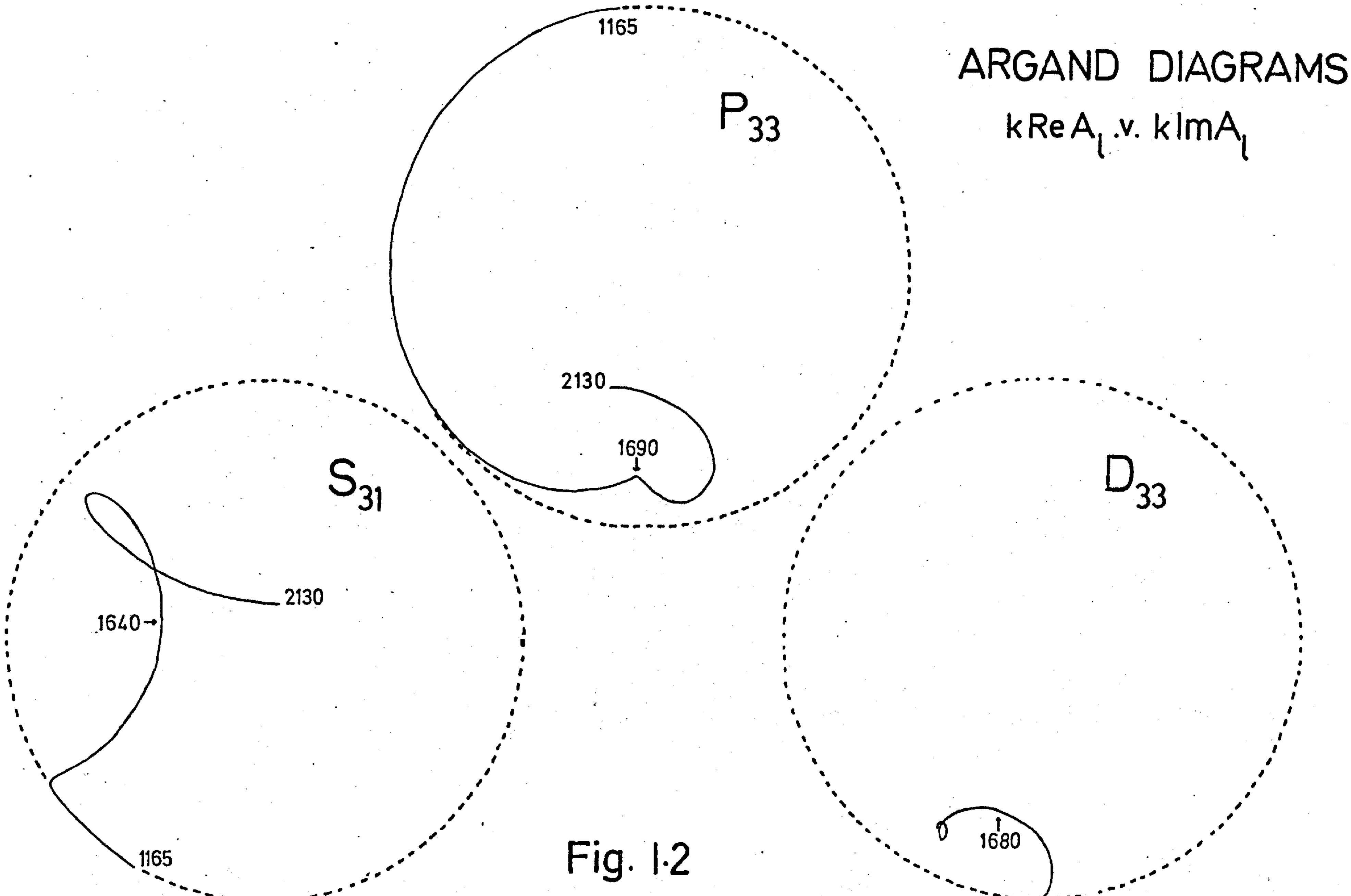
ARGAND DIAGRAMS
kRe A$_l$ .v. k Im A$_l$
P$_{33}$
1165
2130
1690
S$_{31}$
2130
1640
1165
D$_{33}$
1680

Fig. 1·2

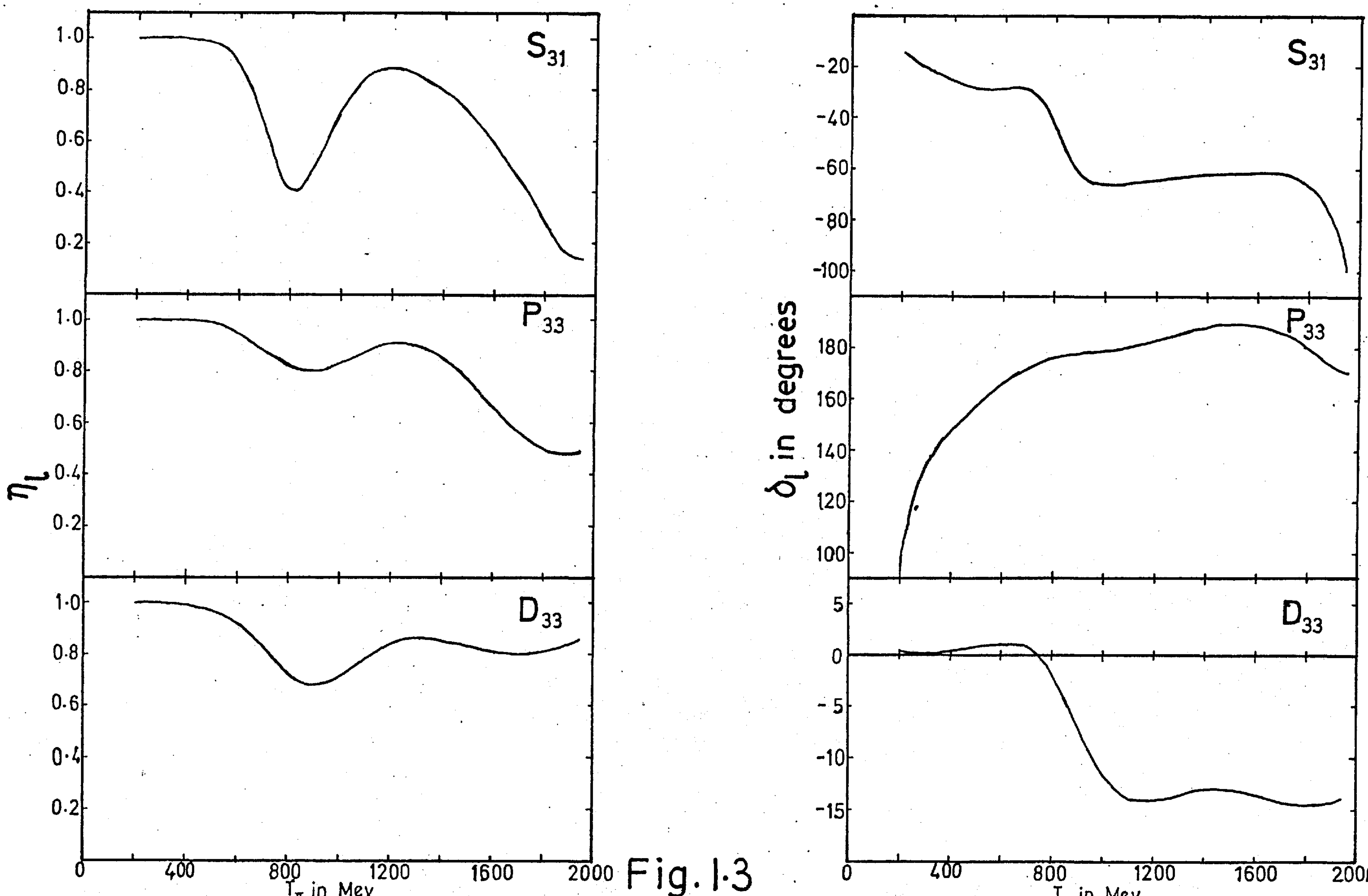

S31
P33
D33
1·0
0·8
0·6
0·4
0·2
ηl
0
400
800
1200
1600
2000
Tπ in Mev
-20
-40
-60
-80
-100
180
160
140
120
100
5
0
- 5
-10
-15
δl in degrees

Fig. I·3

$$T = \frac{X}{\varepsilon - i} \quad \text{with } \varepsilon = \frac{2(E-E_0)}{\Gamma} \quad \text{and} \quad X = \frac{\Gamma_{el}}{\Gamma}$$

- - - - - Unitarity Circle

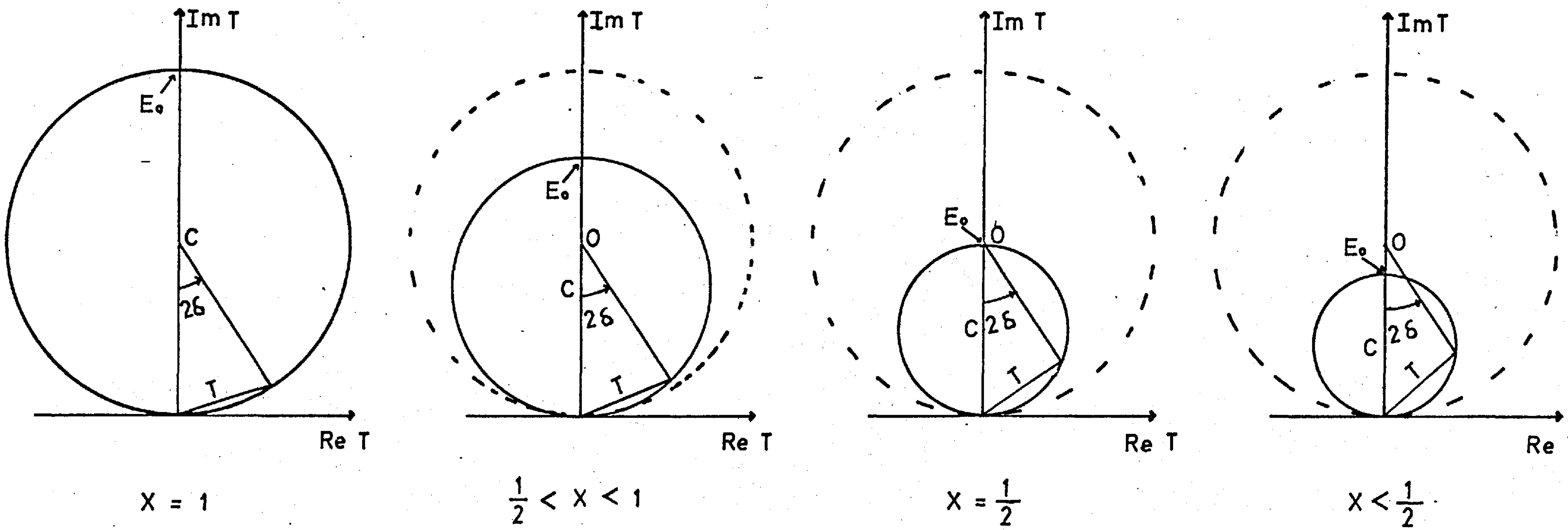

Fig. 1·4

CHAPTER 2

Experimental Apparatus and Data Processing

2.1 Introduction

The Saclay 81 cm. hydrogen bubble chamber was exposed to a beam of positive pions, in the momentum range 0.9 - 1.05 GeV/c, from the K1 beam line at the Rutherford High Energy Laboratory in 1966. Approximately 25,000 pictures, with about 15 pions per picture, were obtained at each of the incident momenta - 895, 945, 995 and 1040 MeV/c. The percentage of protons in the beam was negligibly small. There was a substantial but indeterminate muon contamination in the beam. However, as the experiment was not designed to measure absolute cross-sections, this is of no consequence. A brief description of the chamber and the K1 beam line is given in Section 2.2.

An expected interaction rate of two in every three frames implies a huge amount of raw information that has to be put through an elaborate data-reduction process. The first stage of this process is the compilation of a complete, as far as possible, list (the scan list) of all interactions on the film. The scan list for each momentum was obtained by performing two independent scans followed by a check scan. Section 2.3 describes the scanning procedure adopted.

Each interaction on the scan list has to be measured and the measurements processed to reconstruct the interaction in space. All possible interpretations, in terms of mass assignments to the particles producing the tracks, have then to be tried to check that the values of the track variables are consistent with energy-momentum conservation. Interpretations succeeding this check have then to be checked for consistency with the observed bubble densities of the tracks. An elaborate book-keeping system is necessary to keep track of the event through all these stages of processing. An efficient book-keeping system should: (i) at the end of each measuring-processing-interpretation pass give information about the success or failure of the event at each of the important stages of processing and (ii) at the end of the experiment make it possible to select the various interactions involved and to extract information about the scanning efficiencies for them.

With the original scan list on magnetic tape, a computer controlled book-keeping system can control each stage of the processing and update the scan list at the end of it. Alternatively the scan list is used to generate a list of events to measure at the beginning of each pass and is updated at the end of the pass with information about either the final interpretation, if successfully obtained, of each event, or the first stage at which the event encountered difficulties in the processing system. The latter procedure was adopted in the present experiment. A detailed description of the system is given in Sections 2.3 to 2.5. The complete processing system is schematically shown in Figure 2.2. Section 2.4 describes the measuring machines and the measuring procedure adopted and Section 2.5 contains a brief description of the reconstruction and kinematic fitting processes. Finally, the procedure used for the selection of the most likely physical interpretation of each event and the updating of the scan list is described in Section 2.6. A brief description of the final data summary tapes concludes this chapter.

2.2 The Saclay Chamber and the K1 Beam Line

The Saclay hydrogen bubble chamber was built in its original 50 cm. version in 1960 and was modified to its present dimensions of 81 x 40 x 51 cm^3 in 1964. A system of three flash tubes and vertical cylindrical condenser lenses is used to illuminate approximately 165 litres of sensitive liquid. This sensitive volume was photographed on semi-perforated film by three stereoscopic cameras arranged in an isosceles triangle, of base 47.8 cm. and height 36.1 cm., situated at a mean distance of 172.1 cm. away from the front glass-liquid interface. The fiducial marks, necessary for stereoreconstruction of interactions inside the chamber, are inscribed on the liquid side of the front and back glass windows. A mean magnetic field of 19.538 kilo Gauss was superimposed across the chamber in the direction of the cameras to ensure that the positive pion beam is deflected towards the centre of the chamber after entry through the beam window. The magnetic field was maintained at this mean value throughout the run to within $\pm$ 0.002%.

The K1 beam line, nearly 55 m. in length, was laid out at the Rutherford Laboratory to provide beams of charged π or k mesons of incident momenta up to 2.2 GeV/c for the Saclay hydrogen bubble chamber. The beam line, shown schematically in Figure 2.1, can be considered to be made up of four stages.

The first stage defines the phase space (area of target x solid angle accepted) acceptance. The angular acceptance in the vertical and horizontal directions is defined by the slits CV1 and CH1 respectively. CH1, coupled with the 20° deflecting magnet M1, defines the initial momentum bite. The doublet of quadrupole magnets Q_0 and Q_1 are used to focus and defocus the beam before the 20° deflection by M1.

The next two stages, almost identical in their components, are the stages where the particles undergo electrostatic separation. Each redefines the momentum bite by a bending magnet (M2 or M3) followed by a vertical collimator (CH2 or CH3). The particles are injected into and extracted from the electrostatic separator (VS1 or VS2) by a pair of vertical sweeping magnets (VM1/VM2 or VM3/VM4). In each stage the particles are first focussed by a pair of quadrupoles (Q_0 - Q_1 or Q_5 - Q_6) and then refocussed by another pair of quadrupoles (Q_3 - Q_4 or Q_7 - Q_8) on to the mass selecting horizontal slits (CV2 or CV3). In each case the separation of the wanted particles from the unwanted ones is brought about by a 'parallel' separation system. In this system the separators impose a strong electric field across the beam axis. Since there is no magnetic field to compensate for the deflection due to this field the separator is made up of sections tilted to follow the path of the wanted particles. The first separator in the K1 beam line (VS1) consisted of two sections while the second (VS2) had three sections - each section being 10 ft. long. After emerging from the separator the focussing quadrupoles (Q_3 - Q_4 or Q_7 - Q_8) are used to focus the separated beam of wanted particles on to the mass selecting slit (CV2 or CV3).

In the final stage quadrupole magnets Q_9 and Q_{10} are used to produce a vertically divergent beam. The vertical bending magnet VM5 is used to steer the beam on to the chamber window.

A set of scintillation counters (M and S1 - S6) are judiciously placed along the beam line to assist in 'tuning' the beam. 'Tuning' consists of obtaining a focussed image of the internal target on the final 'mass slit' - CV3. The magnet currents are initially set at values calculated from the beam optics. These values do not generally give a focussed beam due to errors in alignment of the beam components. Focussing is achieved by systematic adjustments to the magnet currents to obtain focussed images of the target starting with images closest to the target. The set of counters S1, S2 and S3 are placed immediately before and after the first 'mass slit' - CV2. Attempts are first made to achieve horizontal and vertical focussing from the first stage. This is done by sweeping the vertical bending magnets VM1/VM2 and looking at S3 counts against the target monitor (M) counts to achieve a good horizontal focus. The current to the vertical focussing quadrupole magnet Q_4 is then varied to achieve a good focus in the vertical direction. This procedure is then repeated for the second stage looking at S5 counts against S2 counts. A check on the momentum selection can then be made by sweeping, in turn, magnets M1, M2 and M3 looking at S5 counts against the target monitor counts.

2.3 Scanning Procedure and Scan List

At each incident momentum the film was scanned twice. The discrepancies between the two independent scans were resolved by a third check scan. A scan list was then generated on magnetic tape. Scanning was done on machines provided with lens-mirror systems to project an image on to a table, the magnification on the Imperial College machines giving a life-sized picture of the chamber, and film transport mechanisms that enabled all three views to be moved together or independently in both directions. All three views were used in the scanning.

Reconstruction is generally inaccurate for tracks less than 10 cms. in length. A particular fiducial volume of the chamber was selected to ensure that only interactions with all tracks (apart from stopping secondaries) longer than 10 cms. are recorded. In each independent scan the scanners were required to record, on a scan card, the following information for each interaction seen within the volume:

(i) frame - event number

(ii) topology

(iii) secondary track ionisation estimates

(iv) a measuring code number signifying whether the event is off-beam or unmeasurable.

They were also required to indicate Dalitz pairs, associated electron pairs, secondary interactions and stopping tracks on a realistic sketch of the interaction on the card.

In the energy range of the present experiment the production of strange particles is extremely rare and as such neutral and/or charged decays are extremely rare. The topologies involved are therefore mainly 2-prongs and 4-prongs. The estimate of the ionisation of each secondary track was according to the following categories:

(i) minimum

(ii) between minimum and twice minimum

(iii) between twice minimum and three times minimum

(iv) greater than three times minimum and

(v) track has a visible $\pi \quad \mu \quad e$ decay

Two sets of scan cards obtained were provided at the scan tables during the check scan. Discrepancies between the number of events on a given frame were looked at and corrected. When a number of events on a given frame agreed in the two scans any discrepancies in topology or the measuring code number were sorted out by looking on the table. Where the ionisation estimates disagreed both were noted down on the final single card for the event. Thus a final single set of scan cards is obtained containing all the necessary information including the two scanners' numbers, the two (different) ionisation estimates and error code numbers, if any, assigned to the scan in error.

This information was punched on cards and fed into the program (ELIST) which flags punching errors, sequence errors and code errors. A final scan list was produced on magnetic tape when all errors have been corrected. The format of the scan list was chosen to allow for updating at the end of each pass and to allow the overall scanning efficiency to be computed.

2.4 Measuring Machines and Procedure

Measurements of the interactions were done on conventional image-plane and film-plane digitisers. The former were D-mac digitising tables with projection and transport systems similar to those on the scan tables. The film-plane digitisers used on the other hand, were the conventional Measuring Machines. In the case of the image-plane digitisers the film remains fixed during measurement and the measurer is asked to follow a track on the table with an index - a pair of cross-wires on a magnetic field coil. A pick-up coil, underneath the image top and connected to a pair of wires that are wound around a pair of graduated drums, follows this index. The drums have metal brushes in contact with them and these read off the graduations on the drums. These readings are electronically converted to x, y co-ordinates for the point being measured.

The least count on these digitisers is equivalent to 100 - 150 microns on the table and this corresponds to a bit size of 10 - 12 microns on film. This is in contrast to a bit size of 2 - 3 microns on film for the film-plane digitisers. At the low energies involved errors due to multiple Coulomb scattering dominate and hence measurements with a bit size of 10 - 12 microns are not expected to be too inaccurate in comparison. The mean value of the residuals on the tracks after geometrical reconstruction was found to be of the order of 15 microns on film for image-plane measured tracks as opposed to 8 microns for film-plane measured tracks.

Furthermore, reproducibility of digitisation of a given fixed point on the table was found to be good to be within $\pm$ 1 least count, as was the linearity in both the x and y directions. A further test was carried out to determine the distance between the point of intersection of the cross-wires and the centre of the magnetic field of the coil. The point of intersection of the cross-wires was set on a fixed point and rotated through 360°. The maximum variation in the x and y counts was found to be $\pm$ 3 counts. However it is observed that each measurer is fairly consistent in the alignment of cross-wires he/she prefers during measuring and does not rotate the cross-wires by more than $\pm 15^{\circ}$. So serious errors in measuring are likely to be introduced only from the distortions produced by the optics of the projection system. An investigation into the possibility of such distortions introducing a systematic error in the measurements was carried out. A known grid was projected on to the table and positions of various points on the grid measured. The measurements, after the usual transformations into a frame of reference where the point of intersection of the optic axis with the table is the origin, were compared with the expected positions (assuming distortion free optics). The difference between the two was found to be of the order of 1 - 2 counts and the distortions were found to have no systematic pattern. It was decided, therefore, that corrections to the digitisations would not lead to a discernible improvement in the geometrical reconstruction.

The scan cards for all measurable events were supplied to the measurers and they were instructed to record the book-keeping information at the start for each event. The event was then measured in a pre-arranged sequence of fiducials, apices and tracks on each view. The order of measuring of the tracks required the beam track to be measured first, followed by the secondary tracks in a clockwise order. This ensured that the secondary tracks were measured in the same order as the ionisation information for them was recorded on the scan list. All the measurements, punched out on paper tape, were converted to binary information on magnetic tape using the group's PDP6 computer or the college IBM 1401.

2.5 Fitting procedure

To obtain the final interpretation of the event, the measurements were fed through the BIND-THRESH-GRIND chain of programmes. The procedure used in each of these stages is briefly described in the following sub-sections.

2.5a Pre-Geometry checks

The order of measurement of the various quantities necessary for a final reconstruction of an event, is optimised for maximum speed of measurement and to reduce possible errors. The data is thus not in a state where it can be used directly for geometrical reconstruction. The pre-geometry programme - BIND - reads in the data and checks for correct sequence of measurements and labelling and corrects certain types of obvious labelling faults. For events without fatal errors the relevant quantities are arranged in a form suitable for THRESH and the necessary view, fiducial, vertex and track labels are inserted.

In the present experiment events that failed BIND were not passed any further in the processing and were essentially treated as not having been measured - i.e. no information was added for them on to the master list during the update stage (Sec. 2.6). The failure rate, almost entirely due to paper tape punch and paper tape reader faults, was of the order of 10%.

2.5b Geometrical reconstruction

Having sorted, checked, rearranged and relabelled the data appropriately it becomes necessary to reconstruct the vertices in space and to determine the physical variables describing the path taken by each track in space before attempting to correlate the tracks at each vertex. This was done by the geometrical reconstruction programme THRESH, written at CERN and modified to run on the IBM 7094 and the PDP 6 computers at Imperial College.

Details of the general checks done by THRESH and the procedures adopted in the vertex and track reconstruction can be found in reference 23). A detailed description of the mathematics involved in the reconstruction is given in reference 24).

The failure rate at the geometrical reconstruction stage was of the order of 10%. This was made up of the following three types of failures:

(i) If checks on the reconstruction of fiducial measurements resulted in less than three good fiducials on a given view the view was rejected by THRESH. Events with less than two good views were classed as fatal errors and were not proceeded with further in the fitting.

(ii) If pre-construction checks on track measurements on a given view resulted in too few good measurements, the view was ignored for that track. A track was completely ignored if this happened on two views. Such events were classed as failures but were not removed from the subsequent processing.

(iii) If the final helix fit on a track did not converge or if the residuals for the converged fit were too large, the track was classed as a failure. Events with such tracks were considered as having failed but they were passed on to the kinematic fitting stage.

Events that had failed due to fiducial measurement failure - (i) above - were essentially treated in the same manner as those failing BIND and no measurement information was added on to the master list for them at the update stage.

2.5c Kinematic fitting

Events that passed through THRESH - including failures of types (ii) and (iii) were fed into the CERN kinematic fitting programme - GRIND on the IBM 7094 or the PDP 6 computers. A full description of the programme and of the mathematical procedure used in the fitting is given in reference 25).

In the experiment the types of events measured were predominantly 2-prongs and 4-prongs. A fair proportion of them had 2-prong secondary interactions on one or more of the tracks. These secondary interactions were also measured to get a better estimate of the physical quantities of the connecting track. Hypotheses, for primary and secondary interactions, were supplied to GRIND in the form of mass assignments to the charged tracks and the mass assignments of the neutral particles involved, if any. If the physical quantities for the charged tracks were all well measured then the four energy momentum conservation equations allowed GRIND to evaluate the three physical quantities for, at the most, one neutral particle. So events with one neutral particle in the final state are fitted to one constraint (1-C) hypotheses and events involving no neutral particles are fitted to four constraint (4-C) hypotheses. Fits to the following hypotheses were attempted, at the production vertex by GRIND:

(i) Two prongs

Incoming track	target		Outgoing tracks 1	2	3	Constraints
π^+	p	$\longrightarrow$	π^+	p		4
		$\longrightarrow$	p	π^+		4
		$\longrightarrow$	π^+	p	π^o	1
		$\longrightarrow$	p	π^+	π^o	1
		$\longrightarrow$	π^+	π^+	n	1

(ii) Four prongs

Incoming track	target		Outgoing tracks 1	2	3	4	5	Constraints
π^+	p	$\longrightarrow$	π^+	p	π^+	π^-		4
		$\longrightarrow$	π^+	π^+	p	π^-		4
		$\longrightarrow$	p	π^+	π^+	π^-		4
		$\longrightarrow$	π^+	p	π^+	π^-	π^o	1
		$\longrightarrow$	π^+	π^+	p	π^-	π^o	1
		$\longrightarrow$	p	π^+	π^+	π^+	π^o	1
		$\longrightarrow$	π^+	π^+	π^+	π^-	n	1

For all hypotheses that gave fits GRIND listed the fitted and unfitted information along with values of missing mass squared, the missing energy, the χ^2 - probability etc. and estimates of the ionisation densities of the tracks predicted from the fitted values of the three track variables. The information was used to select out the most likely interpretations of the events.

Before attempting to fit any of the hypotheses to the event it was felt that GRIND should check for the following:

(i) THRESH failures of types (ii) and (iii) - (Section 2.5b)

(ii) GRIND failures: A check was made on the measurement errors on the three track variables against a standard external error. If the error was greater than three times the standard for all three variables GRIND flagged on error word of 160 for the track. Such events were considered to be too badly measured for the physical interpretations to be reliable.

(iii) Off-Beam events: The measured value of the beam momentum was checked against an external fed-in value. If the two are not consistent to within three times the measurement error on the beam momentum the event was flagged as a possible off-beam event. In such cases the measured beam momentum was used in the fitting. When the two momenta were consistent a weighted mean value was used in the fitting.

For the cases (i) and (ii) GRIND was modified to punch out a 'reject' card carrying the book-keeping information for the event and the information about the type of failure and the track(s) concerned. Any subsequent fits that may converge for such events can therefore be ignored and the information about the failure passed on to the master list at the up-date stage.

2.6 Kinematic fit selection and up-dating of the Master List

In general more than one hypothesis give converging fits to the event at the kinematic stage. If the event had not suffered any fatal failures - type (i) and (ii) in Section 2.5c - a 'slice' card was punched out by GRIND for each fit. The slice card contained the usual book-keeping information along with a unique number describing the hypothesis.

At the selection stage the events were looked at on the scan table and the predicted ionisation of the charged tracks checked against the observed ionisation for each fit. The fit predicting ionisation consistent with observed ionisation was accepted in every case. Where this left an ambiguity between the elastic (4-C) fit and one π^0 production (1-C) fit with the same mass assignments to the charged tracks the (4-C) fit was accepted. It was felt that the more highly constrained fit was more likely to be the correct interpretation of the event. The $\pi^+\pi^+n$ fits were uniquely selected on ionisation consistency alone. In the case of 4-pronged events 1-C fits are so unlikely by energy requirements that the problem of ambiguous fits did not arise.

The events that were flagged as off-beam by GRIND were checked in the above manner with the additional check that the fitted beam momentum for the ionisation consistent fit be within three standard deviations of the expected beam momentum. If the fitted beam momentum did not satisfy this check the event was classified as off-beam and a pseudo-slice card punched to convey this information to the master list at the up-date stage.

For events that were apparently well-measured, but did not give any fit consistent with ionisation the values of the missing-mass squared were checked to see if the event was consistent with the interpretation that there is more than one neutral particle involved - the charged tracks being identified using the ionisation estimates worked out by GRIND from the unfitted values of the track variables with the mass assignments of a proton, a kaon and a pion, in turn. If the event was considered consistent with multi-neutral production a pseudo-slice card was punched to convey this information to the master list along with the mass assignments of the charged tracks.

In cases where the event could not be assigned to any of the categories discussed above it was looked at carefully to see if the beam track was obscured by nearby beam tracks to make it almost impossible to measure. It was thus possible to re-classify an event as unmeasurable by punching an appropriate pseudo-slice card. Also, there were a few of the 4-pronged events that were really 2-prongs with Dalitz pairs. Again it was possible to convert the topology by use of a pseudo-slice card.

2.61 <u>Master List Update</u>

For each event that reaches the kinematics stage we have a slice card after the fit selection stage. It carries the hypothesis number of the ionisation consistent fit that has been accepted on the final interpretation of the event. For events with no acceptable fits it carries a code word (TF = Thresh Failure, GF = Grind Failure, NF = Multineutral etc.) and a code number. For THRESH/GRIND failure the code number signifies the track(s) affected and for multineutrals it indicates the type of multineutral final state (e.g. $\pi^+ \quad 2\pi^0$ or $\pi^+\pi^+(\quad \pi^0)$ for 2-prongs). Scanning corrections decided by the physicist for a given event at the fit selection stage can be punched out on to cards and these pseudo-slice cards are added on to the rest of the deck.

The slice cards and the last updated Master List form the input to a program called SLIST which checks for slice card format errors, orders the cards and merges the information on the cards with the Master list to produce the updated Master list. Any card referring to an event with a previous successful decision is ignored. Every event with a successful fit or multineutral final state decision from the current pass gets the pass number added on to the frame-event number. The updated Master list is read back to list all measurable events for which no successful decision has yet been reached. For these the reject words are picked up and decoded and an appropriate message written on the remeasure list. The remeasure list is sent back to the measuring machines for another pass.

Three such passes were found to be necessary to achieve a more than 90% pass rate at each incident momentum.

2.7 The Data Summary Tapes

At the completion of the final pass the GRIND library tapes produced are read by the program - DSTPRO - to select out the accepted fits for each successful event by checking against the final updated master list. The book-keeping information, the missing mass squared, the missing energy, the χ^2 for the accepted fit etc. are written on to a final tape along with the unfitted and fitted values of the track variables and the final mass assignments to the tracks. This final tape is the end product of the data reduction process described in the preceding sections of this chapter. As such it contains every physical quantity for each event that is likely to be necessary in looking for systematic biases in the experiment and for generating the final distributions of the various variables required to describe the scattering processes involved.

These Data Summary Tapes (DSTs) are the input to the statistics program - SUMX - used to obtain all these distributions.

THE K1 BEAM LINE (schematic)

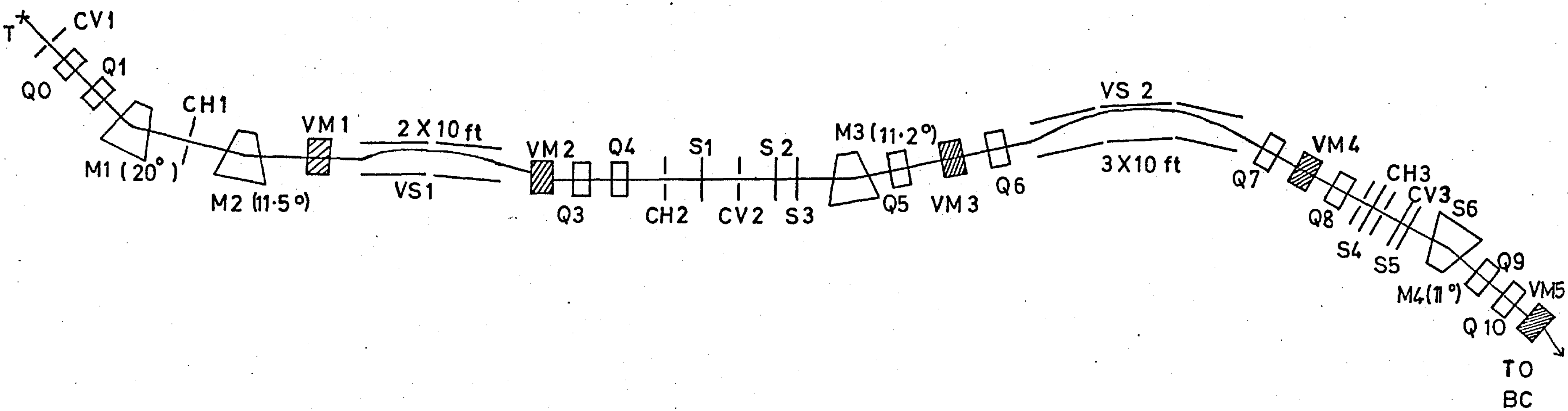

T - internal target

CV 2, CV3 - mass slits

VS 1, VS 2 - electrostatic separaters

S1 - S6 - counters

CV 1 - vertical angular acceptance slit

Q 0, Q 1 / Q3-Q10 - focussing and defocussing quadrupole magnets

M1-CH1 / M2-CH2 / M3-CH3 - bending magnet - vertical slit combinations for momentum definition

Fig. 2·1

Processing System

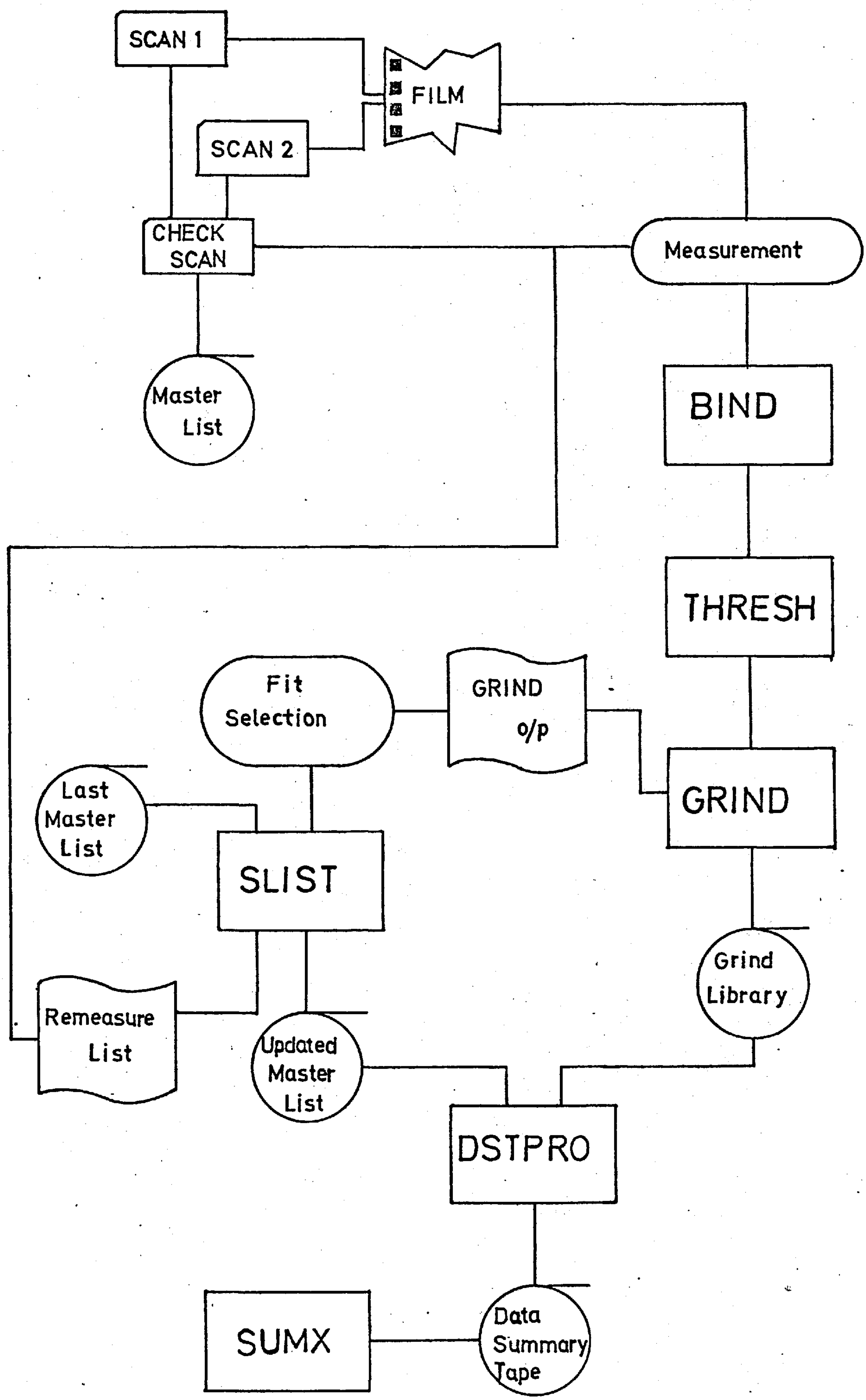

Fig. 2·2

CHAPTER 3

Biases, Elastic Scattering and Inelastic Channel Cross-sections

3.1 Introduction

Systematic biases can creep into the lengthy process of analysis of a bubble chamber experiment at any of the various stages described in the preceding chapter. The presence of such effects in this experiment and methods used to correct or account for them are discussed in this chapter. The overall channel cross-sections for the different final states are presented at each of the four incident momenta. Possible biases introduced at the scanning and measuring stages of the processing are discussed in Section 3.2. Section 3.3 describes the method of correction used for the scanning biases in the elastic channel. In Section 3.4 are presented the final experimental results for positive-pion proton elastic scattering at the four incident momenta. Section 3.5 presents the cross-sections for the various inelastic channels at the four momenta and these are compared with results from earlier experiments.

3.2 Biases in scanning and Processing

When two independent scans are done and the discrepancies between them sorted out by a check scan the overall scanning efficiency can be calculated. With the assumption that every event is equally likely to be seen in a given scan it can be easily shown that the overall scanning efficiency is given by

$$E = \frac{N_{12} \; (N_1 + N_2 - N_{12})}{N_1 \; N_2} \qquad (3.1)$$

where N_1, N_2 are the numbers of events seen in Scan 1 and Scan 2 respectively and N_{12} is the number of events seen in both the scans. The scanning efficiency at each incident pion momentum worked out, using (3.1), to be of the order of 99.8%. With this sort of scanning efficiency it would seem safe to assume that there are no scanning losses. However, it is well known that the assumption used in evaluating E is not generally true for all 2-pronged interactions. There are two types of 2 pronged events that are difficult to spot during scanning. These are:

(i) Events where one of the charged tracks is a short stopping proton. Elastic scatters involving short stopping protons are small angle scatters and hence the scattered pion is not appreciably deflected from the incident direction. In the case of inelastic events involving short stopping protons, however, the charged pion is appreciably deflected from the incident beam direction. This type of scanning bias is therefore expected to show up in elastic scattering only.

(ii) Events where the plane containing the two charged tracks is perpendicular to the front glass of the chamber. If the interaction is an elastic scatter then the incident beam track is coplanar with the outgoing tracks and hence the plane containing all the three tracks is then in the line of sight of the scanner. As such, elastic scatters that are in a plane perpendicular to the front glass are more likely to be missed during scanning than the average 2-pronged events.

These two types of biases involving 2-pronged events mainly affect the elastic channel. A more meaningful estimate of scanning efficiency can be made using the sample of inelastic events. The scanning efficiency for inelastic events turns out to almost a 100% at each of the four momenta. So, apart from correcting the results obtained for elastic scattering for effects of the two types of scanning losses, there are no other corrections necessary as far as scanning is concerned.

The next stage at which possible systematic biases can creep in is the measuring and processing stage. The accuracy of the measuring machines used has been discussed in the preceding chapter. Investigation of systematic biases can only be undertaken after the geometrical reconstruction and the kinematic fits have been done. Once the physical interpretation of an event has been decided it is possible to look at various physical quantities that have a fixed expected distribution for bias-free data.

The first of these is the 'chi-square' value obtained from the kinematic fit. The frequency distribution of the 'chi-square' for a given number of constraints is well defined. Comparison of the experimental distribution to this expected curve gives an indication to the correctness, or otherwise, of the errors assigned to the track variables by the geometrical reconstruction. Figs. 3.1a and 3.1b show the experimental and the expected χ^2 distributions for the elastic (4-c) and the one pion production (1-c) channels respectively at 895 MeV/c. The agreement between the two is good enough to give confidence in the errors estimated in the geometry.

The normalised stretch function, Sij, defined, for the j^{th} track variable of the i^{th} track, as

$$S_{ij} = \frac{x_m - x_f}{\left[(\Delta x_m)^2 - (\Delta x_f)^2\right]^{\frac{1}{2}}} \qquad (3.2)$$

where x_f and x_m are the fitted and measured values, and Δx_f and Δx_m are the errors on them, is expected to have a Gaussian distribution around 0 with a standard deviation of 1, if the measured values of the track variables and their errors are correctly evaluated. The nine stretch function distributions involved in elastic scattering were looked at and found to agree well with the expected distributions.

Incorrect interpretation of events can result in contaminations in the final samples for the various channels. The low energies involved in this experiment ensure that an event involving a proton in the final state can be visually distinguished from an event that does not have a proton in the final state. There is no doubt therefore that the reaction $\pi^+p \rightarrow \pi^+\pi^+n$ is cleanly separated. For the elastic and one-π^0 production channels it is possible to see if the final selected samples contain any contamination by looking at the missing-mass squared and the missing energy distributions. Figures 3.2a and 3.2b show these distributions at 995 MeV/c. There is clearly no evidence of any contamination of one channel by the other.

It has been stated in the preceding chapter that an overall pass rate (in terms of acceptable kinematic fits) of 93% was achieved at each incident momentum after three measurements. This left a 7% residue of events that either never gave good geometry at any of the three measurements or did not give fits that agreed with the visually observed ionisations of the tracks. The residue was looked at carefully by physicists who, by expertise, were able to decide on the possible physical interpretation of these events. On the basis of these decisions it was found that the proportion of events, relative to the total residue, in each of the different channels was the same as that in the overall selected sample. Since the experiment was not designed to evaluate absolute cross-sections, it is not necessary to make any corrections to the selected samples for this residue.

3.3 Corrections for Scanning bias - Elastic Channel

Before the method by which corrections to the elastic channel are made for the two scanning losses discussed in Section 3.2 it is necessary to discuss the final beam momentum distributions obtained from the kinematic fits. The estimated error on the beam momentum fed in as data to GRIND was $\pm$ 25 MeV/c. This includes the 10 MeV/c spread in the incident beam momentum due to 1% momentum bite and a spread of 10 MeV/c introduced by slowing down in the beam window. The mean measurement error on the beam moment is of the order of $\pm$ 15 MeV/c. The fed-in values for incident beam momentum, used in GRIND to find the weighted mean with the measured values, were the nominal beam line values - 905, 955, 1005 and 1050 MeV/c - at the four momenta. The fitting procedure in GRIND resulted in pulling the mean values down by 10 MeV/c in each case and the spread was of the order of 45 MeV/c. Figure 3.3 shows the fitted beam momentum distribution obtained for the fourth momentum. To select out a reasonably clean sample it was decided to impose cuts of ± 35 MeV/c around the mean values of the fitted beam momentum distributions. Table 3.1 gives the mean momentum values and the total numbers of events within the cuts at each momentum.

Table 3.1

No.	Momentum (MeV/c)	Total No. of events
1	895 ± 35	11,499
2	945 ± 35	14,973
3	995 ± 35	14,549
4	1040 ± 35	13,422

Table 3.2 presents the numbers of events in the elastic channel within the fitted beam momentum cuts described above.

Table 3.2

Incident Momentum (MeV/c)	No. of Elastics (uncorrected)
895	4415
945	6222
995	6434
1040	6110

These numbers are not corrected for the scanning losses described in the preceding section.

The incident beam direction was almost parallel to the front glass-liquid interface (the $z = o$ plane). The angle ϕ between the plane of the elastic interaction and the $z = o$ plane was determined for each event. The distribution of the centre of mass scattering angle (θ^*) as a function of ϕ

showed that losses due to small angle scatters occurred for $\cos\theta^* > 0.90$ and that this was the case over the whole range of ϕ. Over the rest of the range of θ^* ($-1.0 < \cos\theta^* < 0.90$) losses were seen to occur around $\phi = \pi/2$. An estimate of the actual number of events with $\cos\theta^* > 0.90$ can only be made by extrapolating the distribution over the remaining $\cos\theta^*$ range, provided this distribution itself is bias free. The procedure adopted to get a bias free sample of elastic events in the range $-1.0 < \cos\theta^* < 0.90$ was as follows.

A cut around $\phi = \pi/2$ was imposed to remove a fixed percentage of events from the overall sample in the above θ^* range. The resulting $\cos\theta^*$ distributio is fitted to the Legendre Polynomial expansion.

$$\frac{dN}{d\cos\theta^*} = a_0\left[1 + \sum_{l=1}^{L} C_l P_l (\cos\theta^*)\right] \qquad (3.3)$$

where a_0 is the normalisation constant, C_l is the normalised coefficient of the Legendre Polynomial of the l^{th} order and L is the maximum value of l. The normalisation constant and the normalised Legendre Polynomial coefficients are determined by minimising the χ^2 defined by

$$\chi^2 = \sum_{i=1}^{n}\left(\frac{N^i_{exp} - N^i_{fit}}{\Delta N^i_{exp}}\right)^2 \qquad (3.4)$$

where N^i_{exp} and N^i_{fit} are the experimental number of events and the fitted number of events in the i^{th} $\cos\theta^*$ bin and ΔN^i_{exp} is the error on the experimental number.

. The normalisation constant a_0 was determined by equating the integral of (3.3) over the range $-1.0 < \cos\theta < 0.90$ to the total number of events used in the fit. Fits were done with values of L ranging from 1 to 10 and Fisher's F - ratio test is applied to determine the order of the first Legendre polynomial coefficient consistent with 0. Integrating (3.3) over the complete range of $\cos\theta^*$ gives the total number of events expected in the channel within the cut in ϕ.

$$\text{Total No. of events} = \int_{-1}^{+1} \frac{dN}{d\cos\theta^*}\, d\cos\theta^* = 2a_o \qquad (3.5)$$

Values of a_o and the coefficients C were determined for different sized cuts in ϕ around $\pi/2$ to determine the range of ϕ around $\pi/2$ over which there is a scanning bias. Although the values obtained for the parameters were all within one standard deviation they were found to be independent of ϕ for events with ϕ outside the range $0.45\pi < \phi < 0.55\,\pi$ at all four incident momenta.

The final bias free sample of elastic events was, therefore, obtained with the following cuts applied to the overall sample

$$-1.0 < \cos\theta^* < 0.90$$

$$\phi < 0.44\pi \text{ and } > 0.56\pi \qquad (3.6)$$

This implies the rejection of 12% of the elastic events due to the cut in ϕ. The total number of events obtained from the fit (3.5) was thus upgraded to obtain the final expected total number of events in the channel at each incident momentum. Table 3.3 presents the corrected total number of events in the elastic channel and the overall corrected total number of events at each incident momentum.

Table 3.3

Incident Momentum (MeV/c)	No. of Elastics (corrected)	Total No. of events (corrected)
895	4730 ± 89	11829 ± 123
945	6750 ± 100	15501 ± 137
995	6925 ± 115	14990 ± 146
1040	6570 ± 109	13882 ± 138

3.4 π^+p Elastic scattering - Results and Discussion

In this section total elastic and elastic differential cross-sections obtained in the present experiment are presented and compared with the results from previous experiments. The disagreements are high-lighted and the checks made for other possible biases, in the present experiment, that could give rise to these disagreements are discussed. Finally possible effects of the present results on the results of phase shift analyses (Chapter 1) are discussed.

At the incident energy range of the present experiment two recent counter measurements of the total positive pion proton cross-section exist. These are the data of Carter et al[26] and Giacomelli et al[27]. The two sets of results disagree by about 10% at all incident pion energies. In the present experiment the values of Ref. 27 are used to normalise the corrected total number of events at each incident momentum and determine the microbarn equivalent per event. Table 3.4 presents the values of the elastic cross-sections determined by this experiment at the four incident pion momenta.

Table 3.4

Incident Momenta (MeV/c)	Corrected No. of Elastic events	Elastic cross-section (mb.)
895	4730 ± 89	8.37 ± 0.18
945	6750 ± 100	10.32 ± 0.18
995	6925 ± 115	11.70 ± 0.23
1040	6570 ± 109	12.37 ± 0.20

These values of the positive pion-proton elastic cross-section are in reasonable agreement with previously determined values[28] as shown in figure 3.4.

The highest order of Legendre polynomial fitted to the distribution (L in (3.3)) is determined by the F-ratio test. The values of L required at the four incident momenta are 4, 4, 5 and 6. The range of $\cos\theta^*$ is divided into bins of interval 0.05 and the differential cross-sections (experimental and fitted) in these bins, the central $\cos\theta^*$ values and the numbers of events within the cuts specified by (3.6) in each bin have been presented in tabular form in reference 29). The experimental and fitted differential cross-section distributions are shown in figures 3.5a, 3.5b, 3.5c, and 3.5d for the four incident momenta. The values obtained for the normalised (C_l) - (3.3) - and the unnormalised (A_l) Legendre polynomial coefficients, for the expansion.

$$\frac{d\sigma}{d\Omega} = \lambda\!\!\!^{-2} \sum_{l=0}^{L} A_l P_l (\cos\theta^*) \qquad (3.7)$$

($\lambda\!\!\!^- = 1/q$, where q is the incident pion momentum in the centre of mass, in natural units with $\hbar = c = 1$), are presented in Table 3.5.

Table 3.5

Incident Momentum → / Coefficient ↓	895 MeV/c	945 MeV/c	995 MeV/c	1040 MeV/c
a_0	2079.7 ± 39.2	2976.6 ± 45.9	3043.9 ± 50.4	2890.5 ± 47.9
A_0	0.465 ± 0.010	0.617 ± 0.11	0.748 ± 0.015	0.843 ± 0.016
C_1	1.339 ± 0.038	1.314 ± 0.026	1.308 ± 0.027	1.339 ± 0.027
A_1	0.624 ± 0.018	0.811 ± 0.016	0.978 ± 0.020	1.128 ± 0.023
C_2	1.206 ± 0.057	1.264 ± 0.036	1.284 ± 0.044	1.358 ± 0.044
A_2	0.561 ± 0.027	0.781 ± 0.022	0.961 ± 0.033	1.142 ± 0.037
C_3	0.383 ± 0.060	0.401 ± 0.046	0.340 ± 0.063	0.395 ± 0.057
A_3	0.178 ± 0.028	0.248 ± 0.029	0.254 ± 0.047	0.333 ± 0.048
C_4	-0.413 ± 0.081	-0.272 ± 0.043	-0.269 ± 0.063	-0.031 ± 0.058
A_4	-0.192 ± 0.038	-0.168 ± 0.027	-0.201 ± 0.047	-0.026 ± 0.049
C_5	-	-	-0.138 ± 0.051	-0.024 ± 0.022
A_5			-0.103 ± 0.038	-0.020 ± 0.018
C_6	-	-	-	0.178 ± 0.046
A_6				0.150 ± 0.039

Extensive measurements of elastic differential cross-sections have been carried out at Berkeley[30] and at the Rutherford Laboratory[31] using counter techniques. Three bubble chamber experiments[32), 33), 34)] have also been published in this energy range. A useful comparison of the results from the two techniques has so far not been possible due to poor statistics of most previous bubble chamber experiments. The high statistics of the present experiment now permit this to be done. The results are in good agreement with counter results over most of the cos θ^* range. However, a marked difference close to cos $\theta^* = -1$ is observed at all four momenta. Figure 3.6 compares the present results with those of Duke et al[31] over the range $-1 < \cos\theta^* < 0$ at 945 MeV/c incident momentum. Over the incident momentum range 895 MeV/c to 1040 MeV/c the present results show the backward peak developing at a higher incident momentum than in the counter measurements. Assuming that the counter measurements in the backward direction are correct, the present experiment could have lost events in the backward direction at the scanning, fitting or fit selection stages of the analysis.

The scanning efficiency for backward elastic events was calculated from the final master lists and found to be 98.5% - under one per cent less than the overall scanning efficiency. A selection of the film was scanned a third time to look for two-pronged events with one secondary track making an angle of more than 90° with the incident track in the laboratory. No significant loss of such events was detected. It is clear that scanning losses are not responsible for the lower backward elastic cross-section in the present experiment.

The χ^2 distribution for backward elastic events was examined and found to be identical to the overall distribution for elastic events. The last possibility is that the fit selection criteria could be biased against backward elastic events. These events should therefore be present in the inelastic sample. The characteristics of the $\pi^+ p \pi^0$ and $\pi^+\pi^+ n$ samples were examined as a function of coplanarity and contamination of these samples by elastic events was found to be unlikely. The configuration of a backward elastic event is such that it involves a fast forward proton with a momentum considerably higher than that of the incident pion in the laboratory. The laboratory momentum distribution of the secondary tracks for those inelastic events where the secondary tracks are approximately coplanar with the beam track showed that the momenta of secondary tracks for such events were at least 200 MeV/c less than that of the incident pion.

There is clearly no evidence of a systematic bias against backward elastic events in the present bubble chamber experiment. The present results for backward ($\cos \theta^* = -1.0$) elastic differential cross-sections are statistically more accurate than those previously reported.

It has been pointed out in an earlier chapter how the characteristics of the scattering of individual partial waves are deduced from the overall elastic differential cross-section distributions along with the polarization distributions at a large number of incident pion energies. The results of a comprehensive partial wave analysis allow deductions to be made about the nature of scattering in individual partial waves. In this centre of mass energy range (1.6 - 1.7 GeV/c^2) the various phase shift analysis[6), 7), 8), 9)] have deduced the existence of three possible I = 3/2 nucleon resonances. The values of the phase shifts and the inelasticities, for the partial waves involved, for the solutions obtained by these groups are inconsistent with the $\cos \theta^*$ distributions obtained in this experiment, particularly near $\cos \theta^* = -1$. The differential cross-section distribution predicted by, what is called, the CERN - Theory solution[6)] is shown along with the present experimental results at the incident momentum 945 MeV/c in figure 3.5b.

In a given partial wave that shows resonance behaviour, the magnitude of background amplitude is likely to be not much larger than that of the resonant amplitude only in the backward hemisphere. In this region diffractio scattering background is negligible. Any significant background amplitude is likely to come from baryon exchange processes. The distribution of the elastic differential scattering cross-section in the backward hemisphere is thus likely to be extremely sensitive to resonant scattering. This has been dramatically demonstrated[35), 36), 37)]. The resonancesinvolved - the S_{31} (1640), P_{33} (1688) and D_{33} (1690) - are supposed to have widths of the order of 200 - 300 MeV. This is more than twice the range of energy covered by the present experiment. Four values of the elastic differential cross-section at

$\theta^* = 180^\circ$ over so small an energy range are not sufficient to extract information about resonant behaviour by the Barger and Cline method[37]. The discrepancy between the present values of $\frac{d\sigma}{d\Omega}$ at $\theta^* = \pi$ and earlier reported values implies the need for more bubble chamber experiments of comparable statistics at the surrounding energies.

Attempts to determine the partial wave amplitudes using the present elastic differential cross-section distributions alone by energy independent partial wave analysis result in ambiguous solutions. These ambiguities can only be meaningfully resolved in an overall phase shift analysis imposing continuity over the complete energy range up to 2 GeV/c incident momentum.

3.5 Inelastic channel cross-sections

In the range of the incident pion momenta of this experiment the inelastic positive pion proton reactions are:

$$\pi^+ p \longrightarrow \pi^+ p\, \pi^0 \tag{3.8a}$$

$$\longrightarrow \pi^+ n\, \pi^+ \tag{3.8b}$$

$$\longrightarrow \pi^+ p\, \pi^+ \pi^- \tag{3.8c}$$

$$\longrightarrow \pi^+ p\ (\geqslant 2\pi^0) \tag{3.8d}$$

$$\longrightarrow \pi^+ \pi^+\ (n + 1 \text{ or more } \pi^0) \tag{3.8e}$$

The incident threshold momentum for the reaction $\pi^+ p \rightarrow \Sigma^+ K^+$ is 1020 MeV/c in the laboratory. This is 20 MeV/c below the highest incident pion momentum in the experiment. At this momentum about 20 events of this reaction have been identified. The reactions 3.8d and 3.8e are multineutral production reactions and events of this type were identified at the fit selection stage by identifying the charged tracks from the observed ionisation and deciding whether the missing mass-squared, with the appropriate mass assignments to the charged tracks, was consistent with multineutral production. As such the sample of multineutral production events is likely to be contaminated by some single-neutral production events - reactions (3.8a) and (3.8b). The total number of multineutral events found at each momentum was found to be only slightly greater than the number of 4-pronged events - reaction (3.8c).

Hence the loss of one-pion production events - (3.8a) and (3.8b) - as a result of their classification as multi-neutrals is minimal.

The final selected samples for reactions (3.8a) and (3.8b) could have been contaminated by elastic interactions. However, it has been mentioned in the preceding section of this chapter that the two samples were carefully examined to check that elastic events were not being erroneously classified as inelastics and that no evidence was found of this. Selection between the two single pion production channels is believed to be uniquely done on ionisation observation alone at the present range of energy. The three important inelastic channels are therefore believed to be cleanly separated. Table 3.6 presents the numbers of events and the cross-sections for those three reactions at the four incident momenta.

Table 3.6

Incident Momentum (MeV/c)	$\pi^+p \rightarrow \pi^+p\pi^0$		$\pi^+p \rightarrow \pi^+\pi^+n$		$\pi^+p \rightarrow \pi^+p\pi^+\pi^-$	
	No. of events	Cross-section (mb)	No. of events	Cross-section (mb)	No. of events	Cross-Section (mb)
895	5783	10.22 ± 0.17	957	1.70 ± 0.06	122	0.22 ± 0.02
945	6959	10.66 ± 0.16	1195	1.83 ± 0.06	268	0.41 ± 0.02
995	6256	10.58 ± 0.17	1203	2.03 ± 0.06	234	0.40 ± 0.03
1040	5583	10.50 ± 0.18	1119	2.10 ± 0.07	262	0.49 ± 0.03

The estimated numbers of events and the cross-sections for the two multi-neutral production channels are given in Table 3.7.

Table 3.7

Incident Momentum (MeV/c)	$\pi^+p \rightarrow \pi^+p\ (\geqslant 2\pi^0)$		$\pi^+p \rightarrow \pi^+\pi^+\ (n + \geqslant 1\pi^0)$	
	No. of events	Cross-section (mb)	No. of events	Cross-section (mb)
895	175	0.31 ± 0.02	62	0.11 ± 0.01
945	261	0.40 ± 0.02	68	0.10 ± 0.01
995	316	0.53 ± 0.03	56	0.09 ± 0.01
1040	246	0.44 ± 0.03	102	0.19 ± 0.02

The errors quoted on the cross-sections are statistical. The present results are statistically far more accurate than values previously reported [32), 33), 34), 38)]. The results along with previously published data and the recently reported results of M. Bowler and R. Cashmore[39)] for the 1-π production reactions are shown in figures 3.7 and 3.8.

The variation with energy of these inelastic cross-sections are discussed at length in the chapters following.

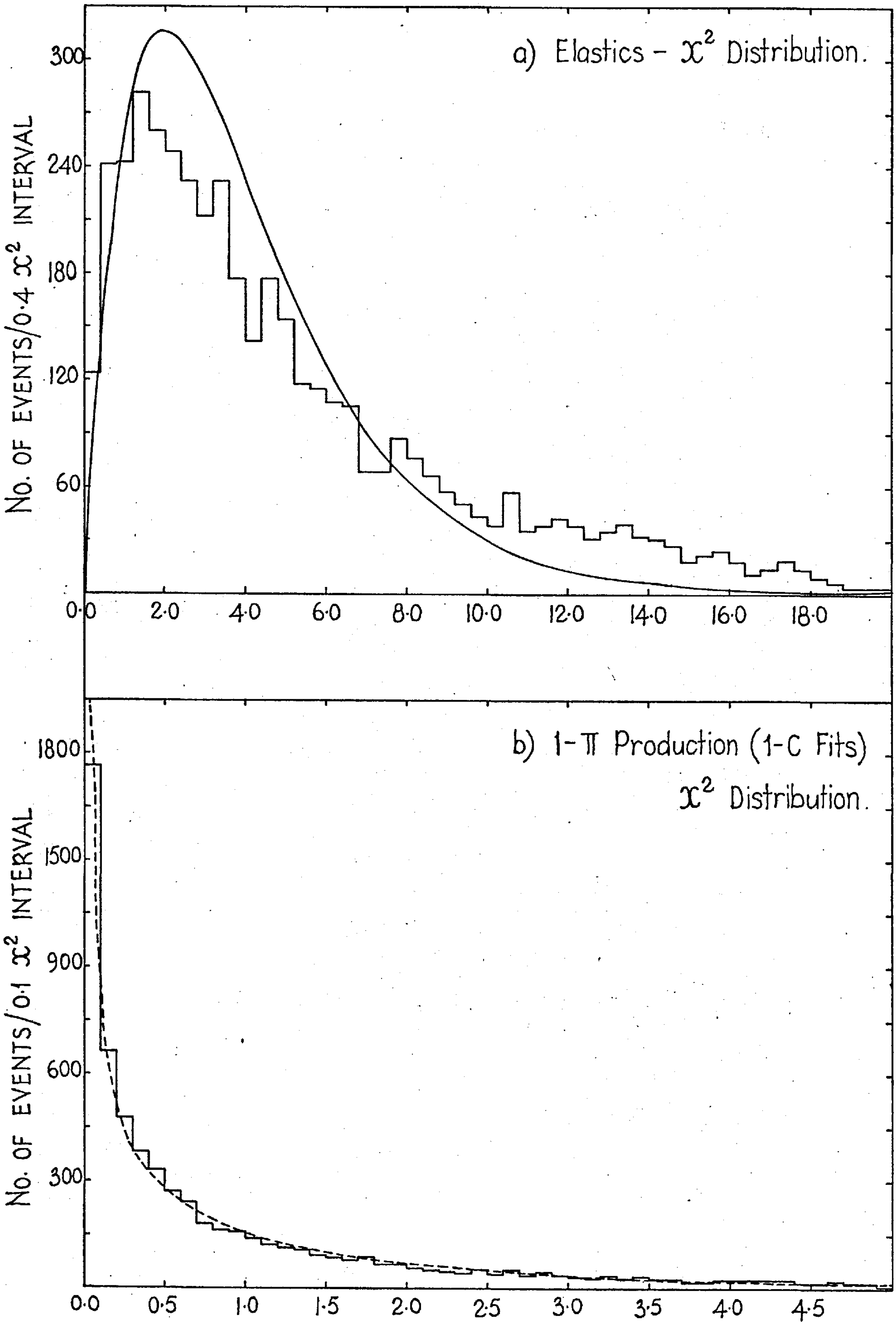
a) Elastics - χ^2 Distribution.
No. OF EVENTS/0·4 χ^2 INTERVAL
300
240
180
120
60
0·0
2·0
4·0
6·0
8·0
10·0
12·0
14·0
16·0
18·0
b) 1-π Production (1-C Fits)
χ^2 Distribution.
No. OF EVENTS/0·1 χ^2 INTERVAL
1800
1500
900
600
300
0·0
0·5
1·0
1·5
2·0
2·5
3·0
3·5
4·0
4·5

Fig. 3·1

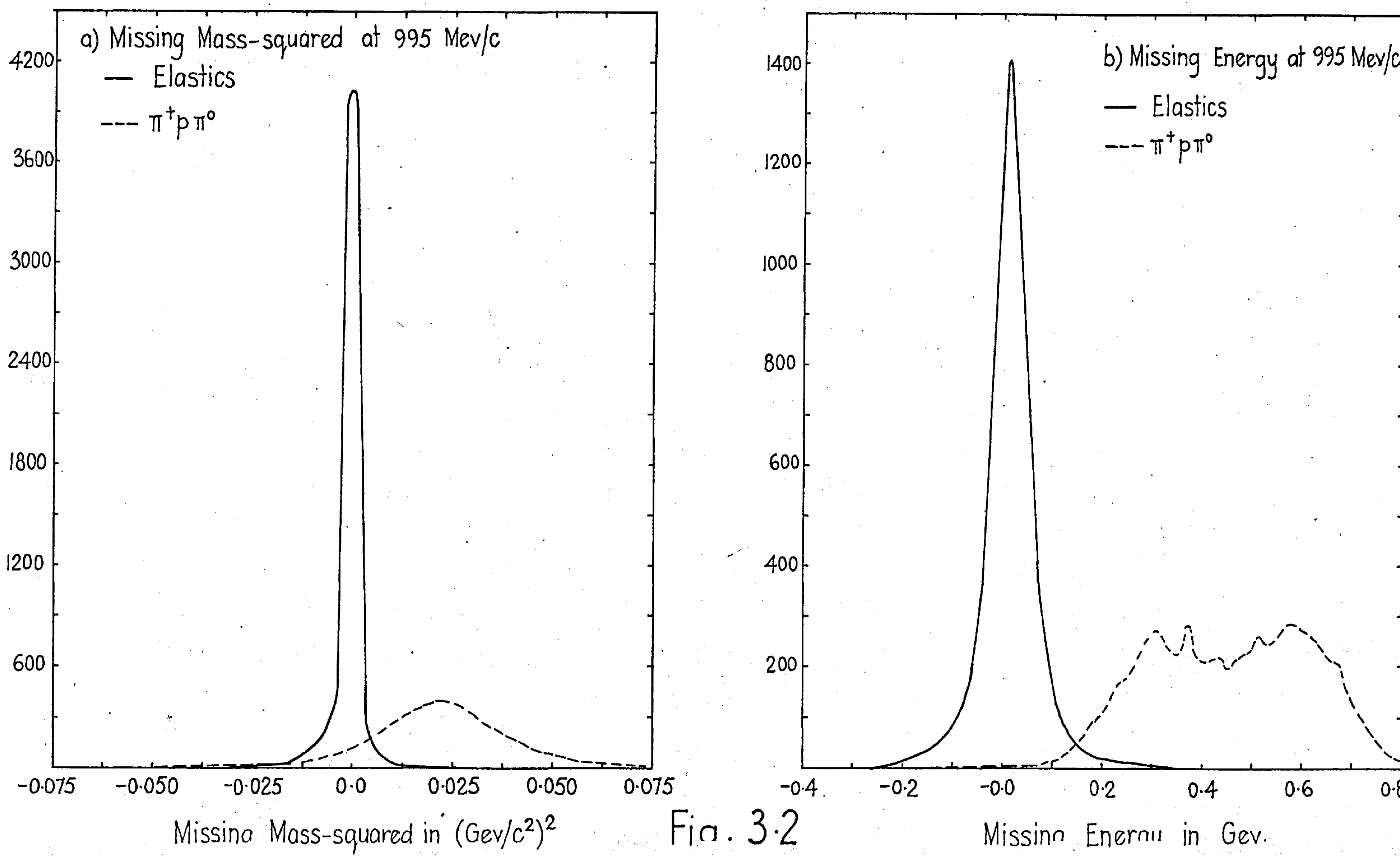
a) Missing Mass-squared at 995 Mev/c
— Elastics
--- π⁺pπ°
4200
3600
3000
2400
1800
1200
600
-0.075
-0.050
-0.025
0.0
0.025
0.050
0.075
Missing Mass-squared in (Gev/c²)²
b) Missing Energy at 995 Mev/c.
— Elastics
--- π⁺pπ°
1400
1200
1000
800
600
400
200
-0.4
-0.2
-0.0
0.2
0.4
0.6
0.8
Missing Energy in Gev.

Fig. 3.2

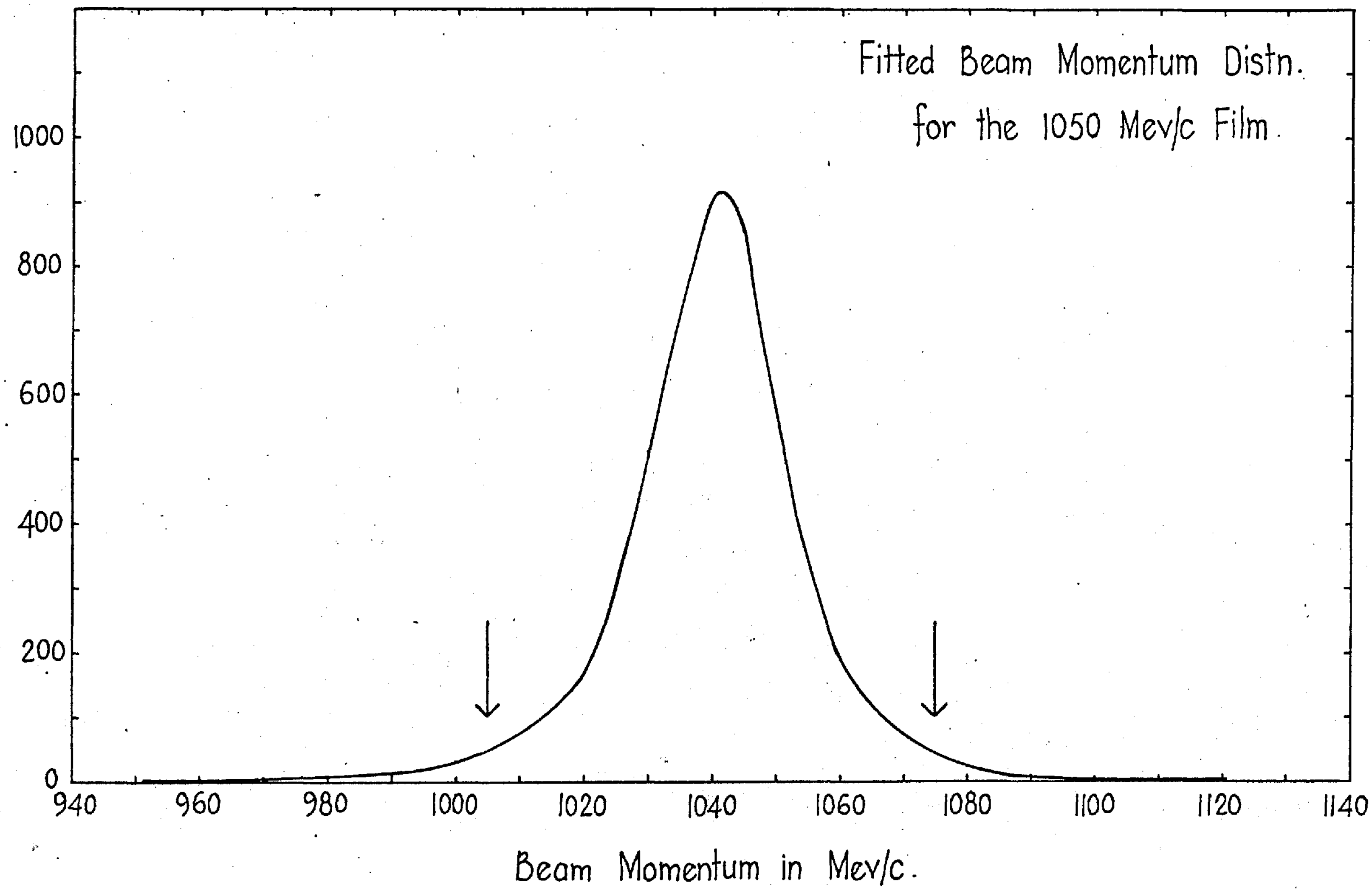
Fitted Beam Momentum Distn.
for the 1050 Mev/c Film.
1000
800
600
400
200
0
940
960
980
1000
1020
1040
1060
1080
1100
1120
1140
Beam Momentum in Mev/c.

Fig. 3·3

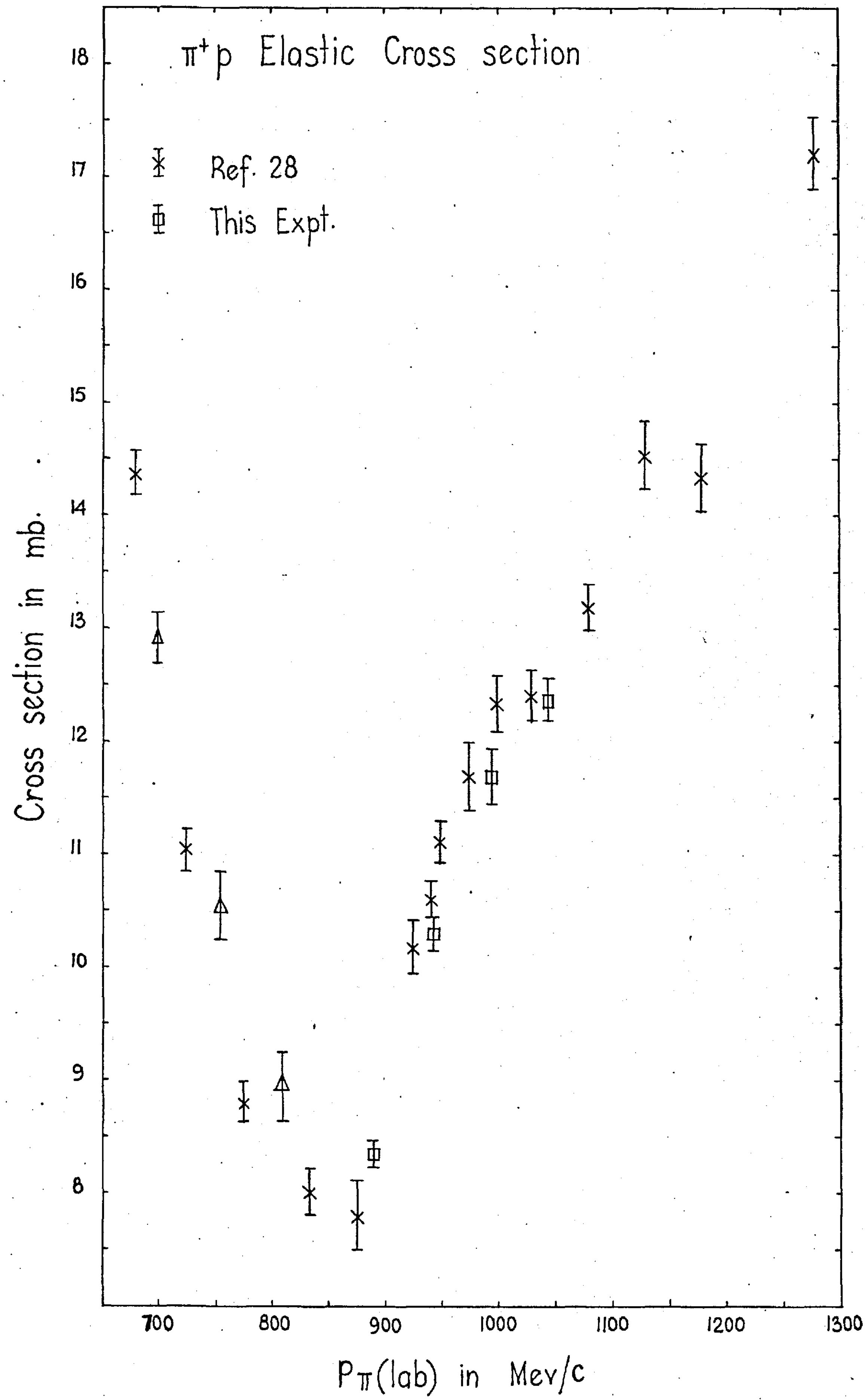

π⁺p Elastic Cross section
Ref. 28
This Expt.
Cross section in mb.
18
17
16
15
14
13
12
11
10
9
8
700
800
900
1000
1100
1200
1300
Pπ(lab) in Mev/c

Fig. 3·4

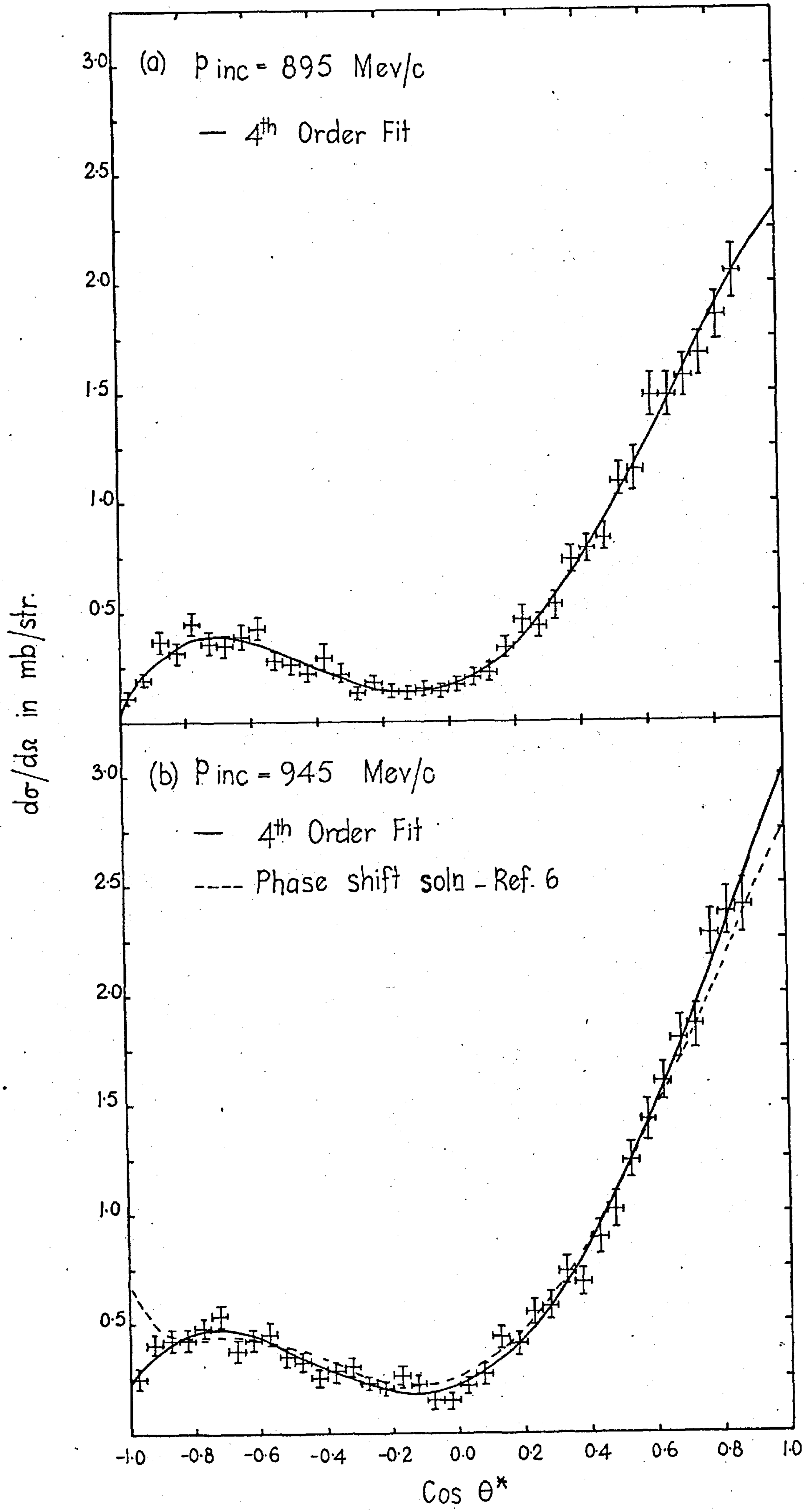
(a) P inc = 895 Mev/c
— 4th Order Fit
(b) P inc = 945 Mev/c
— 4th Order Fit
---- Phase shift soln - Ref. 6
dσ/dΩ in mb/str.
3·0
2·5
2·0
1·5
1·0
0·5
-1·0
-0·8
-0·6
-0·4
-0·2
0·0
0·2
0·4
0·6
0·8
1·0
Cos θ*

Fig. 3·5

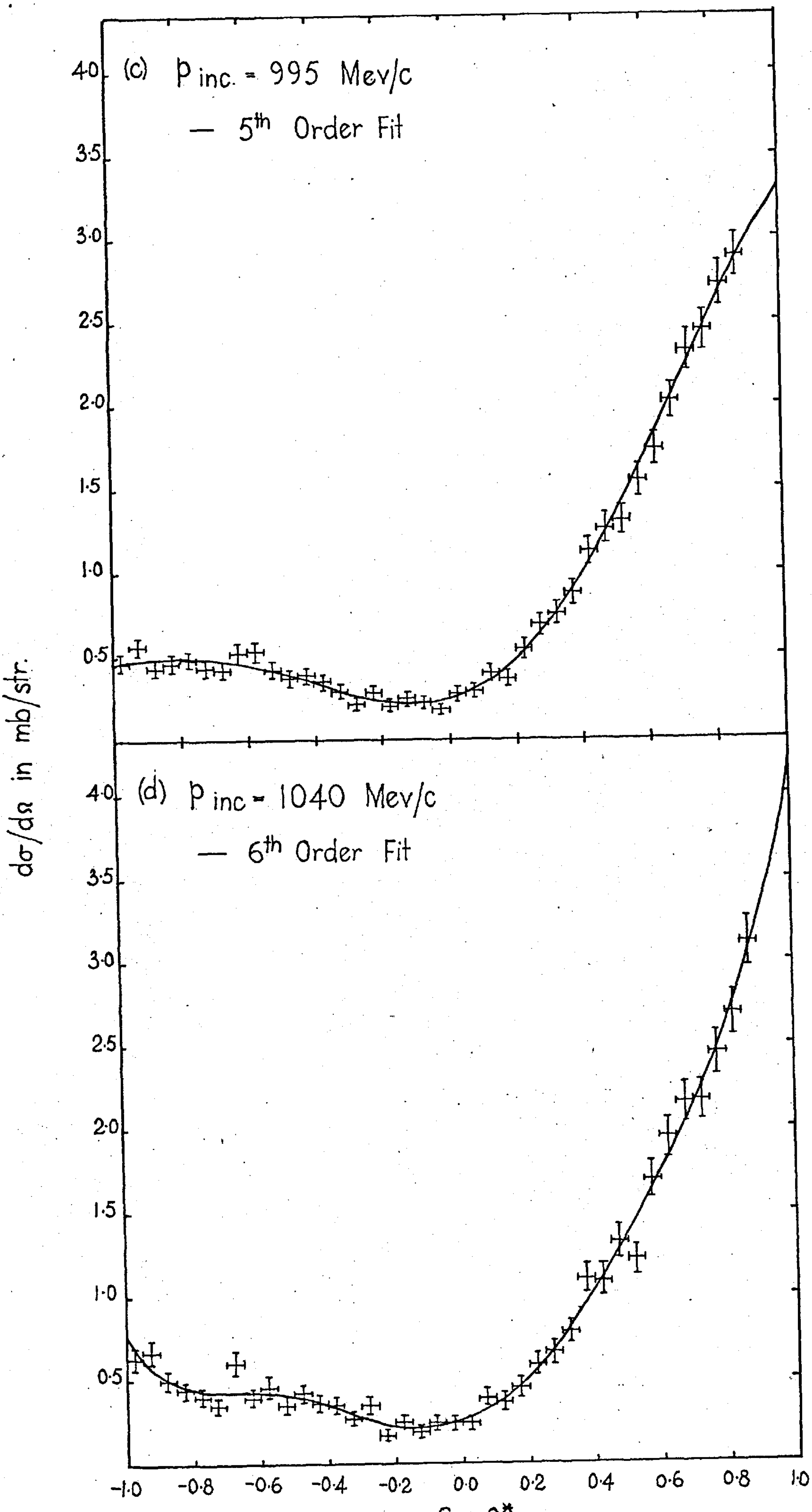
4·0
3·5
3·0
2·5
2·0
1·5
1·0
0·5
(c) P inc. = 995 Mev/c
— 5th Order Fit
dσ/dΩ in mb/str.
4·0
3·5
3·0
2·5
2·0
1·5
1·0
0·5
(d) P inc = 1040 Mev/c
— 6th Order Fit
-1·0
-0·8
-0·6
-0·4
-0·2
0·0
0·2
0·4
0·6
0·8
1·0
Cos θ*

Fig. 3·5

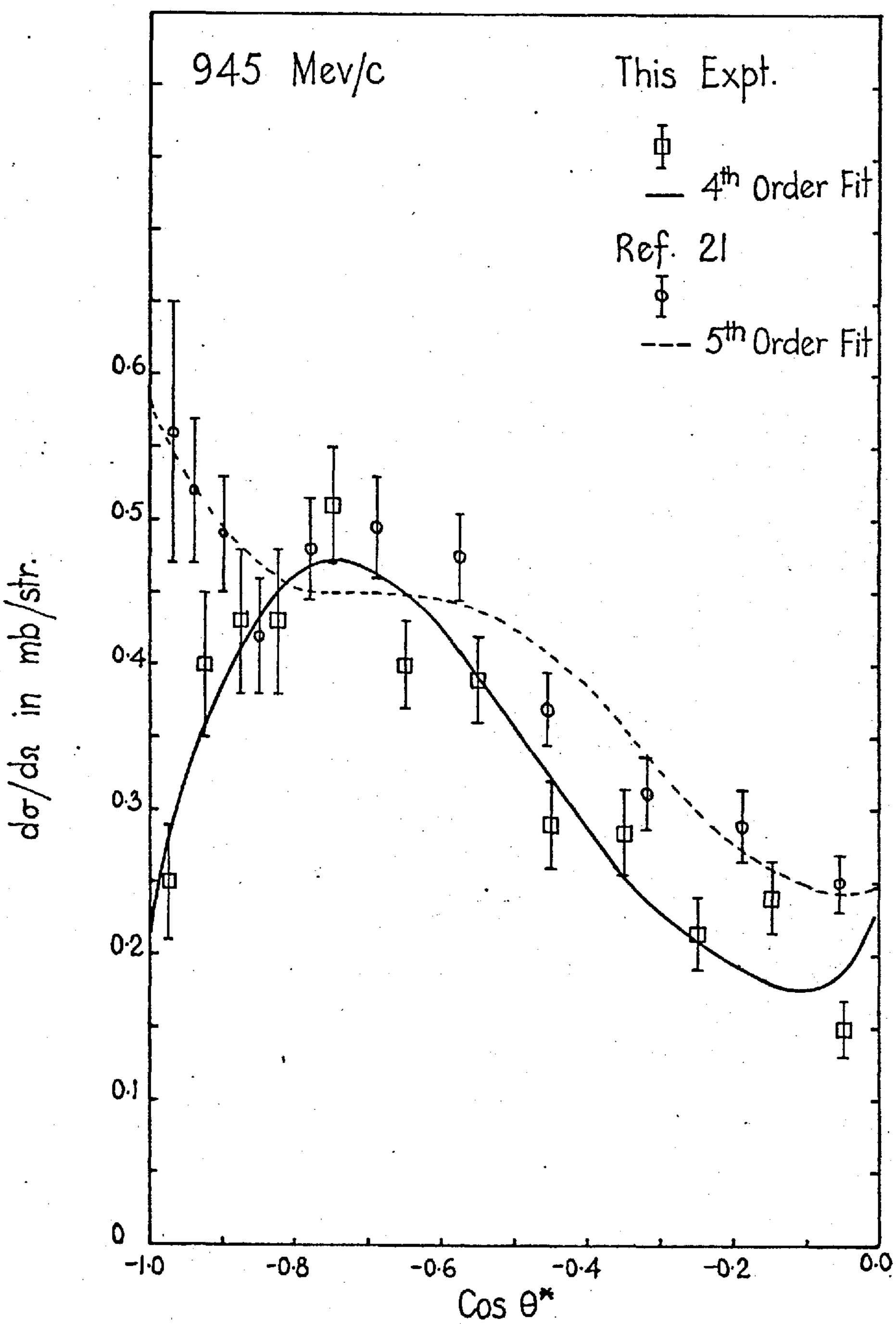
945 Mev/c
This Expt.
4th Order Fit
Ref. 21
5th Order Fit
dσ/dΩ in mb/str.
0
0·1
0·2
0·3
0·4
0·5
0·6
-1·0
-0·8
-0·6
-0·4
-0·2
0·0
Cos θ*

Fig. 3·6

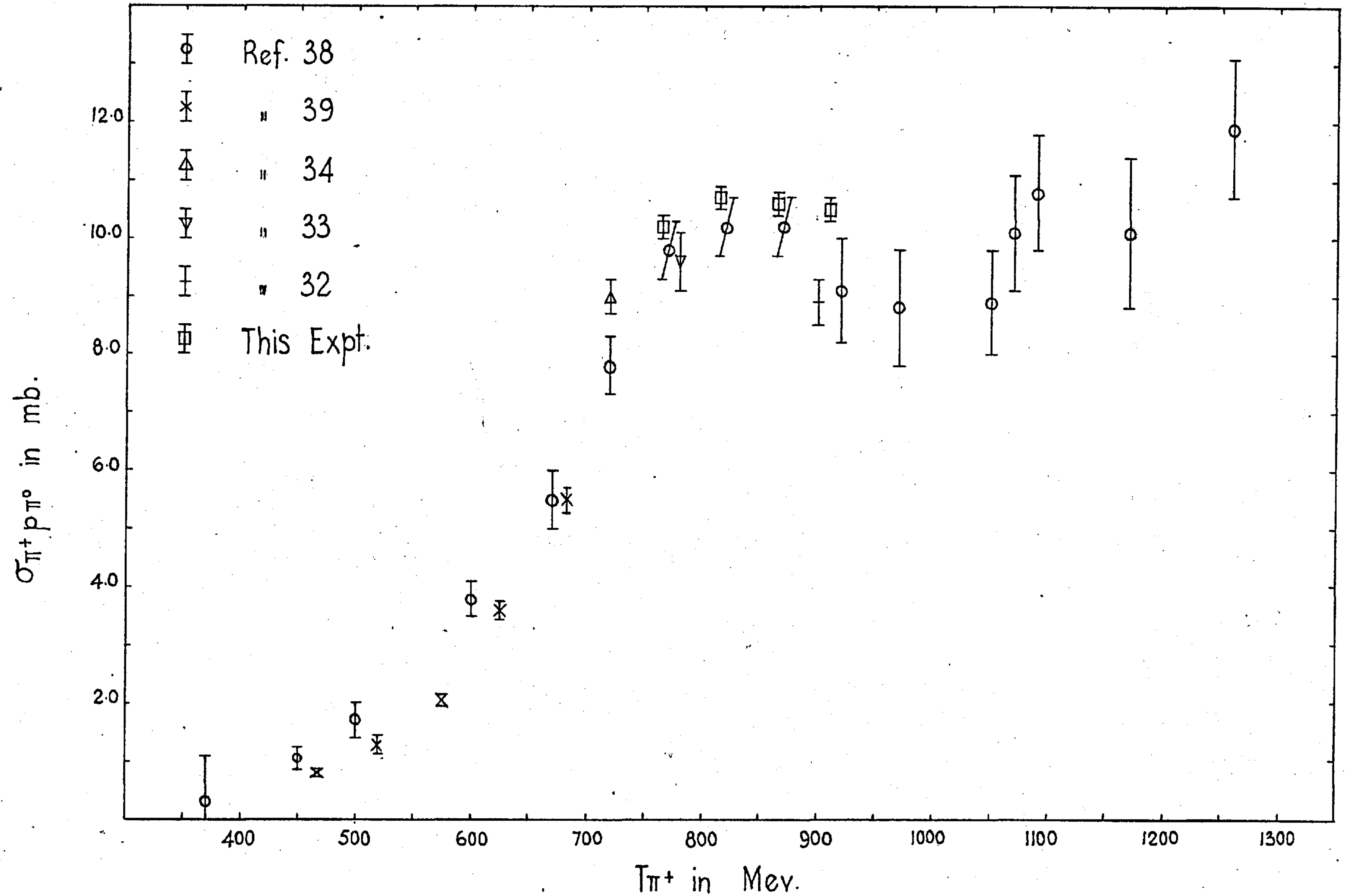
Ref. 38
" 39
" 34
" 33
" 32
This Expt.
12.0
10.0
8.0
6.0
4.0
2.0
$\sigma_{\pi^+ p \pi^0}$ in mb.
400
500
600
700
800
900
1000
1100
1200
1300
T_{π^+} in Mev.

Fig. 3.7

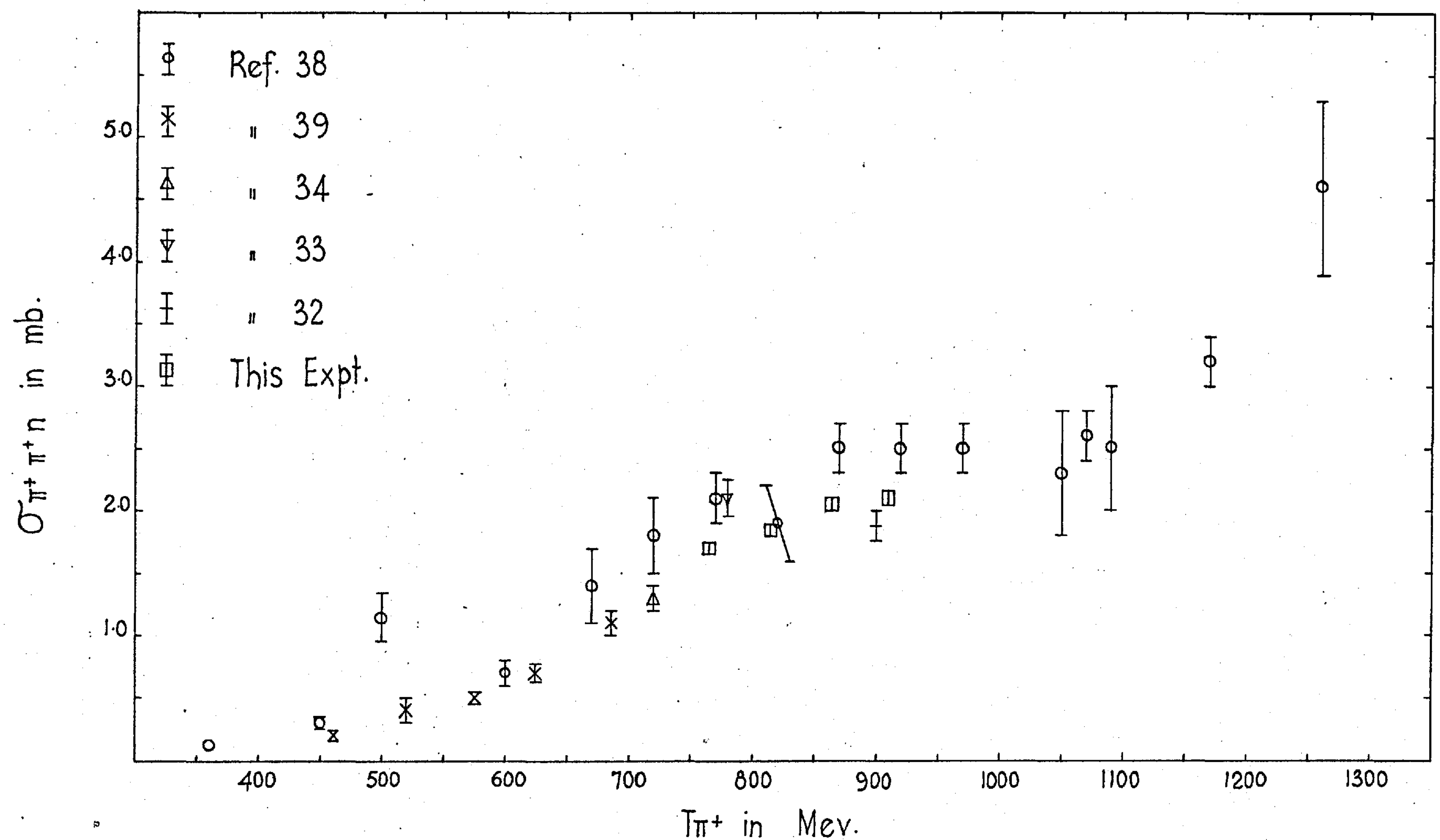
Ref. 38
" 39
" 34
" 33
" 32
This Expt.
5.0
4.0
3.0
2.0
1.0
$\sigma_{\pi^+ \pi^+ n}$ in mb.
400
500
600
700
800
900
1000
1100
1200
1300
T_{π^+} in Mev.

Fig. 3·8

CHAPTER 4

Single-Pion Production - Experimental Results

4.1 Introduction

It has been stated earlier that the dominant inelastic channels in positive-pion proton interactions around 1 GeV/c are the two single pion production channels. To describe completely a process of the type

$$\pi N \longrightarrow \pi_1 \; \pi_2 \; N' \qquad (4.1)$$

one needs to write out an amplitude for the process as a function of five variables. One of these is clearly the centre of mass energy, but the choice of the remaining four variables is by no means commonly agreed upon. The most basic experimental result for a process is the total cross-section for the process at a given centre of mass energy. This is a result one obtains by integrating over the four independent variables in the case of a three-body final state.

Cross-sections obtained for all the inelastic reactions in the present experiment have been presented in an earlier chapter. In section 4.2 the energy variations of these for the single-pion production reactions are discussed. Two variables are usually chosen to be the invariant mass-squared of two two-particle combinations. The invariant mass-squared distributions obtained for the two single pion production reactions at the four incident momenta are discussed in Section 4.3. Simple resonance model fits, based on the Breit-Wigner formula for the decay of the $\Delta(1236)$ and $\rho(765)$ resonances produced in the quasi-two-body intermediate states $\pi\Delta$ and ρp, to the Dalitz plots for the two channels are discussed.

The choice of the remaining two-variables to describe single-pion production processes (4.1) is generally dependent on the model used to fit the data. Olsson and Yodh[14), 16), 17)], in their model, set out to describe the centre of mass production angle distributions relative to the incident pion direction for the final state particles besides the invariant mass-squared distributions. These distributions, obtained in the present experiment, are discussed in Section 4.4. Since the single-pion production reactions are dominated by Δ (1236) production and since the doubly-charged state of the Δ is more copiously produced than the singly-charged state, a selection of $\pi^o \Delta^{++}$ events is made from the overall $\pi^+ p \pi^o$ final state and the centre of mass production angle distribution of the π^o is fitted to a Legendre Polynomial expansion.

An alternative choice of the two angles can be made by defining a frame of reference unique to the three-particle final state and comparing the orientation of the Z-axis in this frame to the Z-axis in a fixed frame. Deler and Valladas[20] choose the Z-axis in the three-body frame to be the normal to the production plane and X-axis to be the direction of π_1 in the production plane. The Z-axis of the fixed frame of reference is along the direction of the incident pion. The variables chosen are the polar angles (Θ, Φ) of the incident pion direction in the three-particle frame - Fig. 4.1. The distributions of Cos Θ and Φ are presented in Section 4.5.

4.2 Energy variation of cross-sections

The values of the cross-sections for the two single-pion production channels for different incident pion energies around the 1 GeV range are plotted in Figures 3.7 and 3.8. The most outstanding feature of these is the dramatic rise in the cross-section for $\pi^+ p \pi^o$ (σ_{+op}) over the centre of mass energy region 1550 MeV to 1620 MeV. The results of the present experiment clearly show that σ_{+op} levels out to a constant value of around 10.5 mb between 1640 MeV and 1700 MeV centre of mass energy. At energies higher than this earlier reported results[38] show a dip in this cross-section reaching a minimum at about 1740 MeV. However, the quoted values of cross-section at these higher energies have large errors compared to the present experiment, and other bubble chamber experiments recently reported[34), 39] at lower energies.

The cross-section for $\pi^+\pi^+ n$ (σ_{++n}), on the other hand, shows a gradual rise with energy from threshold up to about 1700 MeV. The values of σ_{++n}

obtained in the present experiment are about 1-2 standard deviations below previously reported values. The same effect is observed at centre of mass energies lower than the range of the present experiment in recent bubble chamber experiments[34), 39)]. The accuracy of the results of these experiments, including the present experiment, is far greater than the results compiled by Rosenberg and Roper[38)]. As such the value of the ratio $R = \sigma_{+0p}/\sigma_{++n}$ is generally higher than previously obtained. It has been pointed out in the introductory chapter that the value of this ratio was important to the success or failure of the various isobar models used to explain the experimentally observed features of reaction (4.1). The energy variations of R, as experimentally observed, over the range of incident pion energy from threshold to 1300 MeV is shown in Fig. 4.2.

The energy variation of the overall inelastic positive-pion proton cross-section (σ_{in}) is shown in Fig. 4.3. The contribution of σ_{+0p} to σ_{in} clearly dominates the energy variation of the latter. The discussion in Chapter 1 on single pion production around 1 GeV/c suggests that the rapid rise in σ_{+0p} over the range 1550-1620 MeV and the lack of a corresponding rise in σ_{++n} is due to the growing importance of an s-channel partial wave which gives constructive interference between the two states $\pi^0(\pi^+p)$ and $\pi^+(\pi^0p)$ in the $\pi^+p\pi^0$ channel, and destructive interference between $\pi^+_1(\pi^+_2n)$ and $\pi^+_2(\pi^+_1n)$ in the $\pi^+\pi^+n$ channel, where the pion nucleon couplings are the $I = 3/2$ $J^P = 3/2^+$ Δ - states. We shall return to this in the next chapter.

4.3 2-body invariant mass-squared distributions and Resonance production

(a) $\pi^+p\pi^0$ Final state

The π^+ can associate with the proton to form a pure I-spin 3/2 state whereas the π^0 can form a mixture of I-spin 3/2 and 1/2 states with the proton. As such any I = 3/2 pion-nucleon coupling is expected to show up more prominently in the (π^+p) invariant mass-squared distribution than in the (π^0p) distribution. Just such an effect is noticed in the experimental distributions

Figures 4.4 to 4.7, show Dalitz plot distributions and projections obtained for this final state with $M(\pi^+\pi^o)^2$ plotted against $M(\pi^+p)^2$ for the four incident momenta. The first nucleon resonance observed is the I = 3/2, J = 3/2 Δ (1236). The results of the present experiment provide ample evidence for the production of this resonance in π^+p interactions around 1 GeV/c. The Dalitz plots clearly show two bands of high density distribution - centered around the (π^+p) and (π^op) invariant masses of 1210 MeV. Also evident is a generally high concentration of events near the high $(\pi^+\pi^o)$ mass region. The width of the Δ is generally quoted to be 120 MeV. This implies that the effect of Δ production, in both its charged states, is spread over a large area of the Dalitz plot and since the overall amount of phase space is limited by the low centre of mass energy interference effects between the two intermediate states $\pi^o\Delta^{++}$ and $\pi^+\Delta^+$ are expected to play an important role in the region where the two resonance bands overlap. As the available centre of mass energy increases this is expected to diminish in importance as the two resonance bands get more clearly separated on the Dalitz plot. At the high $M_{\pi\pi}{}^2$ end the bands overlap and the high concentration of events in this region is likely to be explained, in part, by the interference effects.

(b) $\pi^+\pi^+n$ Final state

In this final state either pion can couple with the neutron to produce an I-spin 1/2 or an I-spin 3/2 state. The lowest attractive pion-nucleon coupling in I-spin 1/2 is the $N^*(1480)$ with $J^P = \frac{1}{2}^+$. The mass of this is close to the edge of phase space in the present experiment. The Δ resonance is, therefore, the only dominant π-N coupling and it can only be produced in one charged state. The two resonance bands, on a symmetrised Dalitz plot (each event counted twice) are expected to show identical features. Interference effects are still expected to play an important part since the neutron can be coupled to either π^+ to form the Δ^+. Figures 4.8 to 4.11 show the $M(\pi^+\pi^+)^2$ .v. $M(\pi^+n)^2$ distributions.

If the high concentration of events seen in the $\pi^+ p \pi^0$ final state in the high $M(\pi^+\pi^0)^2$ region is entirely due to interference effects a similar concentration might be observed in this final state. It can be seen from Figures 4.8 to 4.11 that no such effect is present in the $\pi^+ \pi^+ n$ final state. This is more clearly demonstrated in Fig. 4.12 where the ratio $R(M_{\pi\pi})$, = $= \frac{d\sigma_{+op}}{dM_{\pi\pi}} \Big/ \frac{d\sigma_{++n}}{dM_{\pi\pi}}$, is shown for the four incident momenta. The rise in R for high values of $M_{\pi\pi}$ clearly implies a greater concentration of events in the $\pi^+ p \pi^0$ than in the $\pi^+ \pi^+ n$ final state. This suggests the production of an attractive $\pi - \pi$ subsystem in the I-spin 1 state. The lowest known such coupling is the ρ-meson with mass 765 MeV and width 125 MeV. The threshold for the production of a meson of this mass is 1.06 GeV/c. The lowest momentum in this experiment is $1\frac{1}{2}$ widths below this threshold. As a result the production of the intermediate state ρ^{+p} is not entirely unlikely.

(c) Resonance Model fit to $\pi^+ p \rightarrow \pi_1 \pi_2 N'$

The dominance of the excitation of resonances decaying to two particles, particularly the I = 3/2, J = 3/2 and M = 1236 MeV Δ resonance, in the experimental Dalitz plots for the reactions (4.1) has been amply demonstrated. We now discuss a model to determine the cross-sections for resonance production in positive-pion proton interactions around 1 GeV/c.

The general reaction (4.1) can be considered as a sum of quasi-two-body production reactions, with subsequent decay of the excited resonance, with three-particle phase space as background. Labelling the final state particles in (4.1) as (1), (2), and (3) and assuming only one possible attractive coupling between each pair of particles, the model assumes the following four processes contributing to the final state:

$$\pi^+ p \longrightarrow 1 + 2 + 3 \text{ (phase space)} \qquad (4.2a)$$

$$\longrightarrow 1 + (23) \qquad (4.2b)$$

$$\longrightarrow 2 + (13) \qquad (4.2c)$$

$$\longrightarrow 3 + (12) \qquad (4.2d)$$

The quasi-two-body processes, (4.2b) to (4.2d), split the overall three-particle production vertex into a two-body production vertex connected via a propagator to a decay vertex. The model, following the usual 'isobar'-type models, assumes that the recoil particle has moved far away from the interaction region before the excited resonance decays - that is, further final state interactions are ignored.

The excited pion-nucleon combinations - (13) and (23) - are assumed to be the I = 3/2, J = 3/2 resonances characterised by their charge. The two-pion combination in (4.2d) is assumed to be the I = 1, $J^P = 1^-$ ρ-meson. This process contributes only to the $\pi^+ p \pi^0$ final state. No attractive I = 2 $(\pi\pi)$ coupling is assumed in the $\pi^+\pi^+ n$ final state. The quasi-two-body processes and 3-particle production via phase space are assumed to be incoherent.

Process (4.2a) is thus assumed to give a uniform density distribution over the Dalitz plot within a boundary defined by

$$Y^2X + X^2Y - t_1XY + t_2X + t_3Y + t_4 = 0 \tag{4.3}$$

where X, Y are the invariant mass-squared values of the (23) and (12) combinations respectively, and

$$\begin{aligned} t_1 &= E^2 + \sum_{i=1}^{3} m_i^2 \\ t_2 &= (m_3^2 - m_2^2)(E^2 - m_1^2) \\ t_3 &= (m_1^2 - m_2^2)(E^2 - m_3^2) \\ t_4 &= (m_2^2E^2 - m_1^2m_3^2)(E^2 - m_1^2 + m_2^2 - m_3^2). \end{aligned}$$

E is the centre of mass energy and m_i is the mass of the i^{th} particle. For processes (4.2b) to (4.2d) we assume, following M. Olsson[40], that the amplitude for the production of a resonance, in the (ij) particle combination, and its subsequent decay is

$$T_k = A_k R_k(M) \tag{4.4}$$

where A_k is the quasi-two-body production, (k + (ij)), amplitude and R_k is the rescattering amplitude incorporating the propagator and the decay vertex and M is the invariant mass of the excited two-body combination. Neglecting angular momentum effects the rescattering amplitude is given by Jackson[41] as

$$R_k(M) \propto \left(\frac{M}{q}\right)^{\frac{1}{2}} \frac{(M_r \Gamma)^{\frac{1}{2}}}{(M_r^2 - M^2) - iM_r\Gamma} \left[W(\cos\theta_k^*)\right]^{\frac{1}{2}} \qquad (4.5)$$

where q is the momentum of the decay particles in the rest frame of the (ij) subsystem, M_r is the mass of the resonance and Γ is the mass-dependent full-width given by

$$\Gamma = \Gamma_o \left(\frac{q}{q_o}\right)^{2l+1} \frac{\rho(M)}{\rho(M_r)} \qquad (4.6)$$

with Γ_o as the quoted full-width and l the relative orbital angular momentum between the decay particles. $\rho(M)$ is a slowly varying factor which is empirically determined. We use the form suggested by Glashow and Rosenfeld[42) for baryon resonances $\qquad \rho(M) = M^{-1}(X^2+q^2)^{-l} \qquad (4.6a)$

with X = 0.35 GeV. Combining (4.6) and (4.6a) the final form for the width is

$$\Gamma = \Gamma_o \left(\frac{q}{q_o}\right)^{2l} \left(\frac{M_r}{q_o}\right)\left(\frac{q}{M}\right) \frac{(X^2+q_o^2)^l}{(X^2+q^2)^l} \qquad (4.7)$$

The factor $(\frac{q}{m})$ represents the phase space distribution for the decay particles in the rest frame of the sub-system. Since the density distribution on the Dalitz plot is being fitted the final form for the fitted density distribution should be free of any production or decay phase space factors - hence, the factor $(\frac{m}{q})^{\frac{1}{2}}$ in (4.5). The factor $(\frac{q}{q_o})^{2l}$ gives the approximate effect of the angular momentum barrier on the width of the resonance. For the 1^- ρ-meson we use the form obtained by Jackson[41) from lowest order perturbation theory calculations

$$\rho(M) = M^{-1} \qquad (4.8)$$

The function W $(\cos\theta_k^*)$ in (4.5) describes the distribution of the angle, θ_k^* , between the decay momentum direction in the sub-system rest frame and the direction of motion of the sub-system in the centre of mass. For each excited two-body resonance we parametrise it as

$$W(\cos\theta_k^*) = 1 - \beta_k \cos^2\theta_k^* \qquad (4.9)$$

with the parameters β_k to be determined by fitting the experimental data.

The experimental (π^+p) mass-squared distributions (figures 4.4 to 4.7) show the Δ^{++} resonance peaking at around 1200-1210 MeV - far below the mass of the resonance (1236 MeV). The form (4.7) for the mass dependent width causes the peak to shift below the resonance mass. This shift is found to be insufficient to explain the position of the peak. The quasi-two-body production amplitude A_k must therefore contain the cause of the extra shift in the (πN) peaks.

The ρ exchange model of Stodolsky and Sakurai[43] has had a great deal of success in explaining Δ production in the analogous reaction[44]

$$K^+ p \longrightarrow K^o p \pi^+ \tag{4.10}$$

where the peak in (π^+p) invariant mass is around 40 MeV below the quoted mass of the Δ. The Stodolsky and Sakurai model introduces an extra factor p_K^2 , where p_K is the momentum of the recoiling K^o in the centre of mass besides $|R_{\pi^+p}|^2$ and various phase space factors in the predicted invariant $(\pi^+ p)$ mass distribution. This has the effect of weighting more strongly the lower values of $M_{p\pi^+}$ and hence causing a further shift in the position of the Δ peak. So in our model we introduce an extra factor p_k , the momentum of the recoiling pion k, in the amplitude for Δ production. Thus, for Δ production we have $T_k = a_k p_k R_k$ with k = 1, 2 and for ρ^+ production $T_3 = A_3R_3$.

The main aim of this model is to extract the amount of Δ production in (4.1). So any $(\pi\pi)$ coupling introduced (the ρ-meson in $\pi^+p\,\pi^o$ final state) is treated as incoherent background along with the 3-particle phase space. Writing $a_k = \alpha_k\, e^{i\phi_k}$ the fitted density distribution on the Dalitz plot is

$$\frac{d^2N}{dX\,dY} = C\Big[\big|\alpha_1 p_1\, e^{i\phi_1} R_1 + \alpha_2 p_2\, e^{i\phi_2} R_2\big|^2 + \alpha_3^2\,|R_3|^2 + \alpha_p^2\, P\Big] \tag{4.11}$$

where P is the constant phase space distribution and α_p^2 is the fraction of phase space. C is an overall constant of normalisation which ensures that, for a given set of values of the parameters,

$$\iint_{\text{DALITZ plot}} \frac{d^2N}{dX\,dY}\, dX\, dY = \text{Total No. of events in the channel.}$$

The lower and upper limits of X and Y, fixed by the particle masses and the total centre of mass energy, are used to define an N x N grid across the Dalitz plot. The data fitted by the model are the experimental numbers of events in each rectangle with at least one corner within the boundary defined by (4.3). For a given set of values of the free parameters the fitted number of events in each significant rectangle is determined by integrating (4.11) over the area of the rectangle within the boundary. This is achieved by dividing the rectangle into n x n subrectangles. The contribution of each subrectangle is added up if its centre lies within the boundary. No approximation is therefore involved in determining the fitted number of events for rectangles lying wholly within the boundary. For rectangles lying on the boundary the number of events predicted by the model are reasonably accurately determined if the sub-division is fine enough. To achieve this the predicted number of events in the boundary rectangles is determined by subdividing each rectangle into 2n x 2n subrectangles compared to an n x n subdivision of the rectangles lying wholly inside the boundary.

The choice of the square grid is governed by the fitting technique used. The amount of resonance production in reaction (4.1) was determined by minimising a χ^2 over the Dalitz plot. The value of N was thus chosen to give a sufficient number of events in each significant rectangle for the assumption of Gaussian errors on the experimental numbers to be valid. The shape of the Dalitz plot boundary - (4.3) - makes it impossible to ensure this for all the rectangles on the boundary. The experimental spread in the centre of mass energy strongly affects the distribution of events in the boundary region. Rectangles on the boundary with less than five events are therefore not used in the fit.

For the $\pi^+ p \pi^0$ final state a 15 x 15 grid ensured that all rectangles within the boundary had more than five events. The following 7 free parameters are determined by fitting the Dalitz distribution at each of the four momenta:

(i) Moduli of resonance production amplitudes -

α_1 - for $\pi^+ p \longrightarrow \pi^o \Delta^{++}$

α_2 - for $\longrightarrow \pi^+ \Delta^+$ and

α_3 - for $\longrightarrow p \rho^+$. Since overall normalisation - eqn. (4.11) - is imposed α_p is fixed to unity.

(ii) Phase difference between the coherent Δ^{++} and Δ^+ production processes - $\phi = \phi_2 - \phi_1$.

(iii) Resonance decay distribution parameters -

β_1, β_2 and β_3 for Δ^{++}, Δ^+ and ρ^+ respectively.

The amounts of Δ and ρ production obtained from the best fit are presented in Table 4.1a along with the goodness-of-fit parameter ($G = \chi^2$/No. of degrees of freedom) values. Table 4.1b shows the values of the resonance decay distribution parameters determined by the fit. These are compared with the value predicted by the Stodolsky and Sakurai model[43), 45)]. The values determined by the fits are reasonably consistent with the ρ-exchange model prediction. The invariant $M^2_{p\pi^+}$ and $M^2_{\pi^+\pi^o}$ distributions obtained from the fits are shown in Figures 4.4 to 4.7 (dashed curves on the Dalitz plot projections).

For the $\pi^+\pi^+ n$ final state (with about 1/6th the cross-section of $\pi^+ p \pi^o$) a suitable distribution of events for a χ^2 type of fit was achieved by an 8 x 8 grid. Bose symmetry requirements for this final state reduce the number of free parameters to two:

(i) α-modulus of Δ^+ production amplitude and

(ii) β - the Δ^+ decay distribution parameter.

The amounts of Δ^+ production in the $\pi^+ \pi^+ n$ final state, the goodness-of-fit parameter values and the values of the Δ^+ decay distribution parameter in this channel for the four momenta are presented in Table 4.1c. The fitted invariant $M^2_{n\pi^+}$ and $M^2_{\pi^+\pi^+}$ distributions are shown in Figures 4.8 to 4.11. This simple model is obviously unable to explain the dip in the middle of the invariant

$M^2_{\pi^+ n}$ distribution present at all incident momenta.

The overall Δ and ρ production cross-sections are presented in Table 4.2 along with the fractions of single pion production reaction these resonance production processes explain. The estimate of total resonance production obtained by this simple model is close to 75% of the total single pion production reaction at each of the four momentum. These fits have ignored the possibility of any strong $I = \frac{1}{2}$ pion nucleon coupling which would contribute mainly to the $\pi^+\pi^+n$ final state. The large amount of phase space required by the fits to this channel could equally easily be replaced by such a coupling. This lends support to attempts to partial wave analyse the single pion production reaction (4.1) on the basis of quasi-two-body production of resonances (subsystems) of known spin and parity. Just such an attempt is presented in the next chapter.

4.4 Production Angle Distributions

The production angle - θ^*_i - of a particle 'i' in the final state is defined as the angle between the direction of motion of the particle and the incident pion direction in the centre of mass frame -

$$\cos \theta^*_i = \frac{\vec{p}_i \cdot \vec{p}}{|\vec{p}_i||\vec{p}|}, \text{ where } p_i \text{ is the three-momentum of particle 'i'}$$

and p the three-momentum of the incident pion in the centre of mass.

(a) $\pi^+ p\, \pi^0$ final state

Figures 4.13 to 4.16 show the production angle distributions for the three final state particles obtained in the present experiment. The main feature of the π^0 distribution is the preferentially forward ($\cos \theta^*_{\pi^0} = 1.0$) emission of the π^0. With increasing incident energy this shows a tendency to turn over at $\cos \theta^* = 1.0$. A secondary peak in the backward direction also appears to develop with increasing incident energy. The ρ exchange model of Stodolsky and Sakurai[43] for Δ^{++} production predicts a dipping differential cross-section near $\cos \theta^*_{\pi^0} = 1.0$. The model is, however, unable to explain the significant population in the backward hemisphere, where a secondary peak develops even when events outside the Δ^{++} mass region ($1.16 < M_{p\pi^+} < 1.30$) are ignored. Tautfest and Willman[46] are able to get reasonable agreement with the experimental $\cos\theta^*_{\pi^0}$ distributions for the reaction $\pi^+ p \rightarrow \Delta^{++} \pi^0$ at 0.94, 1.11 and 1.265 GeV/c by imposing a u-channel nucleon exchange process as background to the t-channel ρ -exchange process.

The π^+ production angle distributions are all reasonably symmetric with respect to the forward and backward hemispheres with a dominant $\cos^2\theta$ term in the expansion. The $\cos\theta^*_p$ distributions show the proton being emitted preferentially backwards with a dominant $\cos\theta$ term which Olsson and Yodh[14), 16), 17), 40)] explain as the result of interference between a dominent $D^-_{3/2}$ wave in the initial state and a small $P^+_{\frac{1}{2}}$ wave.

Following Kraybill et al.[47] we select $\pi^0\ \Delta^{++}$ events from the overall $\pi^+ p\, \pi^0$ final state with $1.16 < M_{p\pi^+} < 1.30$ and fit the $\cos\theta^*_{\pi^0}$ distribution obtained to the expansion

$$\frac{d\sigma}{d\cos\theta^*_{\pi^0}} = \frac{\pi \lambda\!\!\!^{-2}}{2}\left[C_0 + \sum_{l=1}^{L} C_l P_l(\cos\theta^*_{\pi^0})\right] \qquad (4.12)$$

The order (L) of the highest Legendre polynomial, P_l , with a significantly non-zero coefficient C_l in the above expansion, determined by the F-ratio test, is found to be 4, 6, 6 and 7 at the four incident pion momenta. The values of the coefficients are presented in Table 4.3 and are plotted in Figure 4.17. These values are in reasonable agreement with previous results[47] with the exception of C_1 which is significantly greater. Neglecting interference effects between the $\pi^0\ \Delta^{++}$ and the $\pi^+\Delta^+$ states (estimated to be a 10 - 15% effect at 800 MeV), Kraybill et al. set out a formalism relating the coefficients with the amplitudes for the L L$'$ (2J) transition amplitudes for the reaction $\pi^+ p \longrightarrow \pi^0\ \Delta^{++}$. L and L$'$ are the initial and final state orbital angular momenta and J is the total spin. Qualitative conclusions can be drawn about the relative strengths of the transition amplitudes from a study of the energy variation of the Legendre polynomial coefficients. We shall return to these conclusions in the next chapter where a partial wave analysis of single pion production is presented.

(b) $\pi^+ \pi^+ n$ final state

The centre of mass production angle distributions for the π^+ and the n are shown in Figures 4.18 to 4.21. The π^+ distributions are symmetric showing a dominant $\cos^2\theta$ term. The $\cos\theta_n^*$ distribution shows a slight preference towards the backward direction for neutron emission. The backward to forward asymmetry is 1.42 : 1 at 895 MeV/c and drops to 1.15 at 1040 MeV/c. At the highest momentum the distribution, apart from a pronounced peak at $\cos\theta^* = -1.0$, is almost uniform.

4.5 The (Θ , Φ) Distribution

It has been pointed out that the first step in the partial wave analysis of elastic scattering is the determination of the coefficients of a Legendre polynomial expansion fit to the differential cross-section distribution as a function of the centre of mass scattering angle. The generalisation of this to the three particle final state requires a judicious choice of the five independent variables describing the state, such that the effects of total angular momentum conservation can be separated from the dynamics of the interaction. Besides the two squared invariant masses - $S_1 = M_{23}^2$ and $S_2 = M_{13}^2$ - a convenient choice is the three Euler angles connecting a fixed frame to a frame attached to the three particles. It is usual to choose the Z-axis of the former along the direction of the incident pion in the centre of mass system. When the scattering takes place off unpolarised targets the scattering is independent of the choice of the X-axis of this frame. This leaves only two Euler angles to study. The Z-axis of the frame fixed to the final state is chosen to be the direction of the normal to the plane containing the three particles (the production or the Dalitz plane) and the X-axis is chosen along the direction of one of the three particles. For reactions of the type (4.1) M. De Beer et al.[48] choose the nucleon direction as the X-axis. This is perhaps the most appropriate choice since the nucleon couples strongly with both the pions to form resonating two-body subsystems.

The two angles concerned are then the two polar angles (Θ, Φ) - Figure 4.1 - of the incident pion in this frame. The differential cross-section for given values of S_1 and S_2 can be expanded in spherical harmonics in cos Θ and Φ as:

$$\frac{d\sigma}{dS_1 dS_2 d\cos\Theta\, d\Phi} = \sum_L \sum_{M=-L}^{M=L} \left[A_L^M(S_1, S_2) \cos M\Phi + B_L^M(S_1, S_2) \sin M\Phi \right] \times$$
$$\times P_L^M(\cos\Theta) \qquad (4.13)$$

Integration of (4.16) over the Dalitz plot (S_1 and S_2) gives

$$\frac{d\sigma}{d\cos\Theta\, d\Phi} = \sum_L \sum_{M=-L}^{M=L} \left[C_L^M \cos M\Phi + D_L^M \sin M\Phi \right] P_L^M(\cos\Theta) \qquad (4.14)$$

Parity conservation requires the moments, C_L^M and D_L^M, for odd values of L + M to be consistent with zero. The values of the moments for even values of L + M, as obtained in this experiment, are presented in Table 4.4 for the $\pi^+ p \pi^0$ final state and in Table 4.5 for $\pi^+ \pi^+ n$ final states for values of L up to 6. The moments for L = 7 and higher are consistent with zero. The significance of this and of the energy variation of the moments, shown in Figure 4.22 (where the moments consistent with zero at all four momenta are not shown), is discussed in the next chapter.

Table 4.1a

$\pi\Delta$ (1236) and $p\rho^+$ (765) production in $\pi^+p \rightarrow \pi^+p\pi^0$

Momentum (MeV/c)	$\sigma_{\pi^+p \rightarrow \pi\Delta}$ (mb)	$\sigma_{\pi^+p \rightarrow p\rho^+}$ (mb)	$\sigma_{\pi^+p \rightarrow \pi^+p\pi^0}$ (Total in mb)	$G = \chi^2/ND$
895	7.47 ± 0.23	1.14 ± 0.05	10.22 ± 0.17	1.62
945	8.18 ± 0.75	1.05 ± 0.58	10.66 ± 0.16	1.42
995	7.43 ± 0.61	1.53 ± 0.21	10.58 ± 0.16	1.69
1040	6.98 ± 0.50	1.66 ± 0.15	10.50 ± 0.18	1.60

Table 4.1b

Resonance decay distributions - $(1-\alpha\cos^2\theta^*)$

α for resonances→ / Momentum (MeV/c)	$\Delta^{++} \rightarrow p\pi^+$	$\Delta^+ \rightarrow p\pi^0$	ρ-exchange model prediction for Δ	$\rho^+(765) \rightarrow \pi^+\pi^0$
895	0.46 ± 0.05	0.85 ± 0.13	0.6	-20.22 ± 1.32
945	0.50 ± 0.04	0.61 ± 0.11	0.6	- 9.41 ± 9.17
995	0.60 ± 0.04	0.42 ± 0.19	0.6	- 1.30 ± 0.61
1040	0.59 ± 0.05	0.47 ± 0.17	0.6	0.28 ± 0.21

Table 4.1c

$\pi^+\Delta^+$ production in $\pi^+p \rightarrow \pi^+\pi^+n$ and $\Delta^+ \rightarrow n\pi^+$ decay distribution - $(1-\alpha\cos^2\theta^*)$

Momentum (MeV/c)	$\sigma_{\pi^+p \rightarrow \pi^+\Delta^+}$ (mb)	$\sigma_{\pi^+p \rightarrow \pi^+\pi^+n}$ (total in mb)	α for $\Delta^+ \rightarrow n\pi^+$	$G = \chi^2/ND$
895	0.36 ± 0.08	1.70 ± 0.06	-0.02 ± 0.44	1.54
945	0.61 ± 0.08	1.83 ± 0.06	0.32 ± 0.21	2.02
995	0.19 ± 0.06	2.03 ± 0.06	0.91 ± 0.43	2.34
1040	0.53 ± 0.09	2.10 ± 0.07	0.61 ± 0.23	2.01

Table 4.2

Resonance Production in $\pi^+ p \to \pi_1 \pi_2 N'$

Momentum (MeV/c)	$\pi^+ p \to \pi\Delta$ in mb	$\pi^+ p \to \rho^+ p$ in mb	Total resonance production cross-section (mb)	Total 1-π production cross-section mb	% age of resonance production
895	7.83 ± 0.24	1.14 ± 0.05	8.97 ± 0.24	11.92 ± 0.18	75.2
945	8.79 ± 0.75	1.05 ± 0.58	9.84 ± 0.94	12.49 ± 0.17	78.8
995	7.62 ± 0.69	1.53 ± 0.21	9.15 ± 0.65	12.63 ± 0.17	72.5
1040	7.51 ± 0.51	1.66 ± 0.15	9.17 ± 0.53	12.60 ± 0.19	72.8

Table 4.3

P_{Lab} in MeV/c $\rightarrow$	895		945		995		1040	
$l \downarrow$	C	ΔC	C	ΔC	C	ΔC	C	ΔC
0	1.37	0.03	1.47	0.03	1.52	0.03	1.51	0.03
1	0.94	0.04	1.08	0.02	1.23	0.04	1.34	0.05
2	0.22	0.05	0.37	0.05	0.52	0.06	0.77	0.06
3	0.02	0.06	-0.18	0.06	-0.09	0.07	-0.14	0.06
4	-0.21	0.07	-0.23	0.07	-0.42	0.07	-0.54	0.08
5	-	-	-0.14	0.08	-0.12	0.08	-0.35	0.10
6	-	-	-0.17	0.08	-0.02	0.06	-0.54	0.11
7	-	-	-	-	-	-	-0.28	0.11

Table 4.4

P_{Lab} in MeV/c →			895		945		995		1040	
L	M	C/D	C_L^M/D_L^M x 10^{-3}	Δ	C_L^M/D_L^M x 10^{-3}	Δ	C_L^M/D_L^M x 10^{-3}	Δ	C_L^M/D_L^M x 10^{-3}	Δ
		C	68	2	72	2	80	2	85	3
1	1	D	20	3	20	2	27	2	28	3
2	0	C	17	4	6	2	1	4	-20	4
		C	10	3	13	2	18	3	19	3
2	2	D	7	3	8	2	10	3	11	3
		C	8	3	7	2	11	3	13	3
3	1	D	-1	3	-4	2	0	2	-1	3
		C	5	3	3	2	6	3	6	3
3	3	D	-2	3	-1	2	0	3	1	3
4	0	C	-5	4	-7	3	-18	4	-18	4
		C	3	3	3	2	5	3	10	3
4	2	D	6	2	1	2	4	3	6	3
		C	3	3	2	2	6	3	6	3
4	4	D	1	3	-2	2	0	3	-1	6
		C	-4	3	-5	2	-1	3	-6	3
5	1	D	4	3	-4	2	-2	2	-6	3
		C	3	3	0	2	4	3	5	3
5	3	D	6	3	4	2	2	3	11	3
		C	0	3	6	2	4	2	6	3
5	5	D	4	3	2	2	-2	3	-5	3
6	0	C	8	4	12	2	0	4	20	4
		C	-5	3	-5	2	-1	3	-7	3
6	2	D	4	3	0	2	0	3	-4	3
		C	-2	3	0	2	3	3	0	3
6	4	D	3	3	3	3	-1	3	5	3
		C	-3	3	5	2	5	3	6	3
		D	-1	3	-1	2	1	2	1	3

<u>Table 4.5</u>

P_{Lab} in MeV/c →			895		945		995		1040	
L	M	C/D	C_L^M/D_L^M x 10^{-3}	Δ	C_L^M/D_L^M x 10^{-3}	Δ	C_L^M/D_L^M x 10^{-3}	Δ	C_L^M/D_L^M x 10^{-3}	Δ
1	1	C	46	7	26	6	21	6	20	6
		D	1	6	-2	6	14	6	-4	6
2	0	C	-19	9	-29	7	-28	8	-48	8
2	2	C	17	7	12	6	13	6	12	6
		D	-7	6	1	6	-2	6	-2	6
3	1	C	-24	6	-6	6	-13	6	-9	6
		D	1	6	-12	5	-6	5	3	6
3	3	C	2	7	-2	6	-4	6	10	6
		D	8	7	-1	6	-1	6	9	6
4	0	C	-7	9	-31	8	1	8	3	8
4	2	C	-3	6	12	6	15	6	16	6
		D	-2	6	-8	6	-1	6	3	6
4	4	C	8	7	-3	6	-6	6	7	6
		D	6	7	5	6	-3	6	-1	6
5	1	C	2	7	-4	6	13	6	-5	6
		D	-7	6	5	5	4	5	1	5
5	3	C	0	7	-8	6	0	6	2	6
		D	-9	6	-3	6	2	6	-5	6
5	5	C	3	7	9	6	10	6	2	6
		D	-5	6	0	6	-5	6	11	6
6	0	C	-2	9	3	8	-10	8	-4	8
6	2	C	-5	7	0	6	0	6	-3	6
		D	2	6	6	6	-1	6	0	6
6	4	C	-2	7	-8	6	-5	6	-6	6
		D	-1	7	2	6	-3	6	-1	6
6	6	C	1	7	2	6	-3	6	-1	6
		D	-6	7	0	6	-8	6	4	6

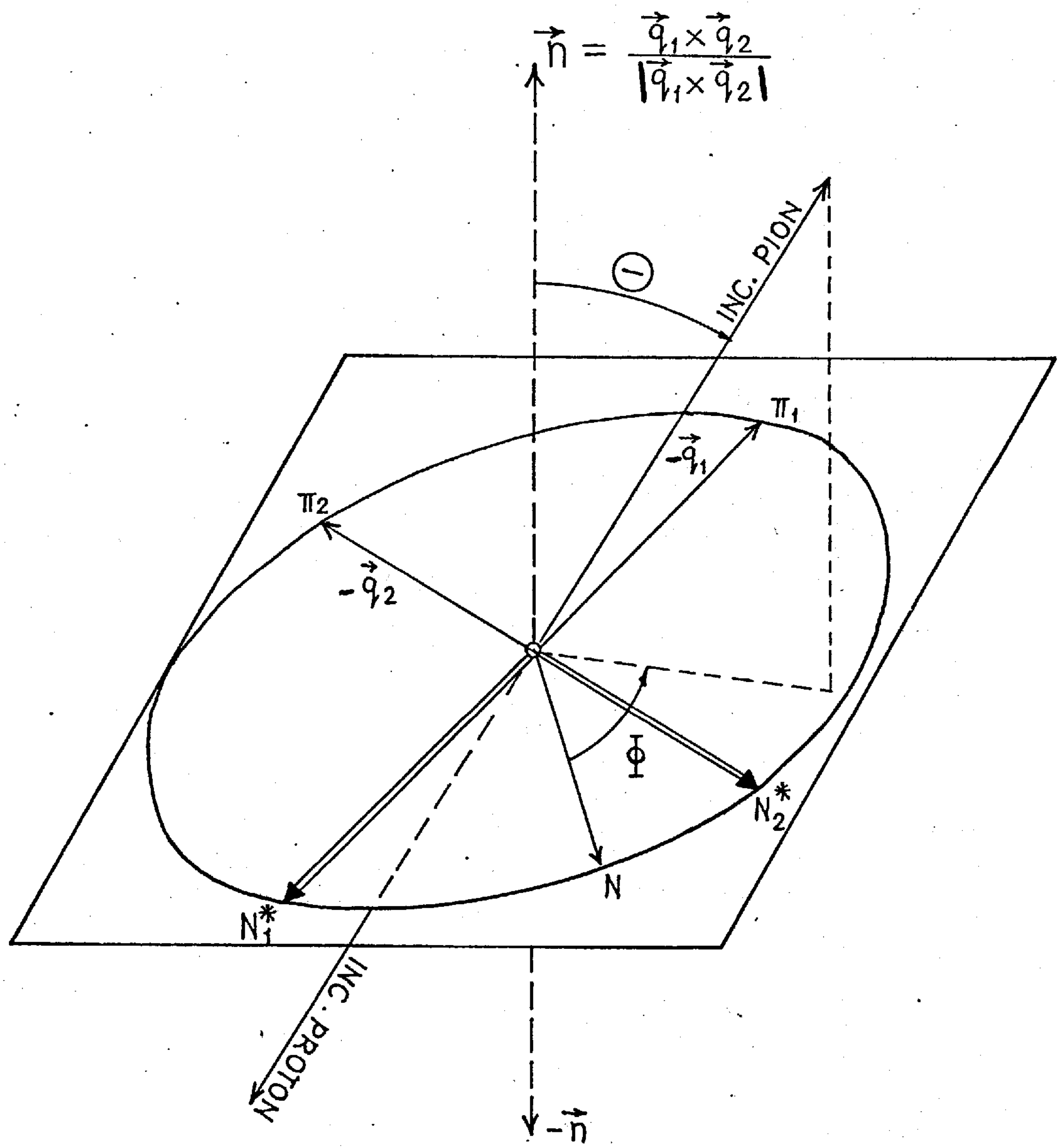

$\vec{n} = \frac{\vec{q}_1 \times \vec{q}_2}{|\vec{q}_1 \times \vec{q}_2|}$
INC. PION
Θ
π_1
$-\vec{q}_1$
π_2
$-\vec{q}_2$
Φ
N_2^*
N
N_1^*
INC. PROTON
$-\vec{n}$

Fig. 4·1

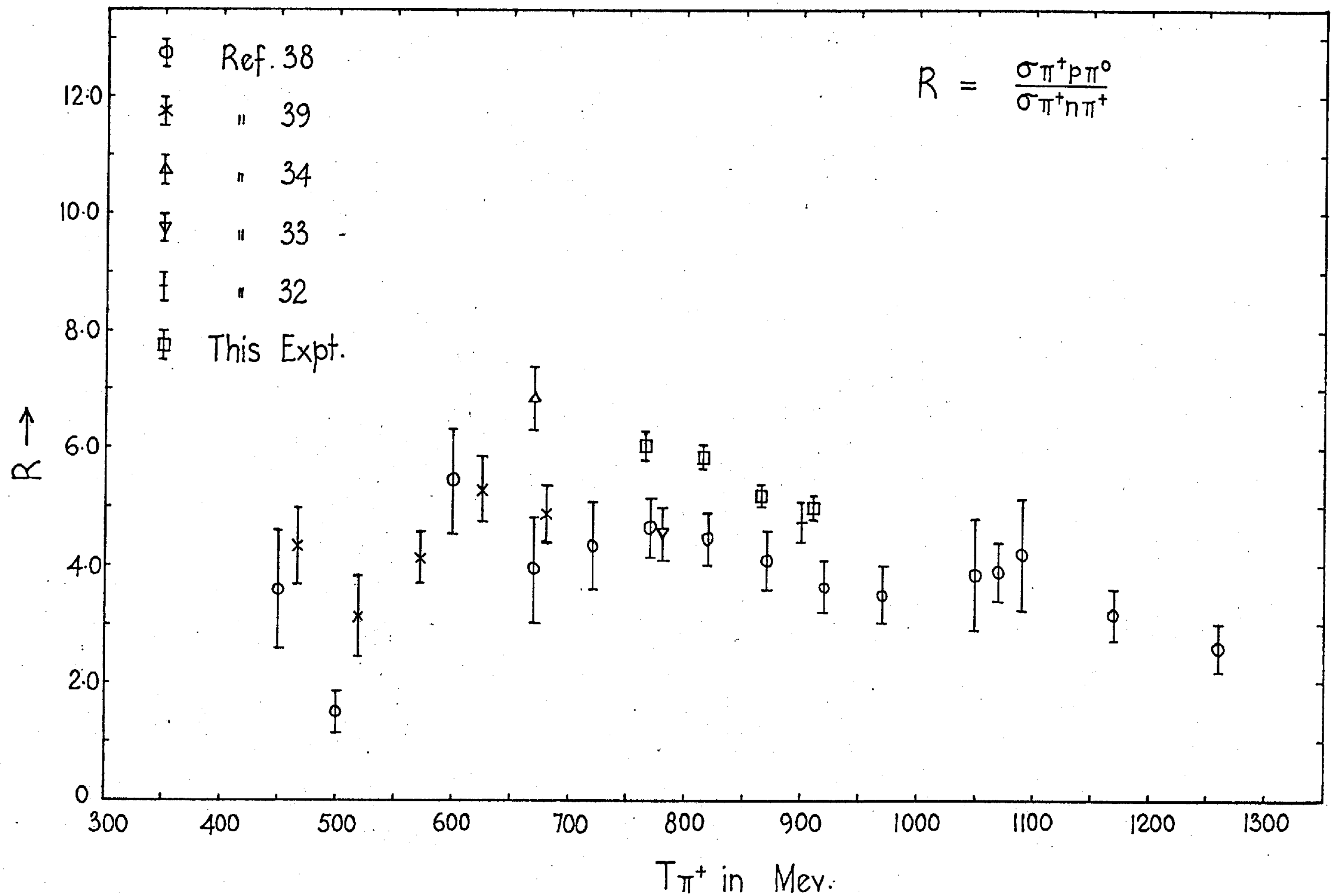
Ref. 38
" 39
" 34
" 33
" 32
This Expt.
$R = \frac{\sigma_{\pi^+ p \pi^0}}{\sigma_{\pi^+ n \pi^+}}$
R ↑
12·0
10·0
8·0
6·0
4·0
2·0
0
300
400
500
600
700
800
900
1000
1100
1200
1300
T_{π^+} in Mev.

Fig. 4·2

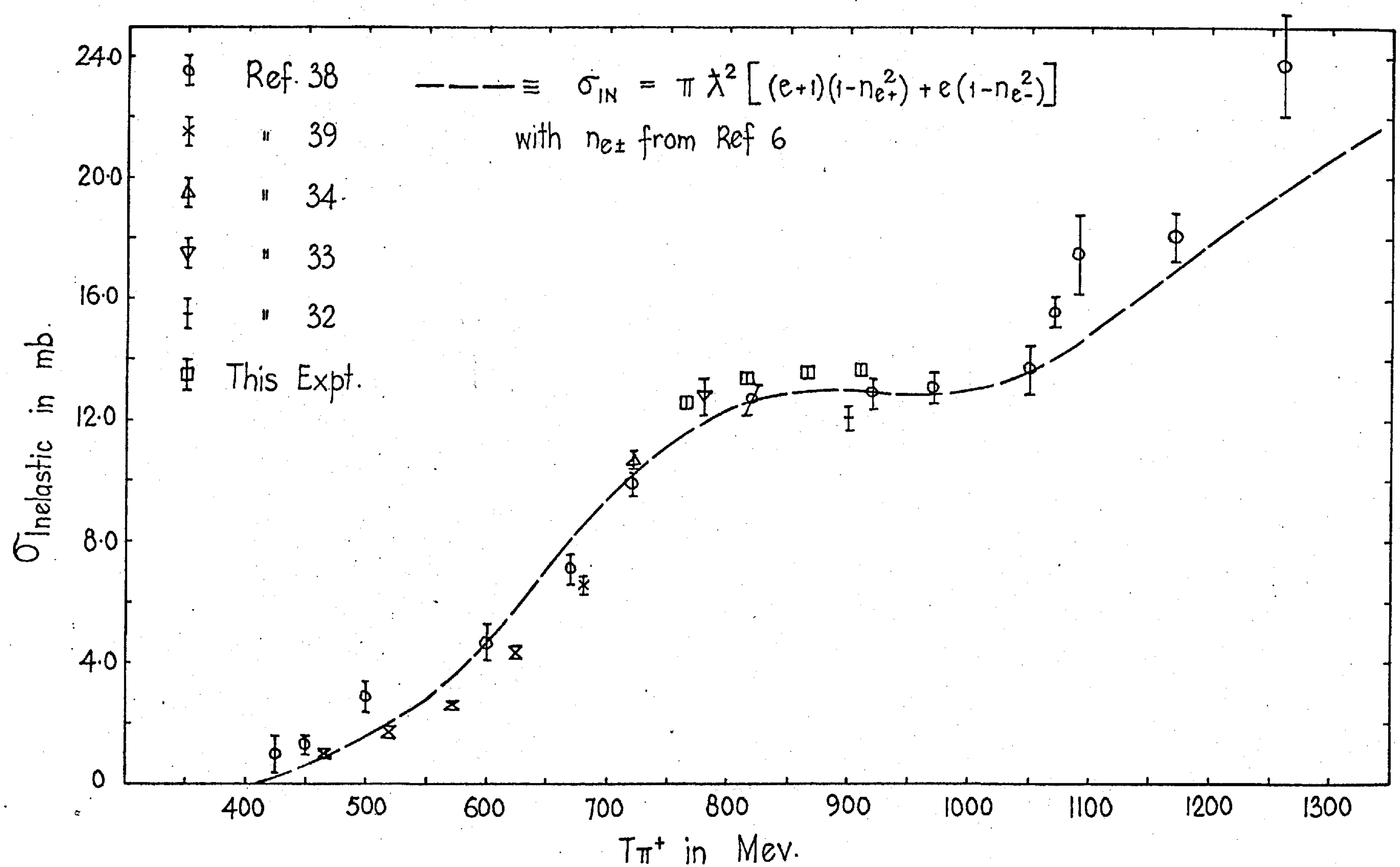

Ref. 38
" 39
" 34
" 33
" 32
This Expt.
$\equiv \sigma_{IN} = \pi \lambda\!\!\!^{-2} \left[(e+1)(1-n_{e+}^2) + e(1-n_{e-}^2) \right]$
with $n_{e\pm}$ from Ref 6
$\sigma_{\text{Inelastic}}$ in mb.
T_{π^+} in Mev.
0
4·0
8·0
12·0
16·0
20·0
24·0
400
500
600
700
800
900
1000
1100
1200
1300

Fig. 4·3

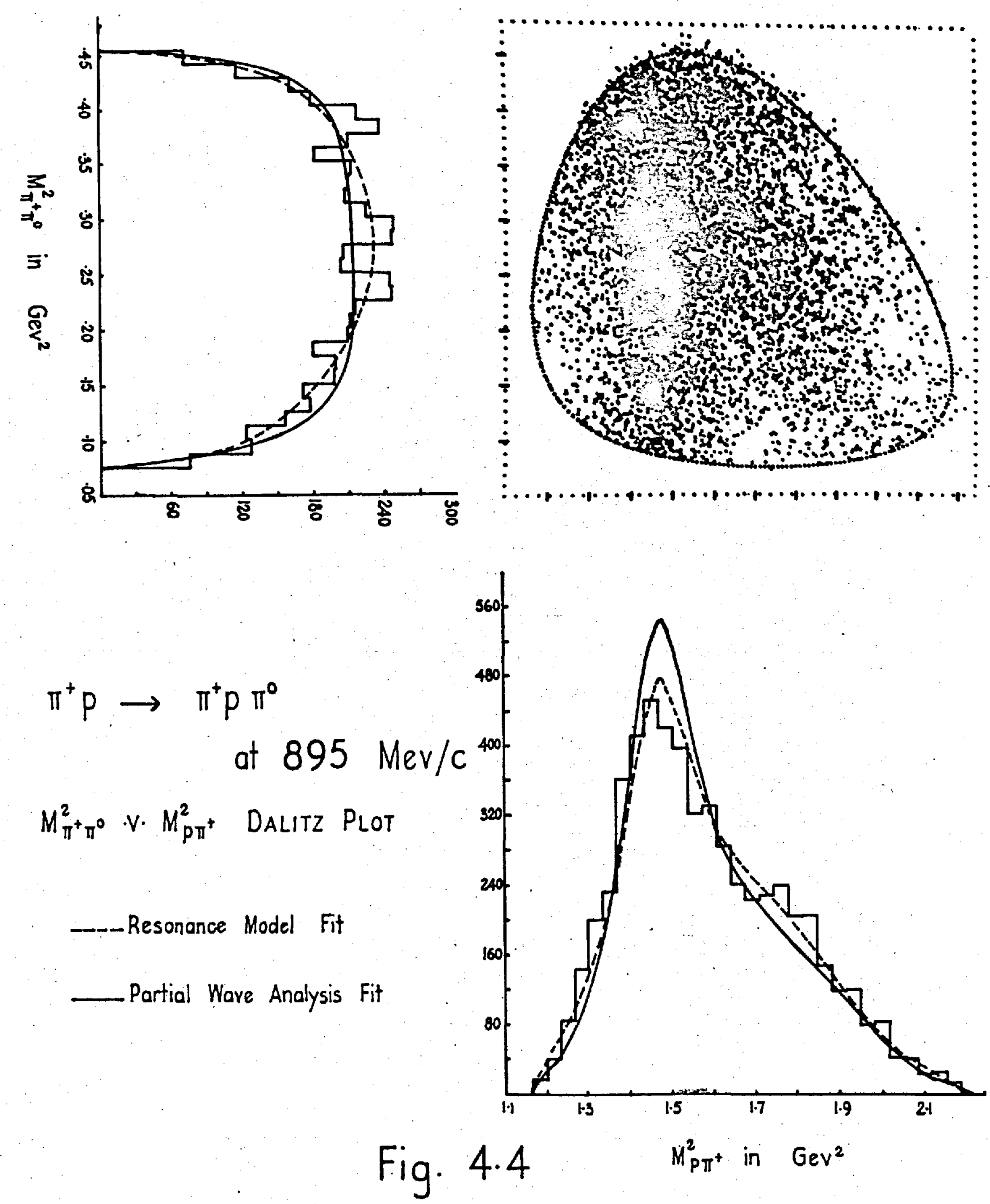

$\pi^+ p \longrightarrow \pi^+ p \pi^0$
at 895 Mev/c
$M^2_{\pi^+\pi^0}$ ·V· $M^2_{p\pi^+}$ DALITZ PLOT
----Resonance Model Fit
——Partial Wave Analysis Fit
$M^2_{\pi^+\pi^0}$ in Gev^2
·05 ·10 ·15 ·20 ·25 ·30 ·35 ·40 ·45
60 120 180 240 300
80 160 240 320 400 480 560
1·1 1·3 1·5 1·7 1·9 2·1
$M^2_{p\pi^+}$ in Gev^2

Fig. 4.4

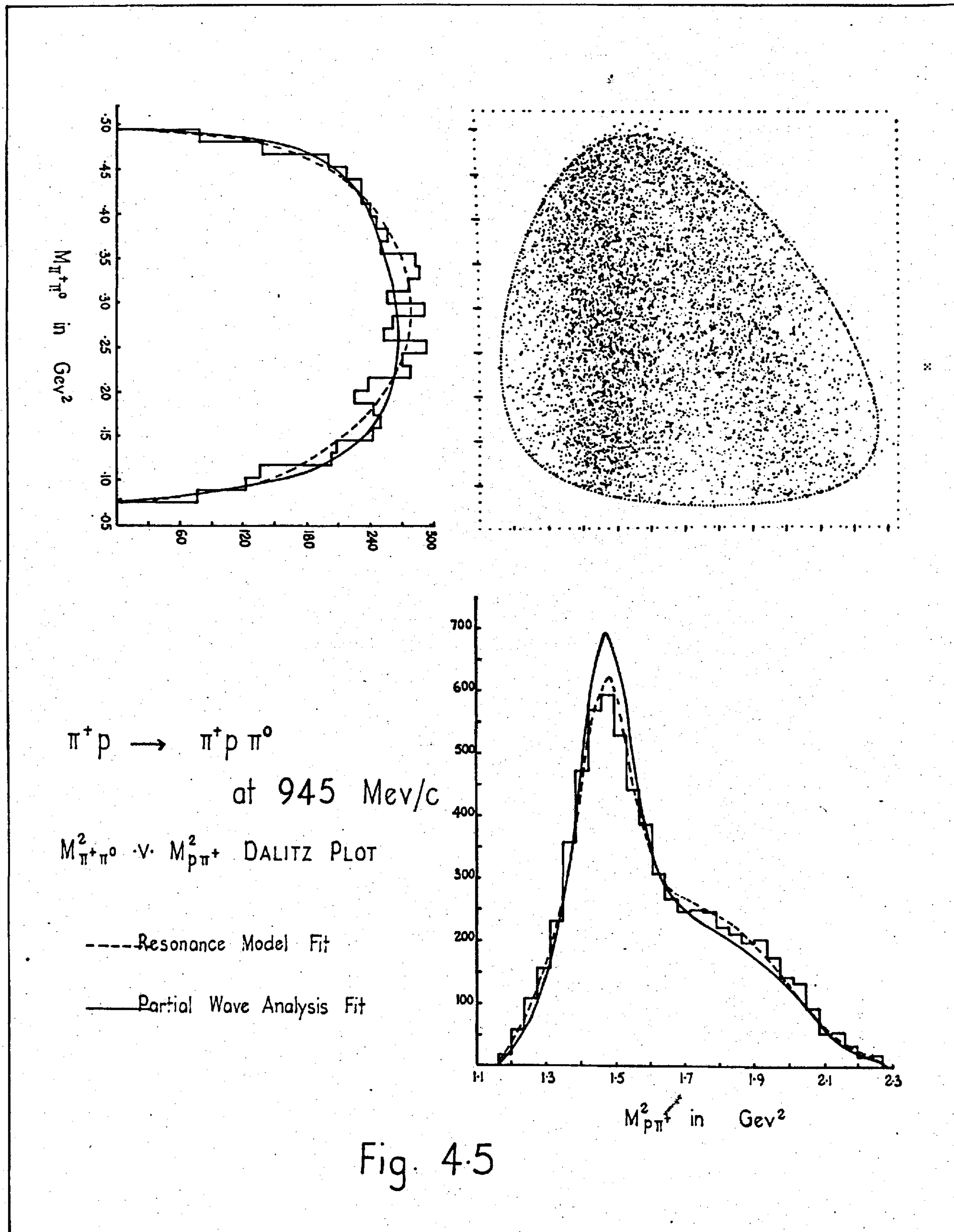

$M^2_{\pi^+\pi^0}$ in Gev²
·50
·45
·40
·35
·30
·25
·20
·15
·10
·05
60
120
180
240
300
$\pi^+ p \longrightarrow \pi^+ p \pi^0$
at 945 Mev/c
$M^2_{\pi^+\pi^0}$ ·V· $M^2_{p\pi^+}$ DALITZ PLOT
----Resonance Model Fit
——Partial Wave Analysis Fit
700
600
500
400
300
200
100
1·1
1·3
1·5
1·7
1·9
2·1
2·3
$M^2_{p\pi^+}$ in Gev²

Fig. 4·5

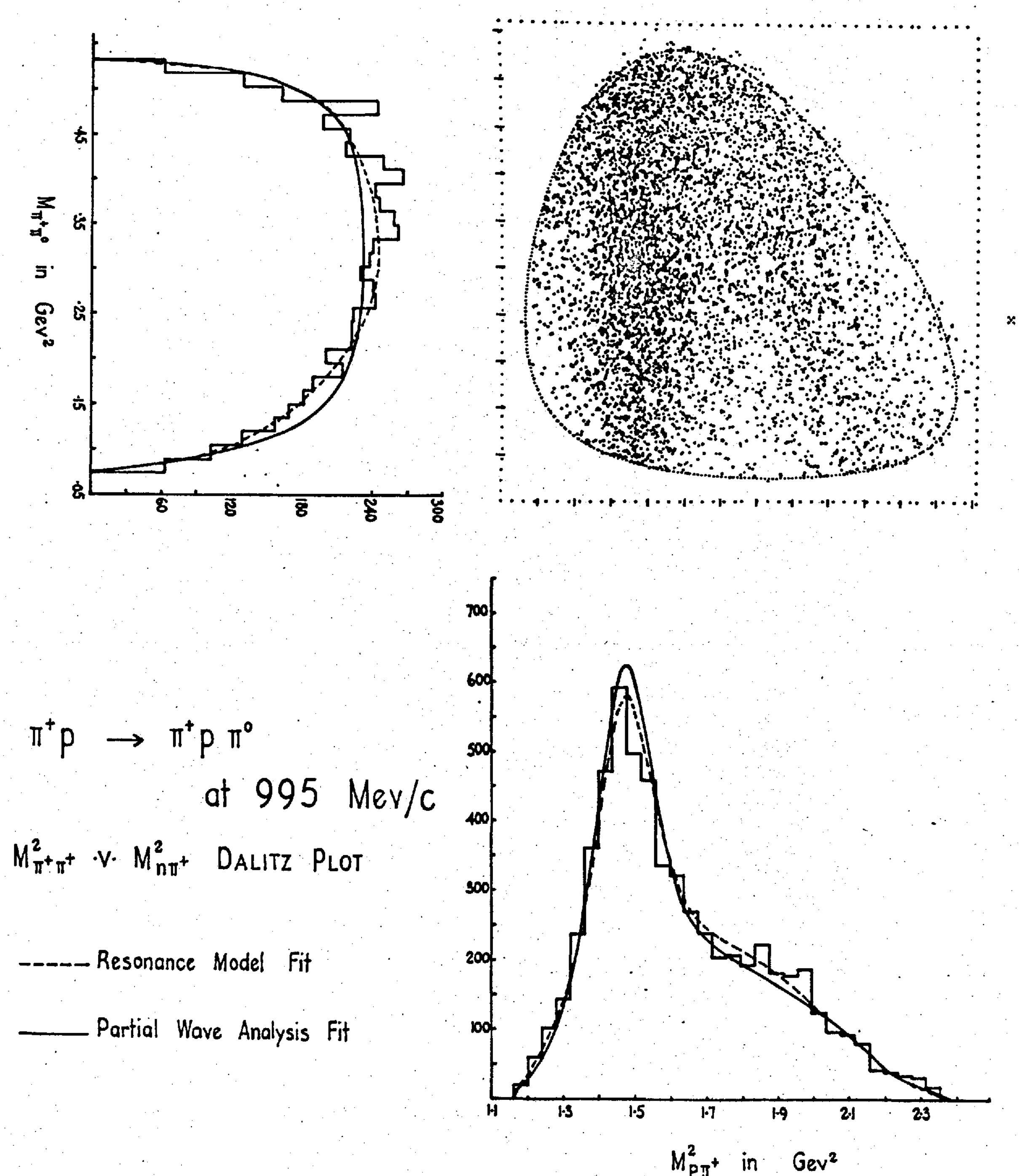

M π+π° in Gev²
·05
·15
·25
·35
·45
60
120
180
240
300
π⁺p → π⁺p π°
at 995 Mev/c
M²π⁺π⁺ ·V· M²nπ⁺ DALITZ PLOT
----- Resonance Model Fit
—— Partial Wave Analysis Fit
700
600
500
400
300
200
100
1·1
1·3
1·5
1·7
1·9
2·1
2·3
M²pπ⁺ in Gev²

Fig. 4·6

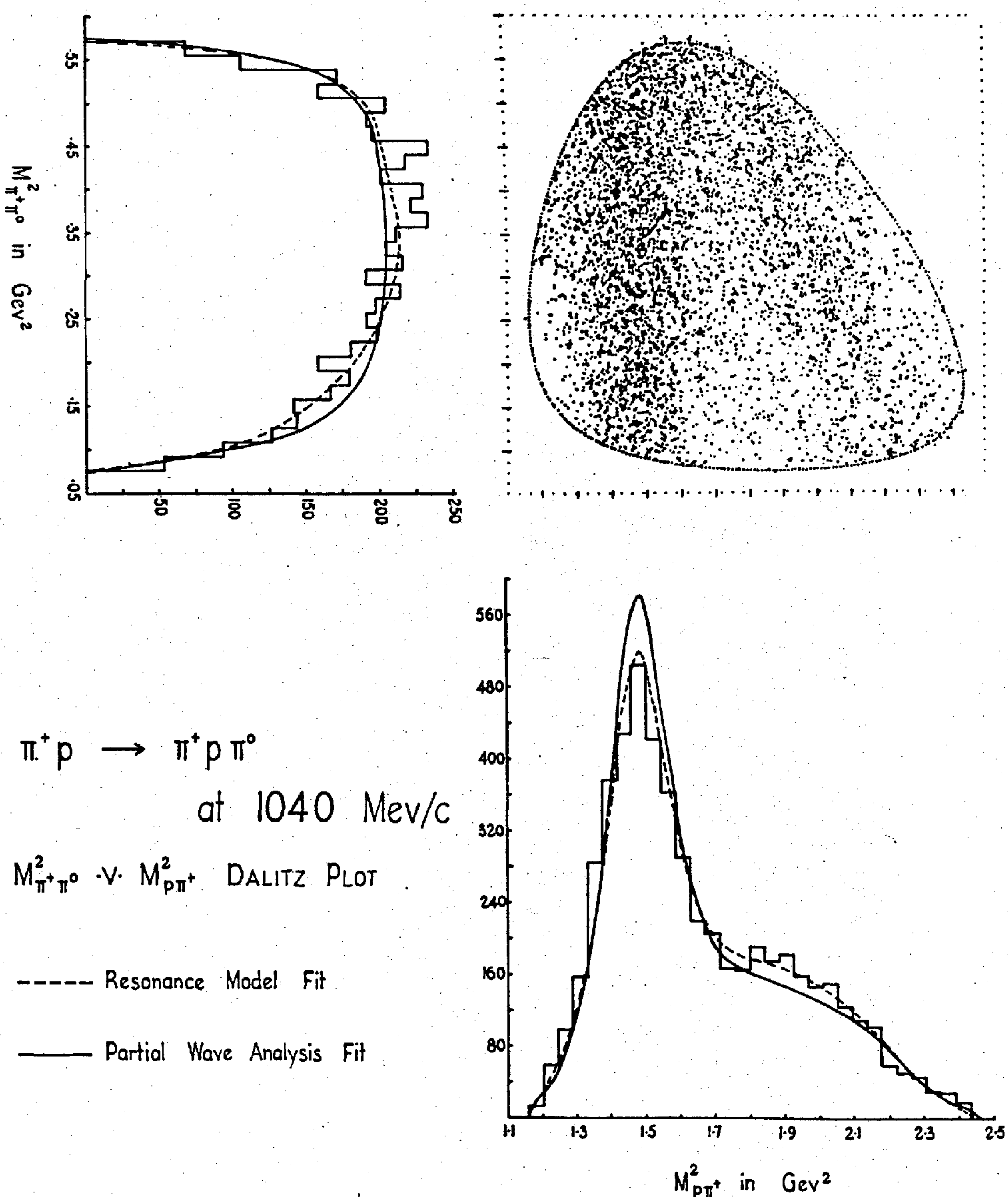

$M^2_{\pi^+\pi^0}$ in Gev²
·55
·45
·35
·25
·15
·05
50
100
150
200
250
$\pi^+ p \longrightarrow \pi^+ p \pi^0$
at 1040 Mev/c
$M^2_{\pi^+\pi^0}$ ·V· $M^2_{p\pi^+}$ DALITZ PLOT
----- Resonance Model Fit
——— Partial Wave Analysis Fit
560
480
400
320
240
160
80
1·1
1·3
1·5
1·7
1·9
2·1
2·3
2·5
$M^2_{p\pi^+}$ in Gev²

Fig. 4·7

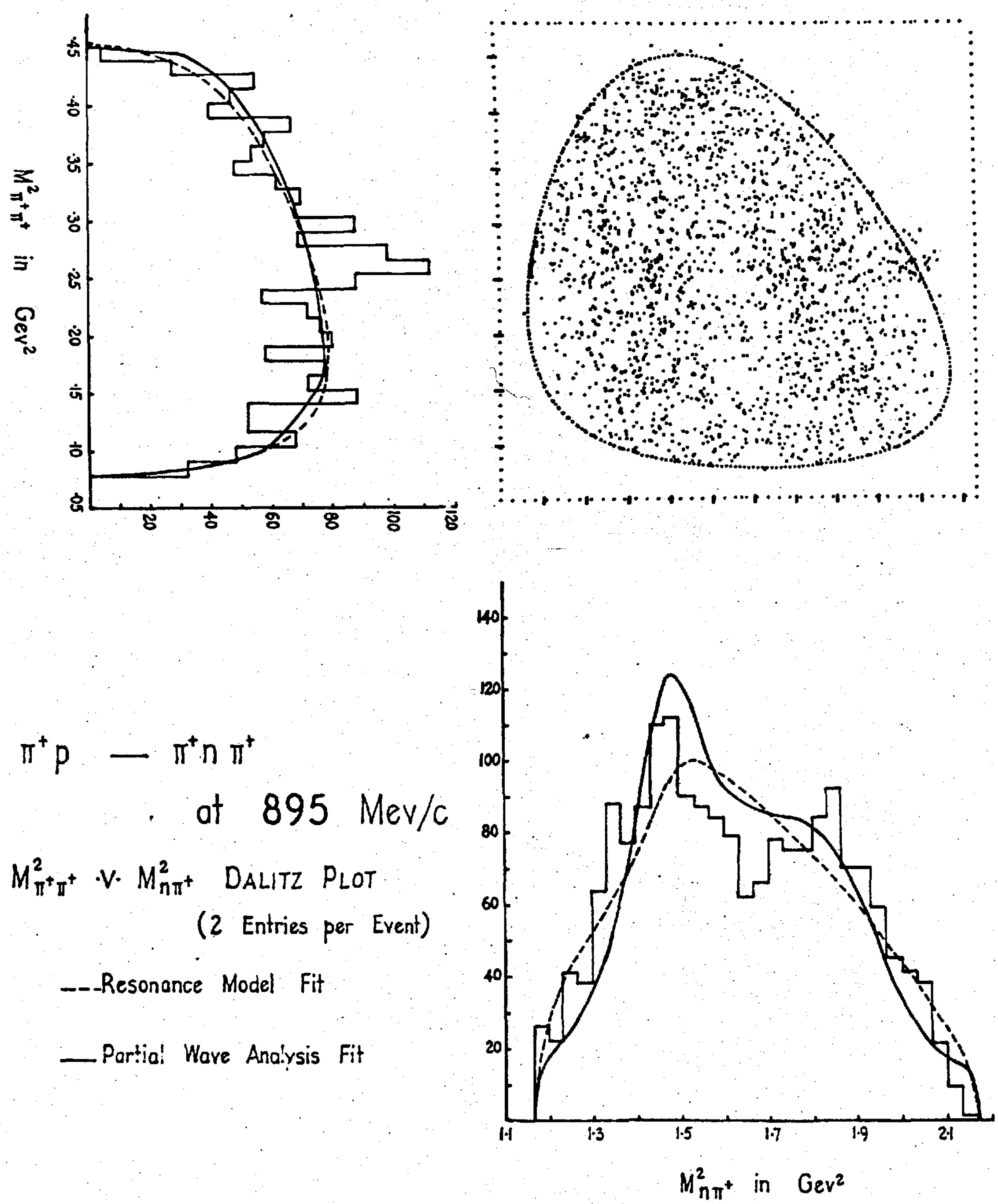

$\pi^+ p \longrightarrow \pi^+ n \pi^+$ at 895 Mev/c

$M^2_{\pi^+\pi^+}$ ·V· $M^2_{n\pi^+}$ DALITZ PLOT

(2 Entries per Event)

--- Resonance Model Fit

—— Partial Wave Analysis Fit

Fig. 4·8

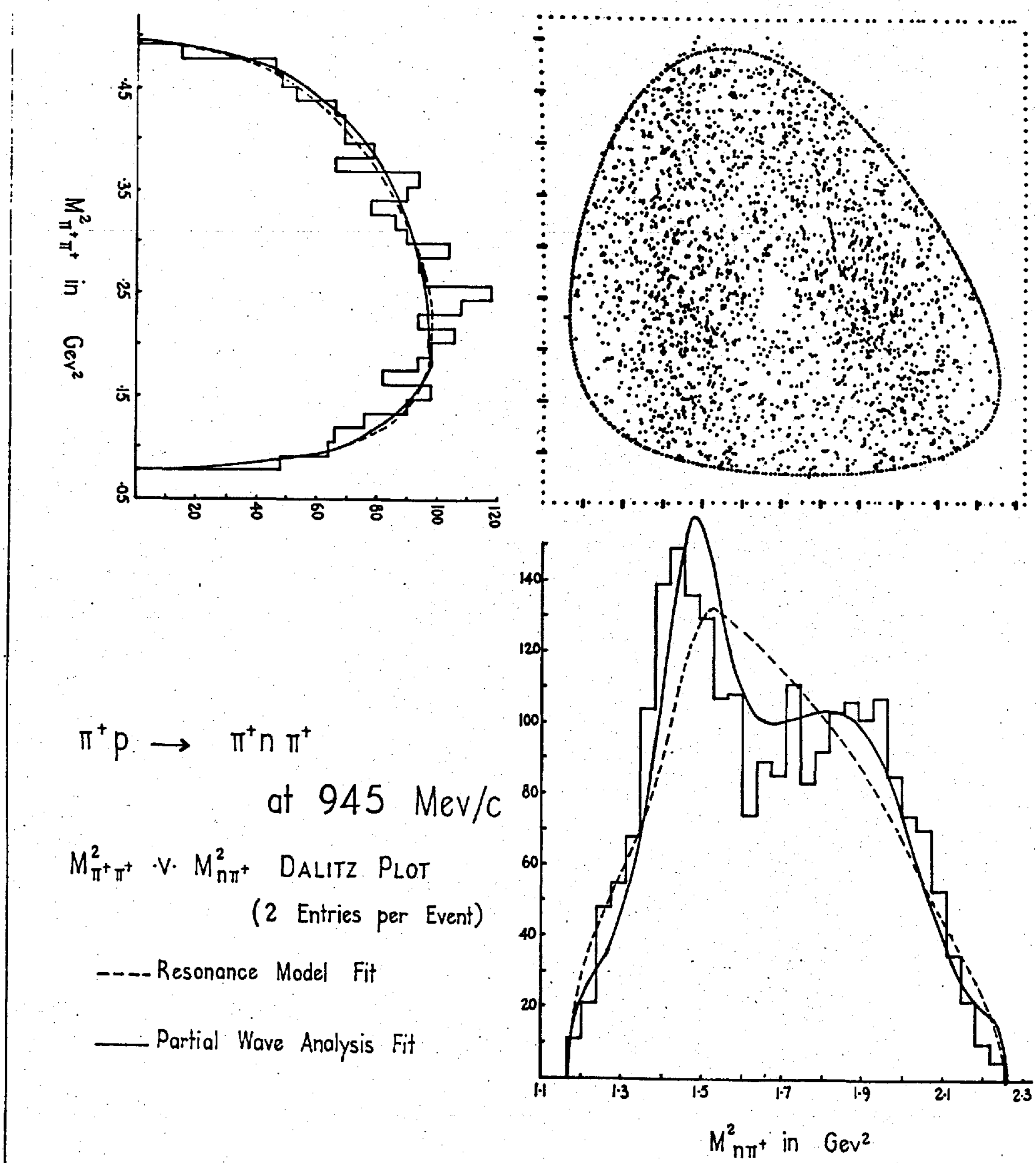

$M^2_{\pi^+\pi^+}$ in Gev^2
·45
·35
·25
·15
·05
20
40
60
80
100
120
140
120
100
80
60
40
20
1·1
1·3
1·5
1·7
1·9
2·1
2·3
$M^2_{n\pi^+}$ in Gev^2
$\pi^+ p \rightarrow \pi^+ n \pi^+$
at 945 Mev/c
$M^2_{\pi^+\pi^+}$ ·V· $M^2_{n\pi^+}$ DALITZ PLOT
(2 Entries per Event)
---- Resonance Model Fit
—— Partial Wave Analysis Fit

Fig 4·9

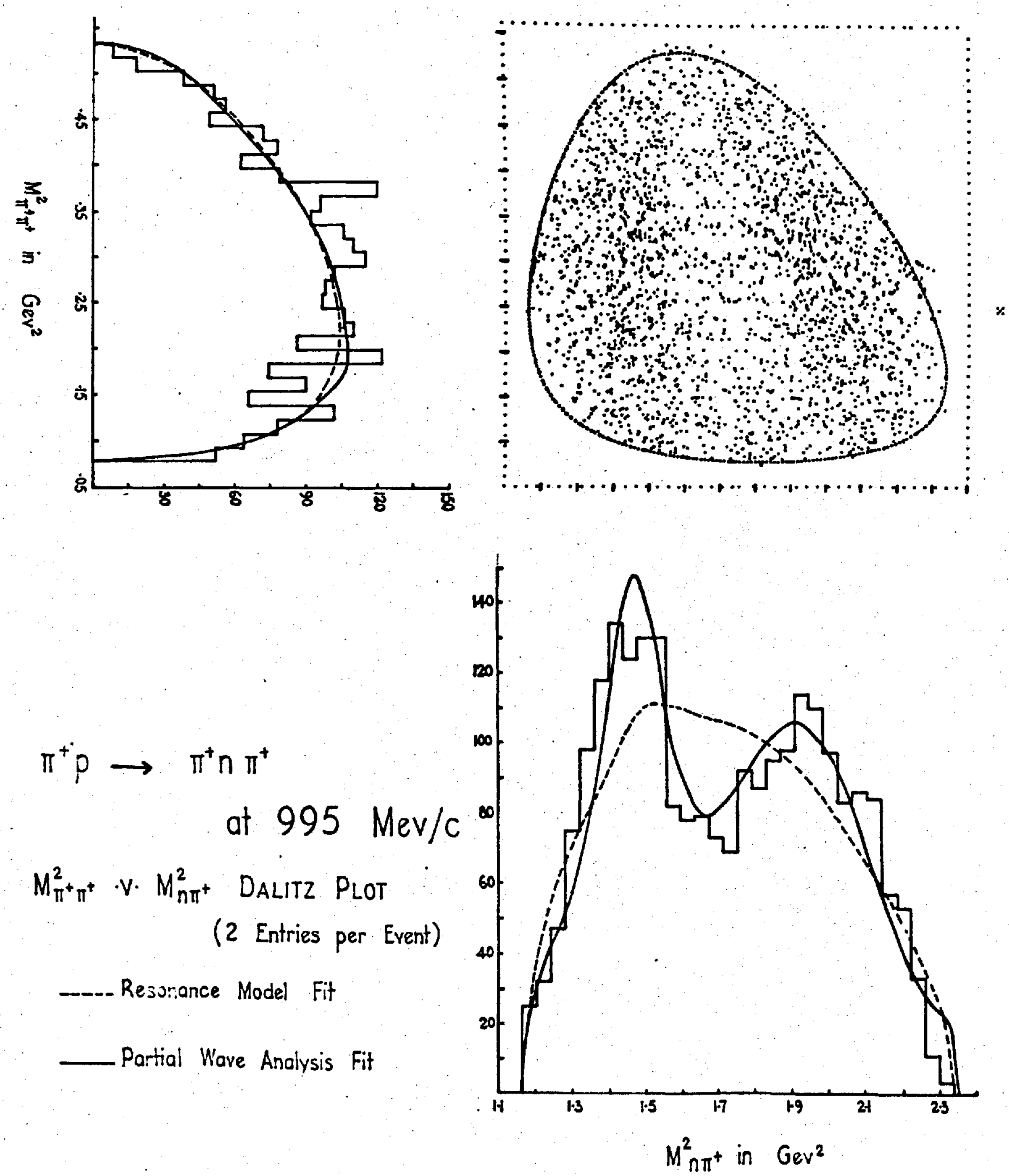

$M^2_{\pi^+\pi^+}$ in Gev²
·05
·15
·25
·35
·45
30
60
90
120
150
140
120
100
80
60
40
20
1·1
1·3
1·5
1·7
1·9
2·1
2·3
$M^2_{n\pi^+}$ in Gev²
$\pi^+ p \rightarrow \pi^+ n \pi^+$
at 995 Mev/c
$M^2_{\pi^+\pi^+}$ ·V· $M^2_{n\pi^+}$ DALITZ PLOT
(2 Entries per Event)
----- Resonance Model Fit
——— Partial Wave Analysis Fit

Fig 4·10

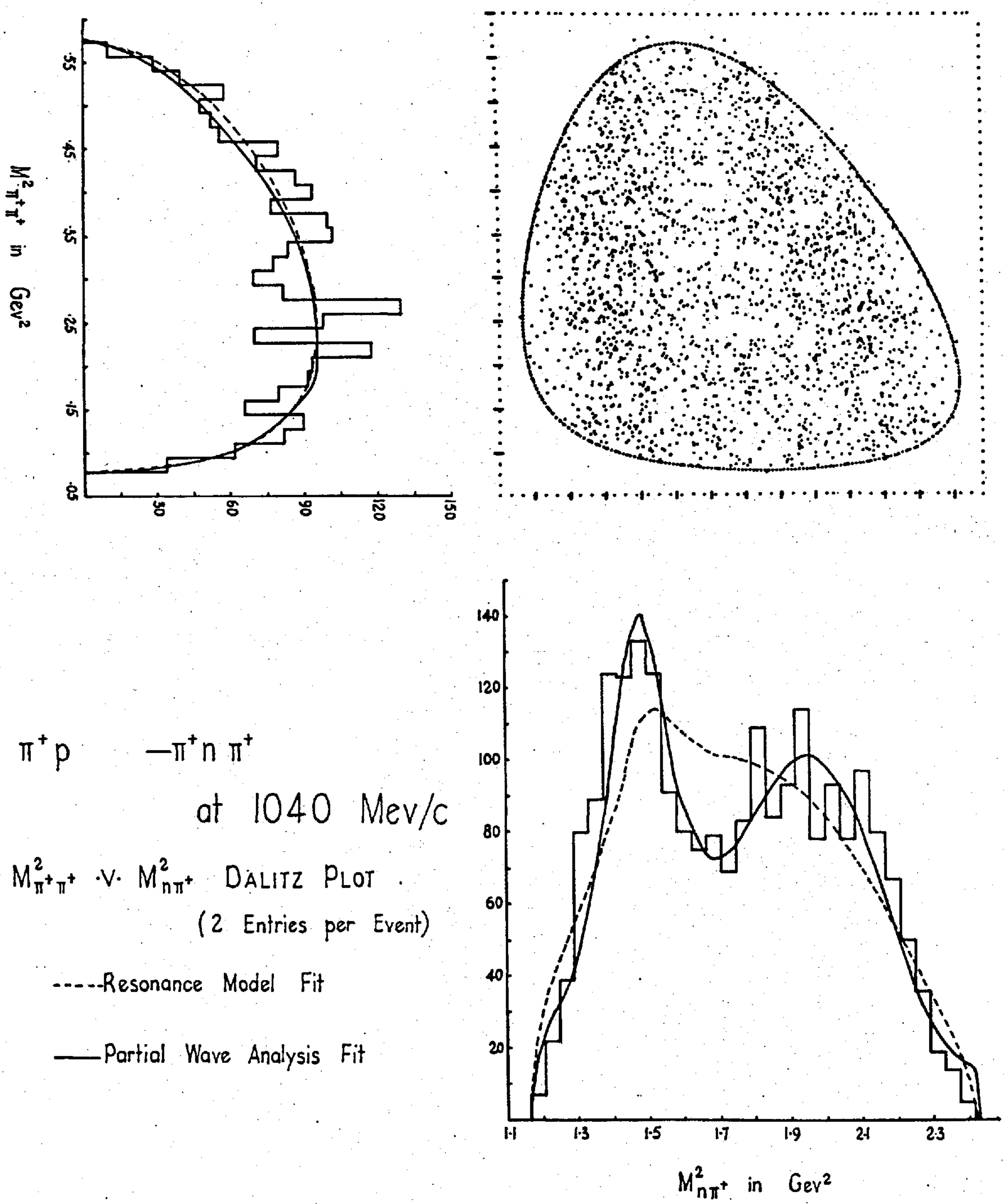

$\pi^+ p \rightarrow \pi^+ n \pi^+$
at 1040 Mev/c
$M^2_{\pi^+\pi^+}$ ·V· $M^2_{n\pi^+}$ DALITZ PLOT.
(2 Entries per Event)
-----Resonance Model Fit
——Partial Wave Analysis Fit
$M^2_{\pi^+\pi^+}$ in Gev²
·05 ·15 ·25 ·35 ·45 ·55
30 60 90 120 150
140 120 100 80 60 40 20
1·1 1·3 1·5 1·7 1·9 2·1 2·3
$M^2_{n\pi^+}$ in Gev²

Fig. 4·11

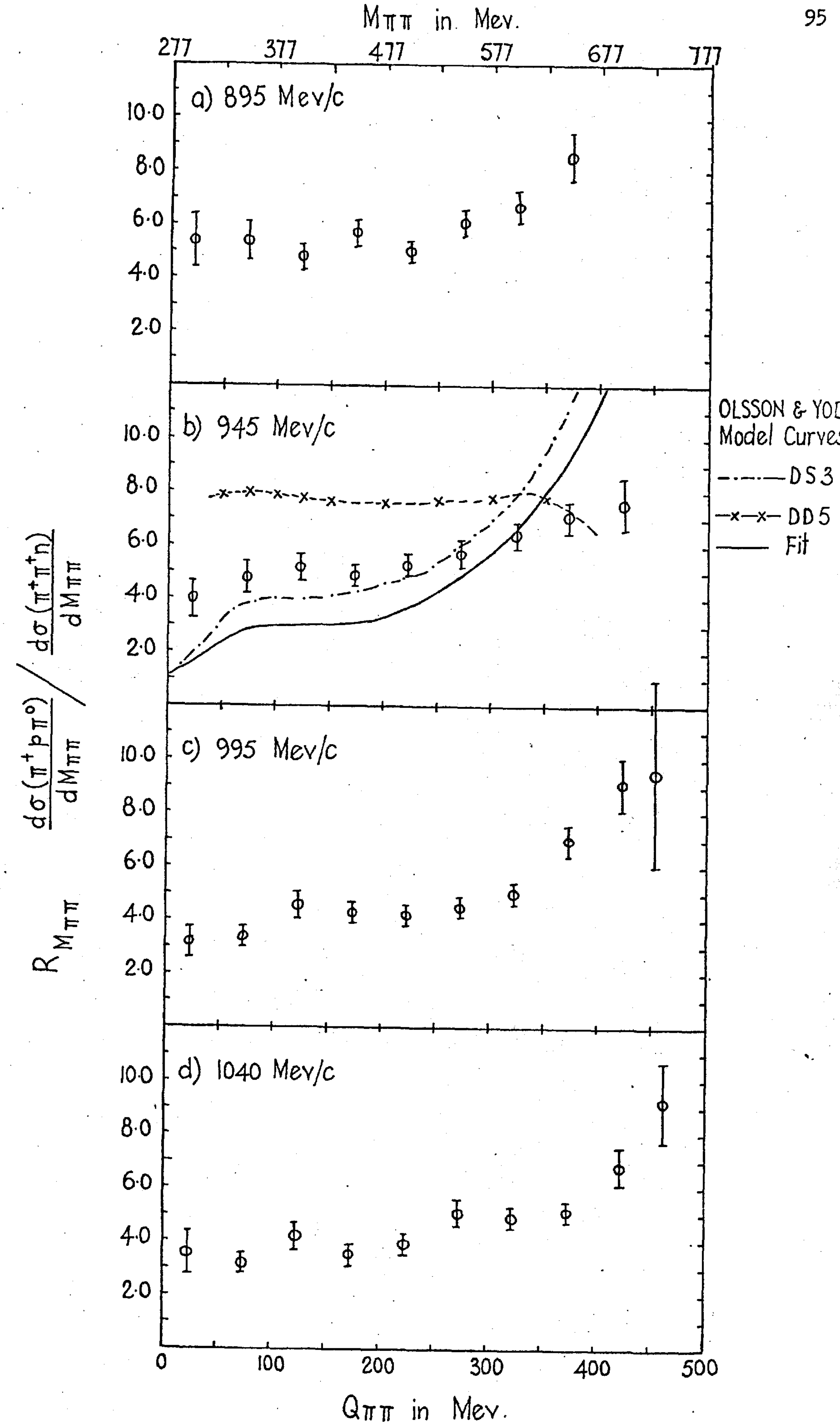

Mππ in. Mev.
277
377
477
577
677
777
a) 895 Mev/c
b) 945 Mev/c
c) 995 Mev/c
d) 1040 Mev/c
10·0
8·0
6·0
4·0
2·0
OLSSON & YOD Model Curves
DS3
DD5
Fit
R Mππ
dσ(π+pπ0)/dMππ / dσ(π+π+n)/dMππ
0
100
200
300
400
500
Qππ in Mev.

Fig. 4·12

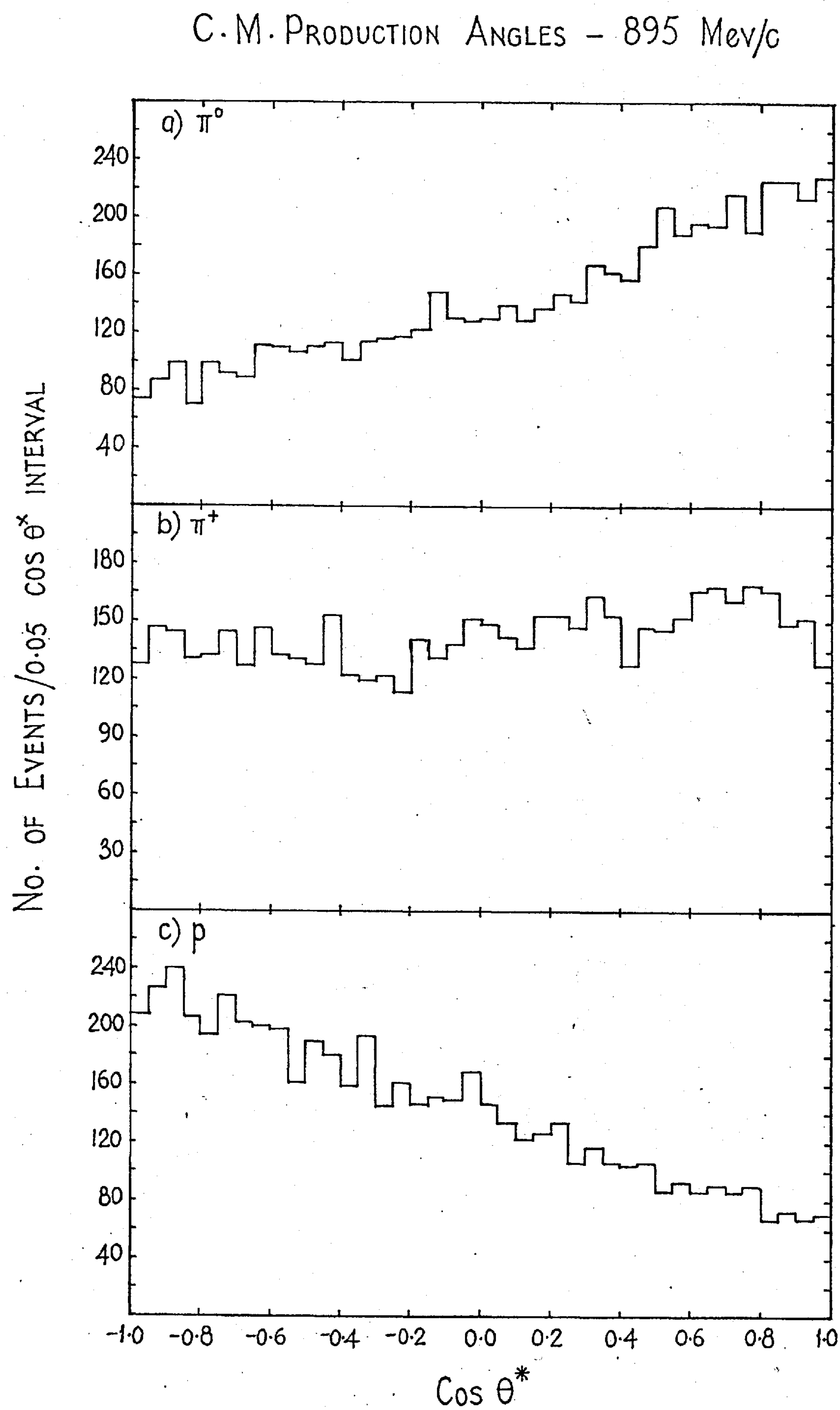
C. M. PRODUCTION ANGLES – 895 Mev/c
a) π^0
b) π^+
c) p
No. OF EVENTS/0·05 COS θ^* INTERVAL
240
200
160
120
80
40
180
150
120
90
60
30
-1·0
-0·8
-0·6
-0·4
-0·2
0·0
0·2
0·4
0·6
0·8
1·0
Cos θ^*

Fig. 4·13

C.M. PRODUCTION ANGLES - 945 Mev/c

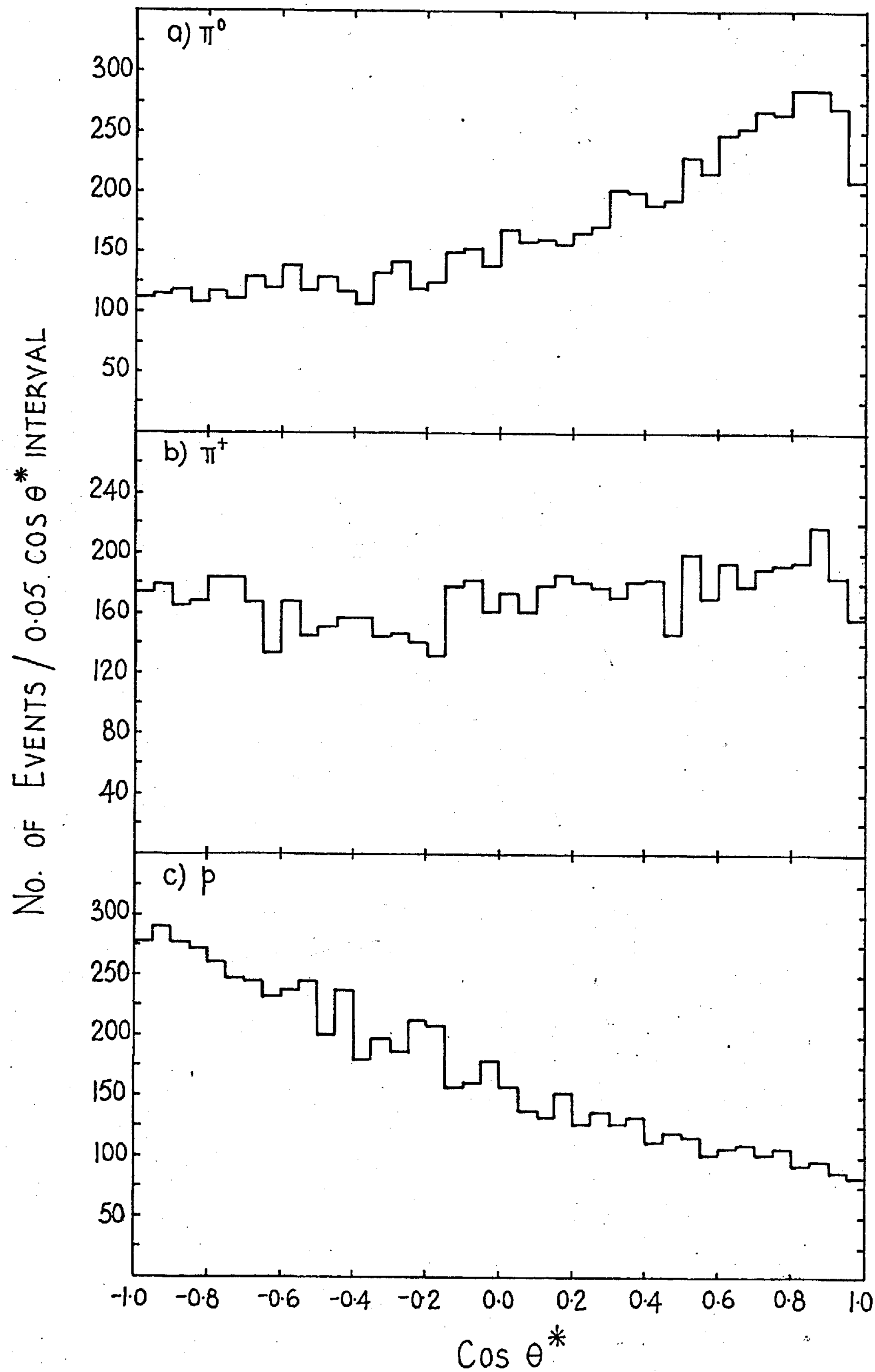

Fig. 4·14

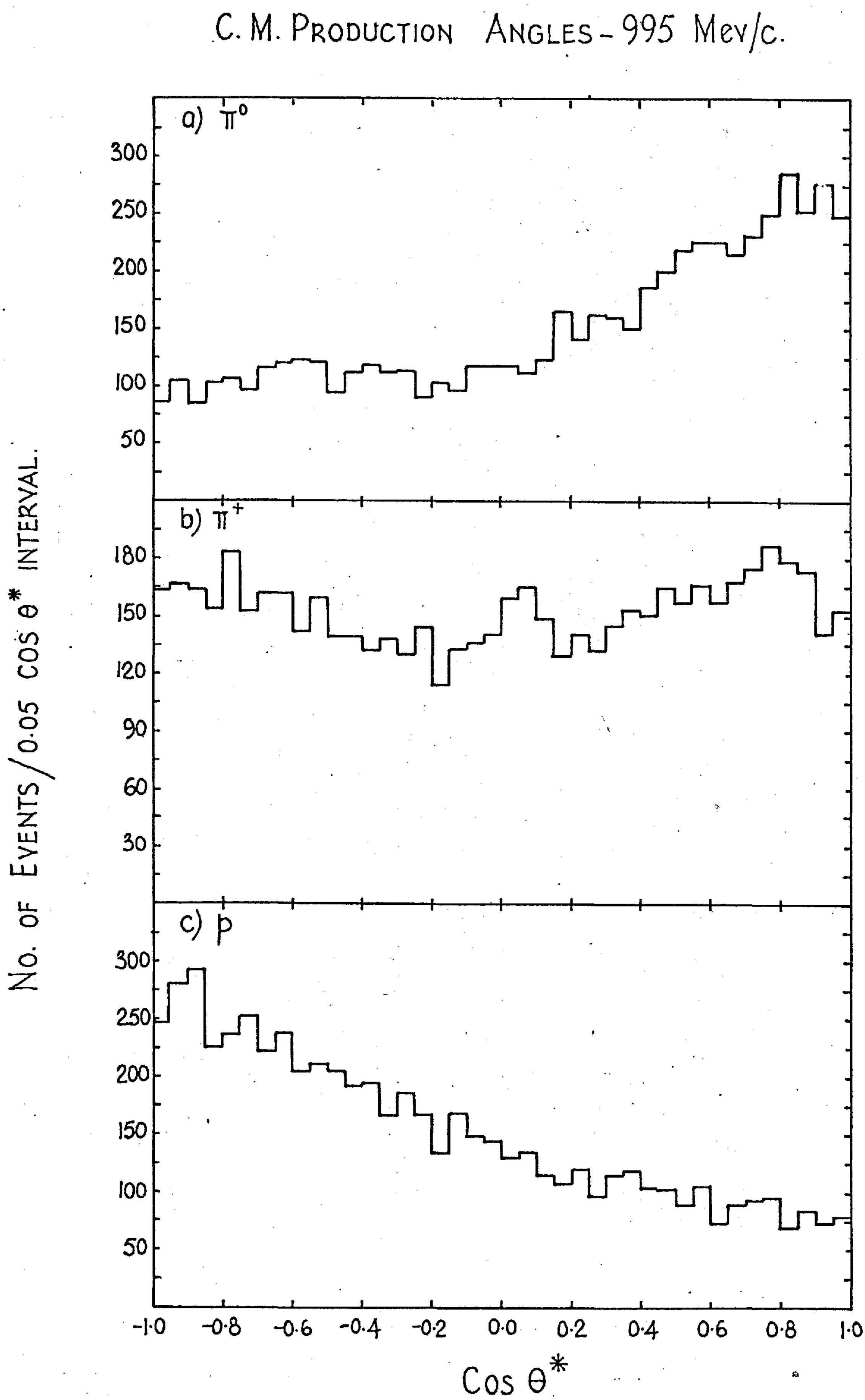
C. M. Production Angles - 995 Mev/c.
No. of Events/0.05 cos θ* interval.
a) π°
300
250
200
150
100
50
b) π⁺
180
150
120
90
60
30
c) p
300
250
200
150
100
50
-1·0
-0·8
-0·6
-0·4
-0·2
0·0
0·2
0·4
0·6
0·8
1·0
Cos θ*

Fig. 4·15

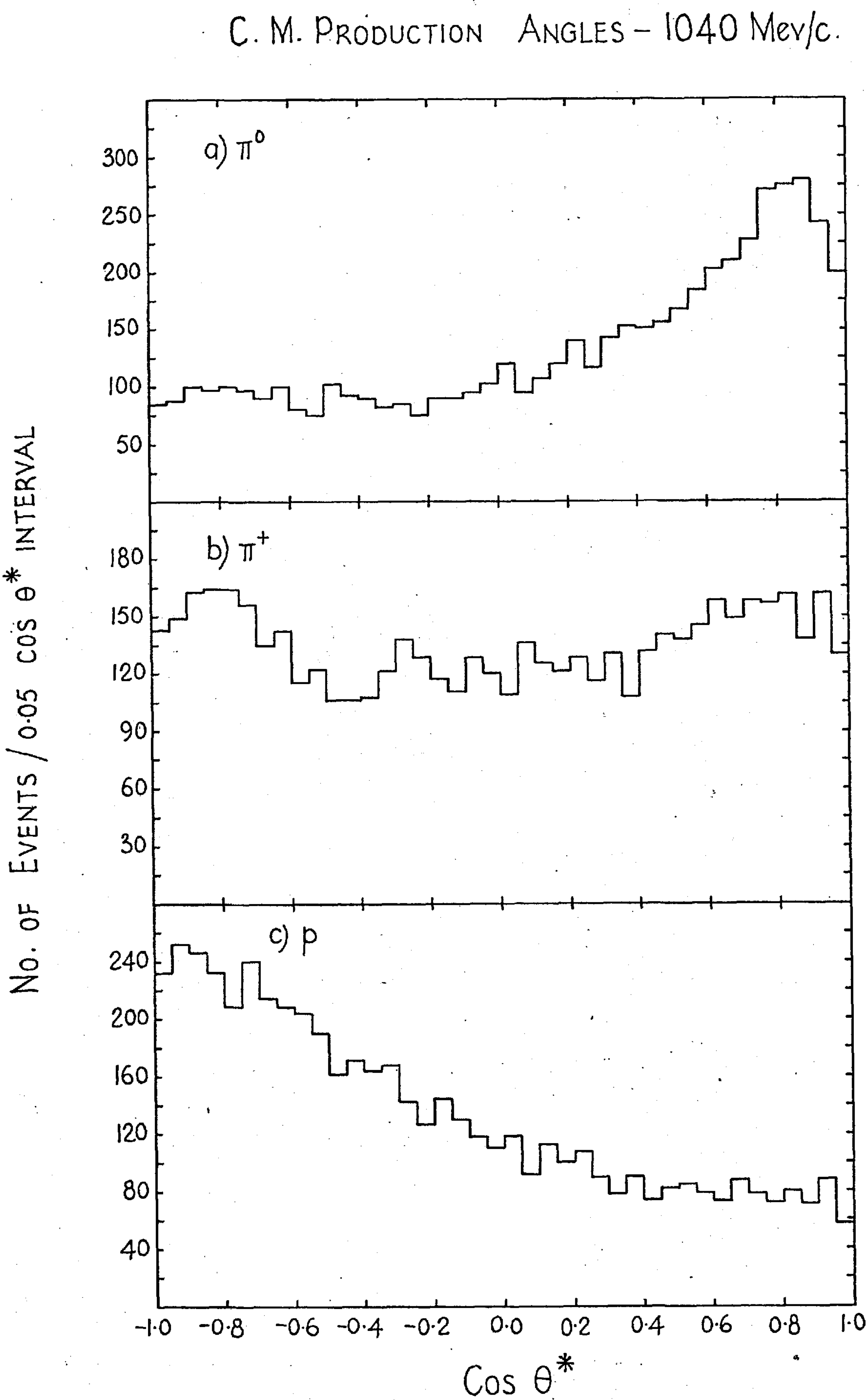
C. M. PRODUCTION ANGLES – 1040 Mev/c.
a) π^0
300
250
200
150
100
50
b) π^+
180
150
120
90
60
30
c) p
240
200
160
120
80
40
-1·0 -0·8 -0·6 -0·4 -0·2 0·0 0·2 0·4 0·6 0·8 1·0
No. OF EVENTS / 0·05 COS θ* INTERVAL
Cos θ*

Fig. 4·16

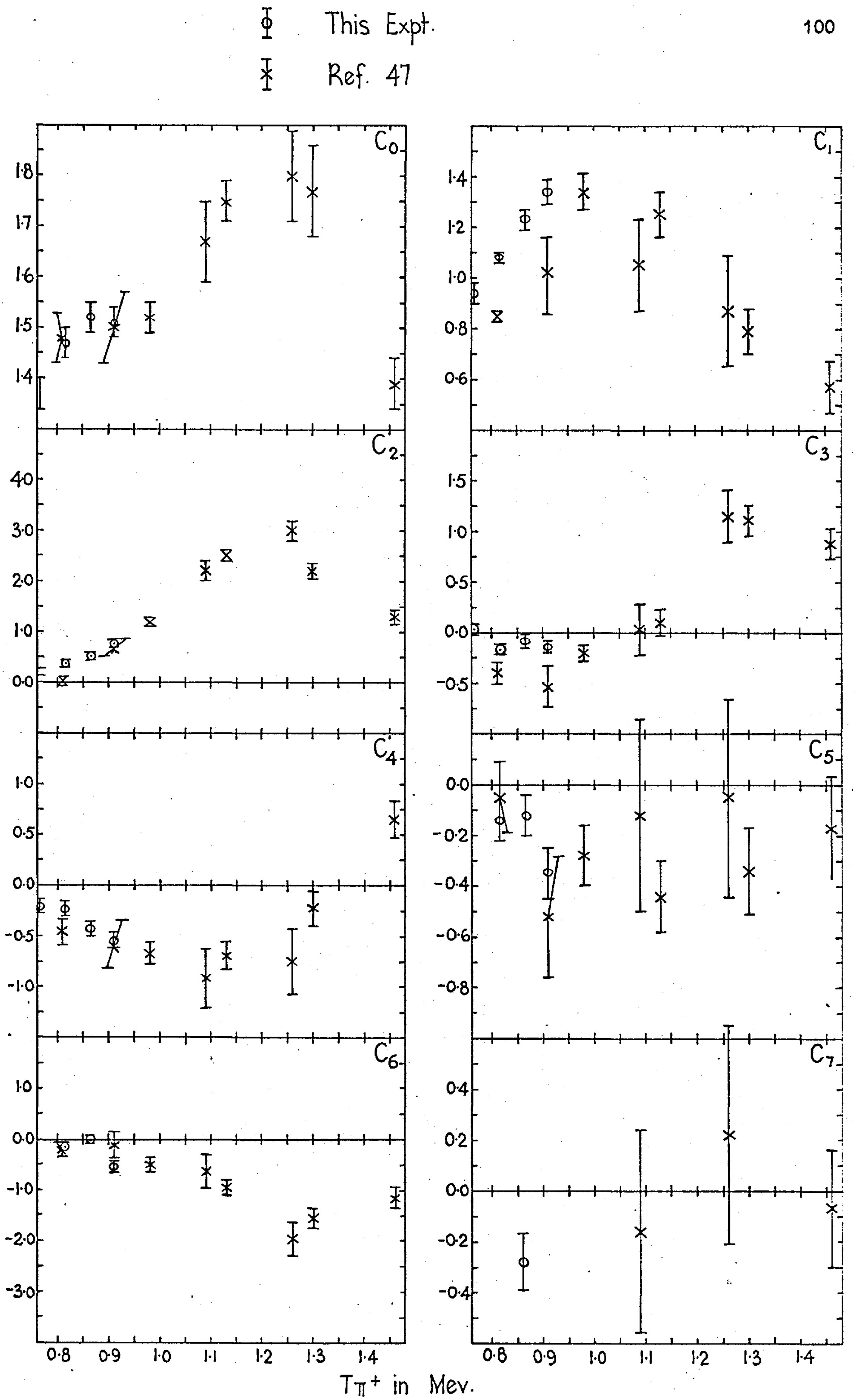

This Expt.
Ref. 47
C0
C1
C2
C3
C4
C5
C6
C7
1·8
1·7
1·6
1·5
1·4
1·4
1·2
1·0
0·8
0·6
4·0
3·0
2·0
1·0
0·0
1·5
1·0
0·5
0·0
-0·5
1·0
0·5
0·0
-0·5
-1·0
0·0
-0·2
-0·4
-0·6
-0·8
1·0
0·0
-1·0
-2·0
-3·0
0·4
0·2
0·0
-0·2
-0·4
0·8
0·9
1·0
1·1
1·2
1·3
1·4
Tπ+ in Mev.

Fig. 4·17

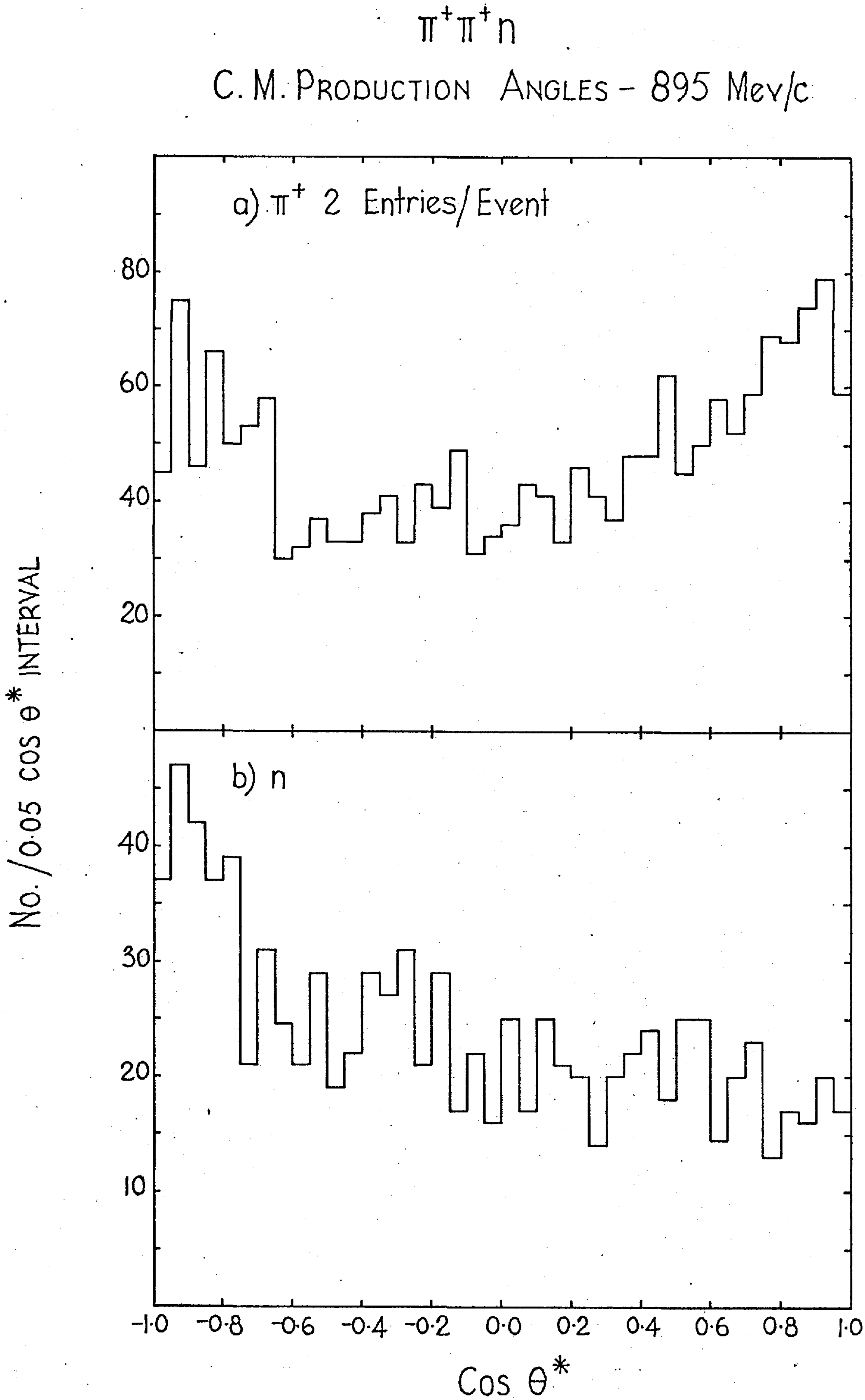

$\pi^+\pi^+n$
C.M. PRODUCTION ANGLES - 895 MeV/c
a) π^+ 2 Entries/Event
b) n
No./0.05 cos θ* INTERVAL
80
60
40
20
40
30
20
10
-1.0
-0.8
-0.6
-0.4
-0.2
0.0
0.2
0.4
0.6
0.8
1.0
Cos θ*

Fig. 4.18

$\pi^+\pi^+ n$

C.M. PRODUCTION ANGLES - 945 Mev/c

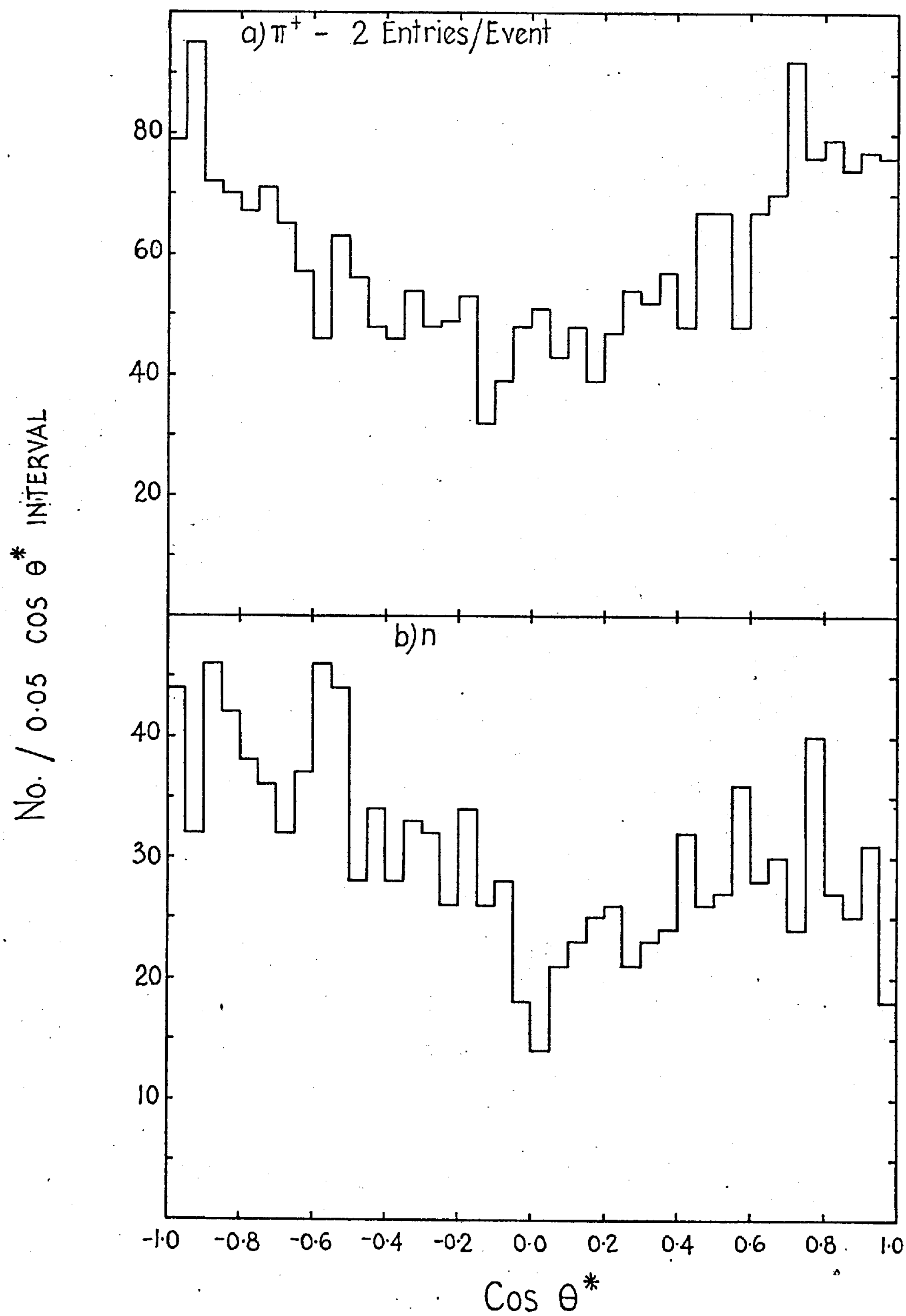

Fig. 4·19

$\pi^+\pi^+ n$

C.M. PRODUCTION ANGLES - 995 Mev/c.

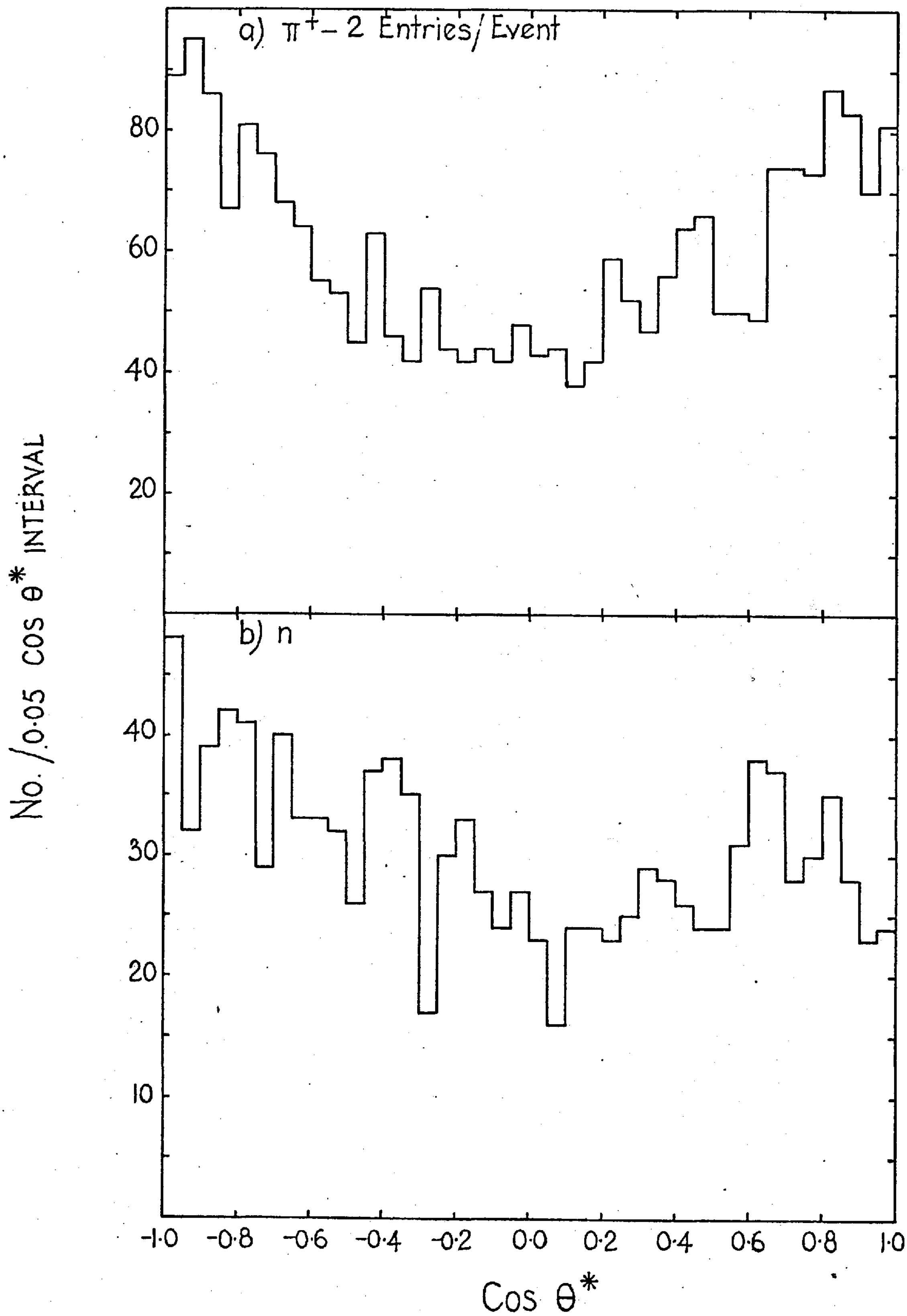

Fig. 4.20

$\pi^+\pi^+n$

C.M. PRODUCTION ANGLES - 1040 Mev/c

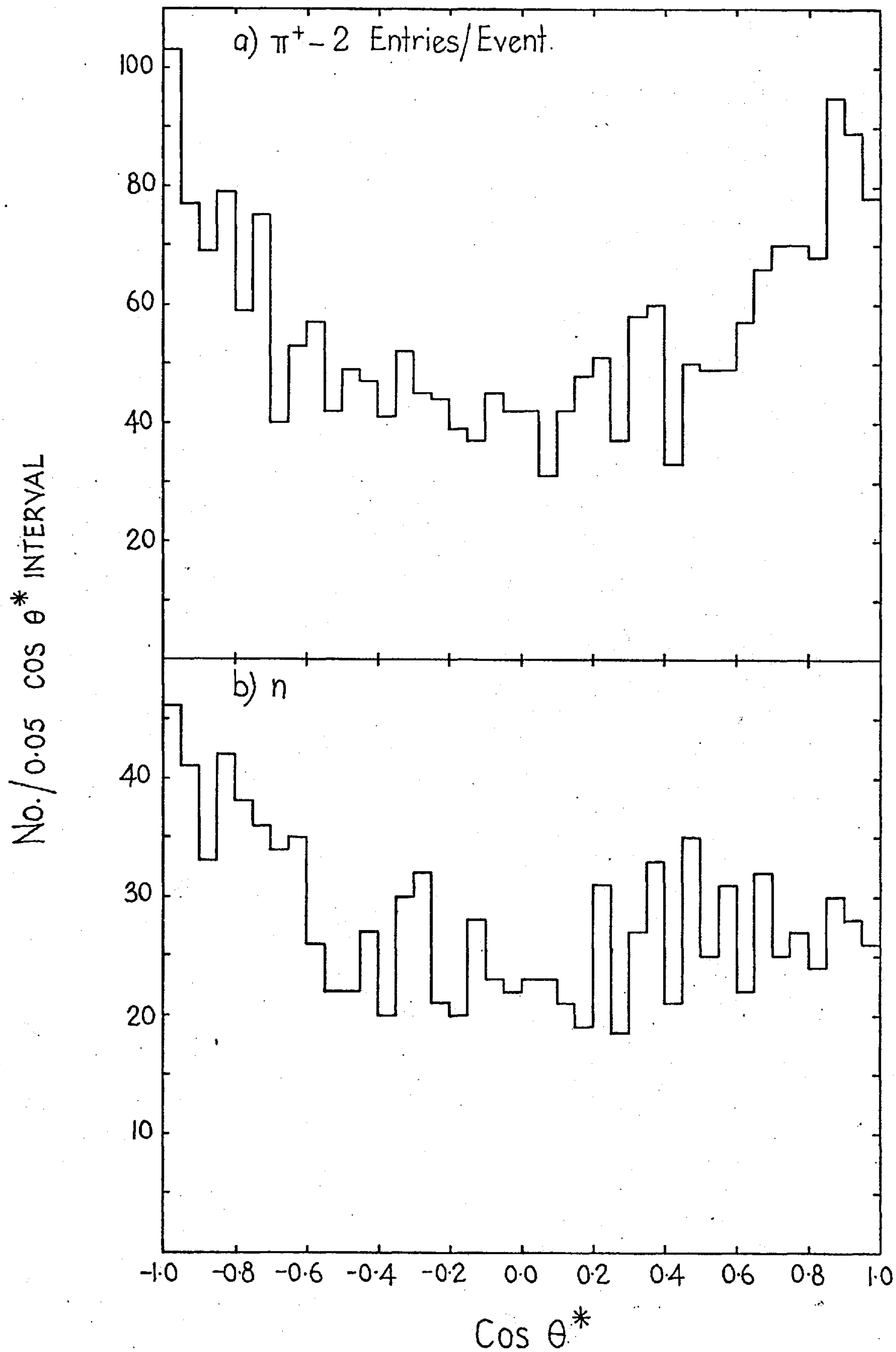

Fig. 4.21

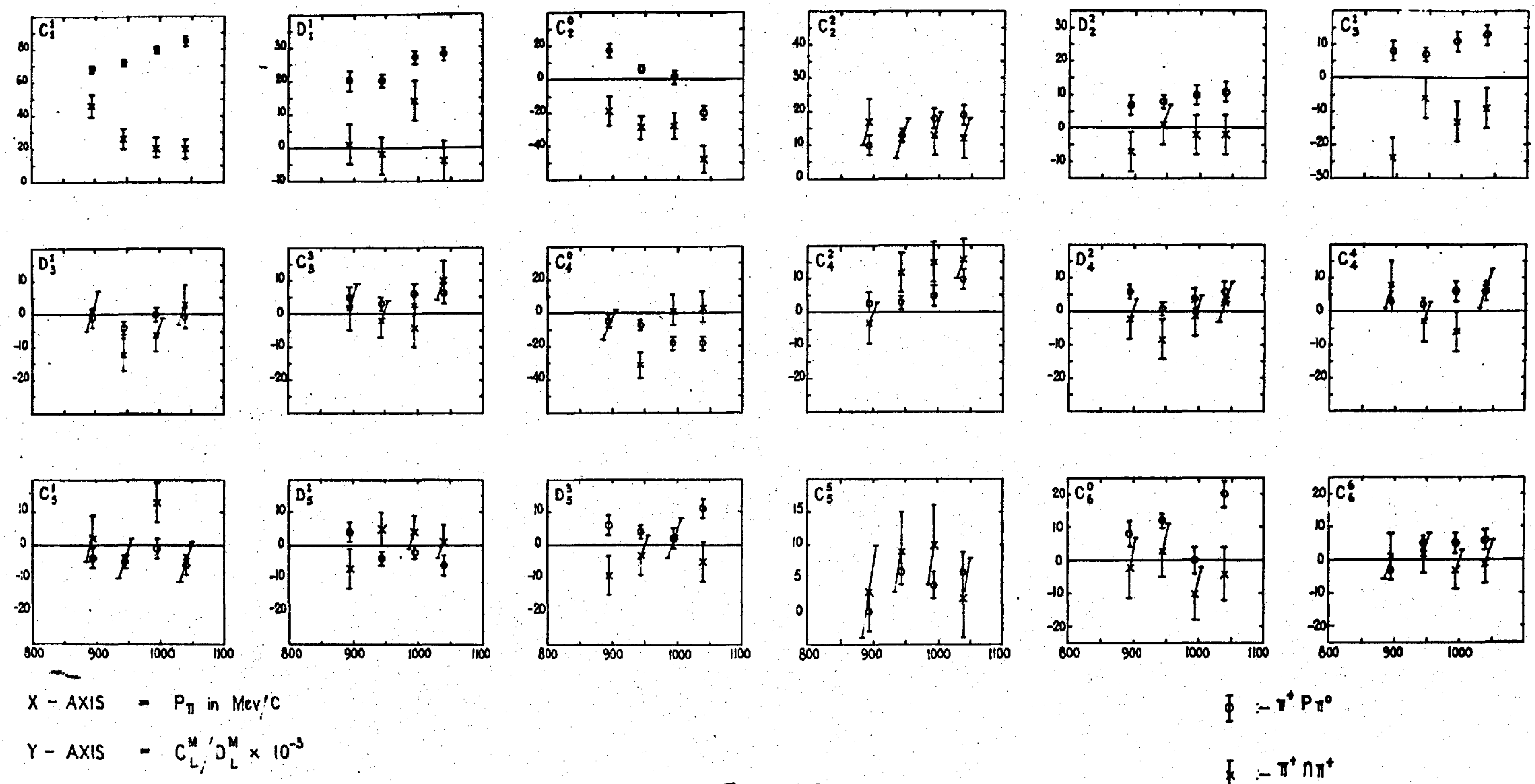

C_1^1
D_1^1
C_2^0
C_2^2
D_2^2
C_3^1
D_3^1
C_3^3
C_4^0
C_4^2
D_4^2
C_4^4
C_5^1
D_5^1
D_5^3
C_5^5
C_6^0
C_6^6
X - AXIS = P_π in Mev/C
Y - AXIS = $C_L^M / D_L^M \times 10^{-3}$
$\pi^+ P \pi^0$
$\pi^+ n \pi^+$

Fig. 4.22

CHAPTER 5

Partial Wave Analysis of Single Pion Production

5.1 Introduction

The various phase shift analyses[6), 7), 8), 9)] of elastic pion-nucleon scattering suggest that the S1, P3, D3, D5 and F5 partial waves in the I = 3/2 state are inelastic around 1 GeV/c incident momentum. The S1, P3 and D3 are most strongly inelastic and are believed to be resonant around this energy (see Table 1.1). These resonances, excited in the s-channel in a formation experiment, are expected to decay more strongly to an inelastic rather than the elastic channel.

In the energy range of the present experiment the dominant inelastic channels are the two single pion production channels. Multi-pion production - cross-sections given in Tables 3.6 and 3.7 - contributes only around 5-9% to the total inelastic cross-section at these energies. As such multi-pion production is ignored in the determination of the inelasticities of the incident partial waves.

It should be possible to extract most of the information about the inelastic nature of the incident partial waves using a model based on an angular momentum decomposition of the single pion production reaction (4.1). In particular, the inelasticity parameters, $\eta_{\ell\pm}$, should be determined more accurately than from elastic scattering alone and it should be possible to deduce the nature, resonant or otherwise, of inelastic scattering in these partial waves. A comparison of the total inelastic cross-sections, as obtained from experiment and from the inelasticities determined by the CERN elastic phase shift analysis[6)], is shown in Figure 4.3.

In the last chapter the dominance of attractive two-body couplings in 3-particle final states has been demonstrated. Final states with a two-body subsystem of known spin and parity and a recoil particle therefore form a natural basis for an angular momentum decomposition of single pion production.

In Section 5.2 we discuss earlier attempts to fit the experimental features of single pion production on this basis. In Section 5.3 the formalism used to explain the results from the present experiment is presented.

The $I = 3/2$, $J^P = 3/2^+$ resonance, the Δ (1236), is the most dominant two-body subsystem. One or more of the incident partial waves are therefore assumed to be strongly coupled to the $\pi\Delta$ quasi-two-body angular momentum states. In Section 5.4 we discuss the important features of the individual $\pi^+ p \longrightarrow \pi\Delta$ transitions with fixed incident and final orbital angular momenta. In Section 5.5 the model used to fit the results at the four incident momenta is presented and the fitting procedure described in detail. Finally, in Section 5.6 we present the results of this phenomenological fit, the values of the reaction cross-sections and the inelasticities of the incident partial waves.

5.2 Earlier Models for single pion production

The first attempts to angular momentum analyse single pion production were made by Olsson and Yodh[14), 16), 17), 40)]. In this model attractive couplings between the pion and the nucleon only are considered in the final state. These are the Δ (1236) and the $I = 1/2$, $J = 1/2$ N^* around 1400 MeV. For each, either pion can be coupled to the nucleon, taking due account of I-spin conservation, to form isobars $(\pi_2 N')$ and $(\pi_1 N')$. Labelling these subsystems (1) and (2) the individual matrix elements are denoted by M^I (1) and M^I (2), I being the total isotopic spin. The overall amplitude is given by

$$M^I = \alpha^I (1) \; M^I (1) + \alpha^I (2) \; M^I (2) \tag{5.1}$$

where α^I are the Clebsch-Gordan coefficients connecting the initial I-spin state to the final I-spin state via the production and decay of the isobar. For the $\pi^+\pi^o p$ final state produced via the intermediate $\pi\Delta$ state

$$M^{3/2} = \sqrt{9/15}\; M^{3/2}(\pi^+ p) - \sqrt{4/15}\; M^{3/2}(\pi^o p) \tag{5.2}$$

Each matrix element is considered as a product of two parts - (i) a production matrix element for isobar production and (ii) a decay matrix element describing the isobar decay. The following notation is used:

L	-	incident orbital angular momentum
L'	-	relative orbital angular momentum of the recoil pion
J	-	total spin
j	-	spin of the isobar
and ℓ	-	relative orbital angular momentum of the decay in the isobar rest frame

and the transitions from the initial state specified by L to the quasi-two-body final state specified by L' are denoted by (JLL'). The matrix element is written as

$$M^{I,J,L}_{j,\ell,L'}(1) = P^{I,J,L}_{j,\ell,L'}(1) \cdot D^{j,\ell}(1) \qquad (5.3)$$

The production matrix element P is of the form

$$P^{I,J,L}_{j,\ell,L'}(1) \simeq a^{I,J,L,L'} \cdot \left(\frac{q}{m_i}\right)^L \cdot \left(\frac{p_2}{m_f}\right)^{L'} \cdot F_P^{J,L,L',j,\ell}(1) \qquad (5.4)$$

where $a^{I,\,J,\,L,\,L'}$ is the complex amplitude for the production 'vertex' for the transition (J, L, L'). The factors $(\frac{q}{m_i})^L$ and $(\frac{p_2}{m_f})^{L'}$ are approximations for the centrifugal barrier effects in the initial and final states with m_i and m_f as the reduced masses. $F_P(1)$ is the angular part of the matrix element in the centre of mass system. The decay matrix element is assumed to be of the form

$$D^{j,\ell}(1) \simeq \sqrt{\frac{\Gamma}{q_1'}} \cdot \frac{1}{m_{13} - m_0 - i\Gamma} \cdot F_D^{j,\ell}(1) \qquad (5.5)$$

for a resonance of mass M_0 and energy dependent width Γ. q_1' is the momentum of the decay pion and $F_D(1)$ is the angular part of the decay matrix element in the isobar rest frame. (5.4) and (5.5) separate out all angular effects of $M^{I,\,J,\,L}_{j,\,\ell\,,\,L'}$ (1) into a 2 x 2 matrix element connecting the nucleon spins in the initial and final states -

$$F\ (1) = F_P\ (1) \times F_D(2) \tag{5.6}$$

The modulus-squared of the matrix element, with appropriate transformations into a common frame of reference, is given by

$$\left| M^{I,J,L}_{j,\ell,L'} \right|^2 = \sum_{\mu_i \mu_f} \Big| \alpha^I(1) \cdot M_{\mu_i \mu_f}(I, J, L, L', j, \ell; 1) + \alpha^I(2) \cdot M_{\mu_i \mu_f}(I, J, L, L', j, \ell; 2) \Big|^2 \ldots \tag{5.7}$$

where μ_i and μ_j are the z-components of the nucleon spins in the initial and final states. For more than one transition contributing

$$|M|^2 = \sum_{\mu_i \mu_f} \Big| \sum_{J,L,L'} \cdot M^{I,J,L,\mu_i}_{j,\ell,L',\mu_f} \Big|^2 \tag{5.8}$$

The four variables, chosen by Olsson and Yodh, for the individual partial wave amplitudes are the kinetic energies - T_1 and T_2 - of the two pions, the cosine - μ_1 - of the centre of mass production angle of π_1 and the cosine -η- of the angle between the production and the decay planes.

Olsson and Yodh assume only S-wave production of the subsystems - the Δ and $N^*(1, 1)^-$. For the production of the Δ the only transition assumed is, therefore, the DS3 which gives a value for the ratio R, $=\sigma_{\pi^+\pi^0 p}/\sigma_{\pi^+\pi^+ n}$, slightly higher than the observed value. To improve the fit to both final states they include the $N^*(1, 1)^-$, in the PS1 transition, as background to the dominant DS3 $\pi\Delta$ transition. They obtain reasonable agreement with experiment at all incident energies around 1 GeV/c with constant strengths for the two amplitudes.

Since the S1, P3, D3, D5 and F5 partial waves are inelastic, around 1 GeV/c it seems unlikely that only the D3 wave is coupled to the dominant inelastic channels. Also, angular momentum and parity conservation allows D-wave production of the Δ from an incident D3 wave. The Olsson and Yodh model seems to oversimplify the situation as far as single pion production is concerned. With the poor statistical accuracy of the experimental data[22] it is not surprising that the model succeeded in explaining the features of single pion production. The choice of the DS3 as the only dominant partial wave is based on the behaviour of R as a function of incident energy and of $R_{M_{\pi\pi}}$ $\left(= \dfrac{d\sigma_{\pi^+\pi^0 p}}{dM_{\pi^+\pi^0}} \Big/ \dfrac{d\sigma_{\pi^+\pi^+ n}}{dM_{\pi^+\pi^+}}\right)$ as a function of $M_{\pi\pi}$ at fixed incident energies. In Figure 4.12 the values of $R_{M_{\pi\pi}}$, as obtained in the present experiment, are shown. The values, obtained by Olsson and Yodh, of $R_{M_{\pi\pi}}$ at 945 MeV/c for the DS3 transition and for the DS3-PS1 fit are also shown. The agreement between the curves and the present experimental results is rather poor.

5.3 The Formalism

Deler and Valladas[20] (DV) have set out a general formalism to partial wave analyse a reaction of the type

Meson (0^-) + Baryon $(\frac{1}{2}^+)$ $\longrightarrow$ Meson (0^-) + Meson (0^-) + Baryon $(\frac{1}{2}^+)$

where the final state particles exhibit strong attractive two-body couplings. We use a model based on this formalism to explain the single pion production results obtained in this experiment.

The amplitudes used by Olsson and Yodh are expressed in terms of the c.m. production angle (θ) of the two-body subsystem (henceforth - the isobar) and the angle (ϕ) between the decay and production planes, along with the kinetic energies of the mesons. DV use a more natural pair of angles - the polar angles (Θ Φ) of the incident pion with respect to a 3-particle system with its Z-axis along the normal to the production plane and the X-axis in the plane (see Figure 4.1) and set out the amplitudes in terms of the Dalitz plot co-ordinates and Θ, Φ.

If μ and ν define the initial and final nucleon spin states and the overall matrix element is $T_{\mu\nu}$ then the differential cross-section in the four variables is given by

$$d\sigma \propto \frac{1}{4 q_i W^3} \cdot \sum_{\mu\nu} | T_{\mu\nu} |^2 \, d\omega_1^2 \, d\omega_2^2 \, d\cos \textcircled{H} \, d\Phi \tag{5.9}$$

The notations and symbols used in (5.9) and the equations that follow are defined in Table 5.1. Considering the production of meson-baryon isobars of known spin and parity we can define a set of transitions from the initial state to the recoil particle - isobar state by the quantum number (J, L, L', j, ℓ). Hence

$$T_{\mu\nu} = \sum_{j,\ell} \cdot \sum_{J,L,L'} \left(T_{j,\ell}^{J,L,L'} \right)_{\mu\nu} \tag{5.10}$$

where the sum of j, ℓ signifies the sum over all possible isobar production. The formalism set out below applies to reaction (4.1).

For the production of the quasi-two body final state π_1^α $(\pi_2^\beta N')$, where α and β denote the third components of the pion isospins, in a particular transition (J, L, L', j, ℓ) the matrix element is written as

$$\left(T_{j,\ell}^{J,L,L'} \right)_{\mu\nu} = \frac{1}{2\pi} \sum_{I,i} \cdot C_{n,\alpha N}^{i\,1\,I} \cdot C_{\alpha\beta n_1}^{\frac{1}{2}\,1\,i} \cdot \sqrt{\frac{2J+1}{2}} \cdot \frac{4W\sqrt{4\omega_1}}{\sqrt{q_i q_1 q_1^*}} \cdot$$

$$\cdot\, T_{I,i}^{J,L,L';j,\ell}(W,\omega_1) \cdot f_{\mu\nu}^{J,L,L';j,\ell}\left(\theta_1^*, \frac{\theta_{12}}{2}, \textcircled{H}, \Phi\right) e^{i\nu\Omega_1} \tag{5.11}$$

where the X-axis of the three-particle system is chosen to be along the bisector of the two pion directions. The angle Ω_1 allows for the pure Lorentz transformation of the final nucleon spin from the isobar rest frame to the c.m. $f_{\mu\nu}^{J\,L\,L';\,j\,\ell}$ is the matrix element connecting the initial and final angular momentum states. It contains the complete angular dependence of the overall matrix element for the process $\pi N \rightarrow \pi_1 \; (\pi_2 N')$. Using the helicity formalism of Jacob and Wick[49] the expression obtained for the angular matrix element is

$$f_{\mu\nu}^{J,L,L';j,\ell}\left(\theta_1^*, \frac{\theta_{12}}{2}, \textcircled{H}, \Phi\right) = \sqrt{\frac{2J+1}{2L+1}} \sum_{\lambda>0} \sum_{M_f^*} \sum_{\mathcal{L}} \sum_{m} (-)^{\frac{1}{2}+j} \cdot$$

$$\cdot\, C^{J j \ell'}_{-\lambda \lambda 0} \cdot C^{\frac{1}{2} J \ell}_{m_f^* - \lambda - x} \cdot C^{\frac{1}{2} J \ell}_{\nu\, m-\nu\, m} \cdot d^{\ell}_{m, -x}\left(\frac{\pi}{2}\right) (i)^{x} \cdot P^{x}_{\ell}(\theta_1^*) \,.$$

$$\cdot\, C^{J\ \frac{1}{2}\ L}_{m-\nu\ \mu\ m-\nu+\mu} \cdot Y^{L}_{m-\nu+\mu}(\Theta, \Phi) \exp\left(i m \frac{\theta_{12}}{2}\right) \qquad (5.12)$$

where $x = \lambda - M_f^*$. The summation over ℓ extends from $|J - \frac{1}{2}|$ to $|J + \frac{1}{2}|$.

The angular amplitude for the production of the state $\pi_2^{\beta}\ (\pi_1^{\alpha} N)$ in the same frame o reference is

$$f^{J,L,L',j,\ell}_{\mu\nu}\left(-\theta_2^*, -\frac{\theta_{12}}{2}, \Theta, \Phi\right) = \text{-------}\ (-i)^{x} P^{x}_{\ell}(-\theta_2^*)\ \text{-------}\ \exp\left(-i m \frac{\theta_{12}}{2}\right). \qquad (5.13)$$

Performing all the summations in (5.4) and (5.5), except the summation over m , we get

$$\left.\begin{aligned} f^{J,L,L',j,\ell}_{\mu\nu}\left(\theta_1^*, \frac{\theta_{12}}{2}, \Theta, \Phi\right) &= \sum_m \left(a_m^{\mu\nu}\, i \sin\theta_1^* + b_m^{\mu\nu} \cos\theta_1^*\right) Y_L^m(\Theta, \Phi)\, e^{i m \frac{\theta_{12}}{2}} \\ f^{J,L,L',j,\ell}_{\mu\nu}\left(-\theta_2^*, -\frac{\theta_{12}}{2}, \Theta, \Phi\right) &= \sum_m \left(-a_m^{\mu\nu}\, i \sin\theta_2^* + b_m^{\mu\nu} \cos\theta_2^*\right) Y_L^m(\Theta, \Phi)\, e^{-i m \frac{\theta_{12}}{2}} \end{aligned}\right\} (5.14)$$

The four matrix elements for each isobar production with $\mu, \nu = \pm \frac{1}{2}$, are reduced to two independent elements by the general property $f_{-\mu,-\nu} = (-)^{\mu+\nu} f^*_{\mu,\nu}$. For the eight transitions SD1 to FP5, with the notation LL'2J, for $\pi N \to \pi\Delta$ the expressions for $f_{\mu\nu}$ (θ^*, 0, Θ, Φ) are given in Table 5.2.

If excitation of the $\Delta(3, 3)$ resonance alone is responsible for single pion production the overall amplitude is given by

$$\begin{aligned} T_{\mu\nu} &= \sum_{JLL'} T^{J,L,L';\frac{3}{2},1}_{\mu\nu} \\ &= \frac{1}{2\pi} \sum_{JLL'} \sum_I \sqrt{\frac{2J+1}{2}} \cdot \frac{4W}{\sqrt{q_i}} \left\{ C^{\frac{3}{2}\ 1\ I}_{n_1\ \alpha N}\ C^{\frac{1}{2}\ 1\ \frac{3}{2}}_{a \beta n_1} \sqrt{\frac{4\omega_1}{q_1 q_1^*}} \cdot T_I^{J,L,L';\frac{3}{2},1}(W, \omega_1) \,. \right. \\ &\cdot f^{J,L,L';\frac{3}{2},1}_{\mu\nu}\left(\theta_1^*, \frac{\theta_{12}}{2}, \Theta, \Phi\right). e^{i\nu\Omega_1} + C^{\frac{3}{2}\ 1\ I}_{n_2 \beta N}\ C^{\frac{1}{2}\ 1\ \frac{3}{2}}_{a \alpha n_2} \sqrt{\frac{4\omega_2}{q_2 q_2^*}} \cdot T_I^{J,L,L';\frac{3}{2},1}(W, \omega_2) \,. \\ &\left. \cdot f^{J,L,L';\frac{3}{2},1}_{\mu\nu}\left(-\theta_2^*, -\frac{\theta_{12}}{2}, \Theta, \Phi\right). e^{-i\nu\Omega_2} \right\} \end{aligned} \qquad (5.15)$$

$T_I^{JLL';\frac{3}{2},1}$ (W, w_i), dependent only on the total c.m. energy and the two particle invariant mass, is the matrix element between the initial and the final angular momentum eigenstates - viz.

$$\langle J\, M\, L';\, \tfrac{3}{2}\, 1;\, I\, \tfrac{3}{2}\, |T|\, J\, M\, L;\, \tfrac{1}{2};\, I \rangle \tag{5.16}$$

and can be considered to be the single pion production amplitude via the $\pi\Delta$ intermediate state in the (J, L') final wave from a (J, L) incident wave. It is factorised to separate out the Δ-production vertex amplitude from the Δ-decay amplitude and the centrifugal barrier effects.

$$T_{I,i}^{J,L,L';j,\ell}(W,\omega_k) = A_{I,i}^{J,L,L';j,\ell}(W).\left(\frac{q_i}{m_i}\right)^L.V(W,\omega_k)\left(\frac{q_k}{m_k}\right)^{L'} \tag{5.17}$$

where m_i and m_k are the reduced masses in the initial and the intermediate recoil particle - isobar states respectively. A is the complex production amplitude for the isobar and is determined by a fit to experiment. The factors $\left(\frac{q_i}{m_i}\right)^L$ and $\left(\frac{q_k}{m_k}\right)^{L'}$ are the approximate centrifugal barrier factors, as in the Olsson and Yodh model. V(W, w_k) represents the propagator and decay amplitude for the isobar given by

$$V(W,\omega_k) = \left(\frac{\omega_k}{q_k^*}\right)^{\frac{1}{2}} \cdot \frac{(\omega_o\Gamma)^{\frac{1}{2}}}{(\omega_o^2-\omega_k^2)-i\,\omega_o\Gamma} \tag{5.18}$$

where w_o is the mass of the resonance and Γ its energy-dependent width. This form is similar to the one - (4.5) - used in the resonance model fits of the preceding chapter. The decay distribution function $w(\cos\theta^*_k)$ in (4.5) is dropped since the spins and orbital angular momenta are properly treated in the present formalism. The forms for the energy dependence of Γ have been set out in Chapter 4 - equations (4.7) and (4.8).

The above formalism applies to the production of pion-nucleon isobars only.

For an attractive $(\pi\pi)$ coupling in the final state there are three angular momenta to be coupled. These are the relative angular momentum of the pions ℓ', in the dipion system, the spin of the recoil nucleon and the relative angular momentum, L'', of the nucleon-dipion system. By coupling ℓ' with the spin of the nucleon to give an angular momentum j' and by coupling this with L'' the calculations for the amplitude are similar to pion-nucleon isobar production case. The angular part of the matrix element is then $f_{\mu\nu}^{JLL'';\, j'\ell'}(\theta_3^*, \frac{\theta_{12}}{2} - \theta_{13}, \text{Ⓗ}, \Phi)$. In obtaining the expression for this the spin states of the nucleon are always considered in the c.m. systems and hence no pure Lorentz transformation is involved.

A π^+p initial state is a pure $I = 3/2$ state; the sum over I in (5.15) reduces to a single term. We write the amplitude for the process $\pi^+p \longrightarrow \pi\Delta$ for the transition (J, L, L') as

$$T_{\mu\nu}^{J,L,L'} = A^{J,L,L'}(W)\left(\frac{q_i}{m_i}\right)^L \left[T(\omega_1) f_{\mu\nu}^{J,L,L'}\left(\theta_1^*, \frac{\theta_{12}}{2}, \text{Ⓗ}, \Phi\right)\left(\frac{q_1}{m_1}\right)^{L'} + T(\omega_2) f_{\mu\nu}^{J,L,L'}\left(-\theta_2^*, -\frac{\theta_{12}}{2}, \text{Ⓗ}, \Phi\right)\left(\frac{q_2}{m_2}\right)^{L'}\right] \qquad (5.19)$$

with

$$T(\omega_1) = \alpha_1 V(W, \omega_1)$$

$$T(\omega_2) = \alpha_2 V(W, \omega_2) \qquad (5.20)$$

and $m_1 = m_2$.

For the $\pi^+p\pi^0$ final state $\alpha_1 = \frac{3}{\sqrt{15}}$ and $\alpha_2 = -\frac{2}{\sqrt{15}}$; while for the $\pi^+\pi^+n$ final state $\alpha_1 = \alpha_2 = -\frac{1}{\sqrt{15}}$ which includes an overall factor of $\frac{1}{\sqrt{2}}$ for Bose symmetry.

Since the dependence of the angular part of the matrix element on Ⓗ, Φ

is in terms of spherical harmonics it is trivial to determine the density distribution on the Dalitz plot for a given transition. The expressions obtained by integrating (5.9) over Θ, Φ are given in Table 5.3.

5.4 Features of the $\pi^+p \rightarrow \pi\Delta$ transitions

The amplitudes, set out in the preceding section, for the process $\pi^+p \rightarrow \pi\Delta$ include the isotopic spin Clebsch-Gordan coefficients for the production of the two charged states of the Δ and for their subsequent decay. The relative strengths of the two single pion production processes for a given transition (LL'2J) can be easily determined by integrating the appropriate expression in Table 5.3. The values of the ratio R, for $\pi^+p \rightarrow \pi\Delta$ transitions up to a maximum J of 5/2, are presented in Table 5.4. R, determined experimentally, decreases with energy from a value of about 6 at 895 MeV/c incident momentum to about 4.8 at 1040 MeV/c. The DS3 and PP1 are the only $\pi^+p \rightarrow \pi\Delta$ transitions that give the right order of magnitude of R. Following Olsson and Yodh, one would expect these two transitions to contribute strongly to single pion production around 1 GeV/c. The decrease with energy in the value of R seems to suggest a small contribution of FP5 at 1040 MeV/c, if not at an earlier momentum.

A study of R as a function of the two-pion effective mass at fixed centre of mass energy for a given transition can be undertaken by integrating the appropriate expression in Table 5.3 over the range of the pion-nucleon effective mass. The resultant values of $R(M_{\pi\pi})$ for the various $\pi^+p \rightarrow \pi\Delta$ transitions, at 995 MeV/c incident pion momentum are shown in figures 5.1a and 5.1b. As discovered by Olsson and Yodh the DS3 transition seems to follow the experiment, particularly over the middle $M_{\pi\pi}$ region. The high peak in $R(M_{\pi\pi})$ for the PP1 transition for values of $M_{\pi\pi}$ between 450 - 600 MeV rules out this transition as the dominant process contributing to single pion production. Distributions $R(M_{\pi\pi})$ for the DD3 and DD5 transitions are also reasonably close to experiment.

The DS3, DD3 and DD5 transitions are therefore expected to contribute strongly to single pion production with small, but not insignificant, contributions from the PP1, and perhaps the SD1 and PF3, transitions from a comparison of $R(M_{\pi\pi})$ with experiment.

Comparison of the experimental two-body invariant mass-squared distributions for the two single pion production channels with the predicted distributions for the individual transitions gives further information about the relative strengths of these transitions. Figures 5.2 to 5.5 show these distributions at 1040 MeV/c incident momentum. The curves in these figures are obtained by normalising to the total number of one-pion production events at 1040 MeV/c. They are not normalised to the individual histogram.

The transitions with $J = \frac{1}{2}$ show strong peaks in $(\pi\pi)$ mass distribution at the low and high mass ends - the SD1 transition more so than the PP1 transition. The presence of the former is thus ruled out and the amount of PP1 is expected to be small. The inelasticity of the incident $S_{\frac{1}{2}}$ partial wave is therefore expected to manifest itself in a final state different from the $\pi\Delta$ state.

Of the two $P_{3/2}$ transitions PP3 is likely to contribute more strongly in spite of its higher values of R and $R(M_{\pi\pi})$ than the PF3. The invariant mass distributionsfor this transition are generally more consistent with the experimental distributions in shape than those for PF3. A small PF3 contribution is certainly expected. Between them the PP3 and the PF3 transitions should account for the inelasticity of the $P_{3/2}$ incident wave.

Both $D_{3/2}$ transitions - the DS3 and the DD3 - are expected to contribute strongly to the process. It is obvious from figure 5.5 that the DS3 transition alone cannot explain all the features of one-pion production. The $M^2_{\pi^+\pi^+}$ distribution is clearly not well explained by the DS3 transition. The concentration of events in the high $M^2_{\pi^+\pi^+}$ region is better explained by the presence of the DD3 as well.

Of the two J = 5/2 incident transitions a strong contribution from the DD5 is suggested. A small contribution from the FP5 transition is perhaps likely at a 1040 MeV/c if only to give a lower value of R at this incident momentum.

The angular momentum barrier factor for the $\pi\Delta$ final state in the amplitude (5.17) has the effect of weighting more strongly the low invariant (π^+p) mass region of the Dalitz plot for non-zero L'. This weight is stronger for higher values of L'. It has been pointed out in the preceding chapter that the Δ^{++} peak in the (π^+p) invariant mass distribution appears about 30 MeV below the quoted mass of the Δ. As such one would expect the transitions with high values of L' to contribute strongly to single pion production.

5.5 The Model and the fitting procedure

The simple resonance model fits to the experimental Dalitz plot distributions have shown that Δ production with a recoil pion accounts for 60-70% of all single pion production, around 1 GeV/c. $\pi^+p \longrightarrow \pi\Delta$ is therefore the dominant inelastic process in this region. As such the highly inelastic incident partial waves - S1, P3, D3 and D5 - can be expected to go into this channel. The results of the various phase shift analyses of elastic pion-nucleon scattering are in disagreement about whether the I = 3/2 F5 wave is inelastic in this energy region.

The most likely $\pi^+p \rightarrow \pi\Delta$ transitions can be decided by studying the energy variation of

(i) the Legendre polynomial expansion coefficients - C_ℓ - for the $\cos\theta^*_{\pi^0}$ distribution for $\pi^+p \rightarrow \pi^0\,\Delta^{++}$ $(1.16 \leqslant M^2_{p\pi^+} \leqslant 1.3)$ a process that can be reasonably clearly selected from the $\pi^+p\pi^0$ final state, and

(ii) the moments C^M_L/D^M_L in the expansion, of the (Θ, Φ) distributions for the two single-pion production processes, in spherical harmonics.

Figure 4.17 shows the values of the C_ℓ's obtained. Coefficients C_5 - C_7 are significantly non-zero at the higher incident momenta. Under the formalism set out by Kraybill et al[47)] this suggests the presence of a small amount of F-wave production of the Δ^{++}. F-wave production of the Δ can be initiated from the incident P3 and F5 waves. We would expect the angular momentum barrier effects to favour the former.

A significantly non-zero and negative C_4 is explained by D-wave production of the Δ in a J = 5/2 state. The increasing negative value of this coefficient with energy suggests an increasing amount of P wave production with 5/2 total angular momentum. The values of C_4, therefore, suggest a strong DD5 transition at all incident momenta and a small amount of FP5 at the highest momentum.

The moments C_L^M/D_L^M - Figure 4.22 - are consistent with zero for values of $L \geqslant 7$. This implies that transitions with $J = 7/2$ are not needed. The significant non-zero values for $L = 6$ at the higher momenta suggest the presence of a small amount of the F5 incident partial wave. This lends support to the need for inclusion of the FP5 transition in the model. The presence of both the P3 and the D3 incident waves is suggested by the non-zero values for $L = 4$.

So in a model based on $\pi^+ p \rightarrow \pi\Delta$ as the dominant process giving rise to one-pion production around 1 GeV/c one needs to allow for transitions with $J = 5/2$ with orbital angular momentum between the incident pion and the proton equal to 3. Restricting the relative orbital angular momentum of the recoil pion and the Δ for the F5 incident wave to 1 we have eight possible transitions from SD1 to FP5. These are listed in Table 5.4 along with the values of the ratio R for these transitions at the four incident momenta.

The threshold incident pion momentum for the process $\pi^+ p \rightarrow \rho^+ p$ is 1060 MeV/c. However the high concentration of events in the high $M(\pi^+\pi^0)$ region is only explained in the resonance model by a small amount (8-13% of total single pion production) of ρ^+ production. This evidence forces us to include this process in the model for partial wave analysis of one-pion production. Due to the centre of mass momentum in the $\rho^+ p$ final state being small it is valid to assume that the ρ-meson and the proton are produced in an S-wave only. By parity and angular momentum conservation only an incident S1 wave can produce this final state.

The resonance model fits of Chapter 4 also require about 12-18% of 3-particle phase space in single pion production. A major part of this phase-space is required to explain the $\pi^+\pi^+ n$ final state. This suggests that production of other attractive two-body couplings which contribute more to the $\pi^+\pi^+ n$ than the $\pi^+ p\pi^0$ final state. Bowler and Cashmore[39] in a similar attempt to determine the inelasticities of the $I = 3/2$ incident partial waves introduced an $I = 2$ attractive $(\pi\pi)$ coupling produced in an S-wave from an incident P1 wave. Olsson and Yodh[14), 16), 17, 40)], on the other hand, included $I = \frac{1}{2}$ $(\pi - N)$ rescattering effect, with $J^P = \frac{1}{2}^-$.

We are restricting the model to production of resonating subsystems only. The lowest known $I = \frac{1}{2}$ (πN) resonance is the P11 Roper resonance with mass 1480 MeV and width of the order of 250 MeV. The threshold incident momentum for producing a nucleon resonance of this mass with a recoiling pion is 910 MeV/c. Only the 895 MeV/c momentum in this experiment is below this threshold. Moreover the width of this resonance is twice that of the ρ-meson and as such its production, at even lower incident momenta, than that of the present experiment, is not at all unlikely. As in the case of ρ production the centre of mass momentum in the $\pi(\pi N - 1480)$ final state is small. It is thus valid to assume that the recoil pion is produced in an S-wave relative to the (πN) resonance at and around 910 MeV/c incident momentum. Again, by parity and angular momentum conservation, the incident S1 wave feeds this final state.

The model, as outlined above, assumes that all single pion production is caused by the production and subsequent decay of the Δ $(I = 3/2,\ J^P = 3/2^+,\ M = 1236$ and $\Gamma = 120)$, the ρ^+ $(I = 1,\ J^P = 1^-,\ M = 765$ and $\Gamma = 125)$ and the N^* $(I = \frac{1}{2},\ J^P = \frac{1}{2}^+,\ M = 1480,\ \Gamma = 260)$ resonance with a recoil particle. Pure three-particle production, without any non-resonating final state interactions between the particles, is assumed to be negligible. The S1 (1640) resonance with I-spin = 3/2 is thus allowed to decay to $\pi\Delta$, $\rho^+ p$ or πN^* final states while the P3 (1690) and the D3 (1688) are assumed to decay to the $\pi\Delta$ final state only.

There are a total of ten amplitudes and ten phases to determine at each incident momentum by fitting the experimental data. The functional dependence of the transition amplitudes on Θ and Φ takes the form of spherical harmonics.

As such interference between transitions with different J^P values, for the incident partial waves, does not affect the Dalitz plot distribution. Interference between the three transitions - SD1 ($\pi^+p \rightarrow \pi\Delta$), SS1 ($\pi^+p \rightarrow \rho^+p$) and SS1 ($\pi^+p \rightarrow \pi N^*$) - involving the S1 incident partial wave has to be taken into account in fitting the Dalitz plot distribution. The same is true for the two P3 transitions and the two D3 transitions - the PP3 and PF3 and the DS3 and DD3 $\pi^+p \rightarrow \pi\Delta$ transitions. Hence a total of ten real amplitudes and four phase differences can be determined by fitting the Dalitz plot distributions alone.

Within the frame-work of this model it is clearly possible to determine reasonably accurately the dominant incident partial waves involved in single pion production. A description of the fitting procedure adopted to determine the 14 parameters, mentioned above, is presented below.

The procedure adopted is similar to the one used to determine the amounts of resonance production in the preceding chapter. At each incident momentum the two Dalitz plot distributions are fitted simultaneously. A 15 x 15 grid across the $M^2_{\pi^+\pi^0}$ .v. $M^2_{\pi^+p}$ distribution leads to about 180 rectangular bins with a significant area within the boundary. The smaller total number of events in the $\pi^+\pi^+n$ final state forces the use of a coarser grid (10 x 10) across the $M^2_{\pi^+\pi^+}$ .v. $M^2_{\pi^+n}$ distribution. This contributes a further 86 bins. The experimental number of events (N_i) in each bin is determined and bins with fewer than five events are rejected. This only affects a few bins in the boundary region in each Dalitz plot. A total of about 260 data points are used in the fit.

For a given set of values of the free parameters the fitted number of events (μ_i) in each bin is determined with overall normalisation condition

$$\sum_i \mu_i = \text{Total number of 3-body final state events observed.}$$

The best values of the parameters are obtained by minimising the total chi-square MINUIT[50] is used to perform the minimisation.

Preliminary fits with widely different starting values for the parameters were done to study the behaviour of the χ^2 over a wide region of the 14-dimensional space. These led to the following conclusions:

(i) The function $-\chi^2$ - has a single unique minimum independent of the starting values.

(ii) At 895, 945 and 995 MeV/c the amplitude for the FP5 transition is consistently zero. Fits at these incident momenta with FP5 amplitude fixed to zero give essentially the same χ^2.

(iii) The phase difference between the two D3 transitions - the DS3 and DD3 - is equal to $-\pi$ at all incident momenta.

(iv) The SD1 transitions appear to be consistently π out of phase with each of the other two S1 transitions - the SS1 ($\pi^+p \rightarrow \pi^+N^*$) and SS1 ($\pi^+p \rightarrow \rho^+p$). This implies that the two SS1 transitions are in phase over this energy region.

The final fits were thus done with FP5 fixed to zero at 895, 945 and 995 MeV/c and with the above mentioned phase differences fixed. The phase difference between the two P3 transitions varies with energy.

5.6 Results and Conclusions

The final values of the parameters obtained at each momentum are given in Table 5.5. The effective mass-squared distributions, projected out from the final fits for each of the two 3-particle final states are shown in figures 4.4 to 4.11. These fits are clearly an improvement on the resonance model fits of the preceding chapter, especially for the $\pi^+\pi^+n$ final state. It is clear, from Table 5.6, that the model is able to explain the energy variation of the ratio (R) between the two channels. Figure 5.6 shows excellent agreement between the fitted and experimental values of R as a function of the two-pion effective mass at each energy.

The main aim of this analysis is to determine the inelastic cross-sections for the various incident partial waves and hence to evaluate the inelasticity parameters. The cross-sections and the values of η for the S1, P1, P3, D3, D5 and F5 partial waves are given in Table 5.7. A direct comparison of the inelasticities with the results of the elastic phase shift analyses can be made by looking at the energy variation of $(1 - \eta^2_{\ell\pm})$. Figure 5.7 shows these along with the results of Bowler and Cashmore[39] from a similar analysis in the 600-800 MeV/c region and the values obtained by the 'CERN Theoretical' and the 'Berkeley Path 1'[51] phase shift analyses.

The main conclusions of this analysis of single pion production around 1 GeV/c for the individual incident I = 3/2 pion-nucleon partial waves follow:

(a) S_{31}

In this model this wave is coupled to three inelastic final states - $\pi\Delta$ (1236) in a D wave, the $\pi^+N^{*+}(1, 1^+)$ in an S wave and the ρ^+p in an S wave. In agreement with the Bowler et al. results, this wave appears to be weakly coupled to the $\pi\Delta$ final state. We estimate the branching ratio - $(S_{31} \rightarrow \pi\Delta)/(S_{31} \rightarrow$ all inelastic channels) - to be around 0.15 - 0.20. The dominant decay mode is π^+N^{*+} with a branching ratio of around 0.5 - 0.7.

The inelasticity of this wave is considerably smaller than that suggested by the results of the elastic phase shift analyses. It is unlikely that the amount of the contribution to this wave is underestimated; the threshold for the production of a π-π coupling with a central mass of 765 MeV is above the present energy region. The $I = \frac{1}{2}$ $J^P = \frac{1}{2}^+$ π - N coupling at 1470 MeV, it has been pointed out, is the dominant coupling produced from this wave. This coupling has a branching ratio of decay to the elastic and the $N\pi\pi$ channel of 60 : 40. The analysis provides an estimate of the amount of the production of the π^+N^{*+} state decaying into a three body final state. This enables us to evaluate the amount of four body final states produced via this intermediate quasi-two-body state from an incident S1 wave. Table 5.8 gives the inelasticity parameter η, $(1 - \eta^2)$ and σ_{in} for this wave including this estimated 4-body contribution to this wave. Only the values at the highest momentum are consistent with the CERN results and whereas the CERN results show a falling cross-section we find a rising cross-section with energy.

The model used by Bowler and Cashmore does not couple the S_{31} wave to the π^+N^{*+} final state. Since they find that the wave is weakly coupled to the $\pi\Delta$ state they get most of the inelasticity in the ρ^+p final state. Being even lower in energy than the present experiment it seems they overestimate the amount of ρ-meson production.

The inelastic cross-section for this wave (with or without the 4-body contribution from the π^+N^{*+} shows a rising cross-section with energy. The results from the present analysis, within the energy range covered, are consistent with resonance scattering in this wave.

(b) P_{31}

The model assumes that the only inelastic channel to which this wave is coupled is the $\pi\Delta$ only. The fits show - Figure 5.7 - considerable inelasticity at the lowest momenta falling to zero at the highest. This is in good agreement with Berkeley results. The CERN results show practically no inelasticity in this partial wave over this energy region.

The model of Bowler et al. allows this wave to feed a final state with a nucleon as a recoil particle with an $I = 2$ $(\pi\pi)$ coupling - a PS1 transition - as well as a P wave $\pi\Delta$ final state. The inelasticity they determine agrees well with the inelasticity from the analysis at 895 MeV/c.

The sharp fall in the inelasticity seems to suggest strong structure in the partial wave near 1 GeV/c.

(c) P_{33}

The amount of inelasticity agrees with the CERN results at lowest momentum. The present results, however, show a sharp increase above 950 MeV/c. Again this energy variation is consistent with Berkeley results rather than the CERN results.

Bowler and Cashmore seem to find a lower inelasticity between 600 - 800 MeV/c than the CERN results. This wave can feed the $\pi\Delta$ state in an F besides a P wave. The present analysis indicates a significant amount of F wave production of the $\pi\Delta$ state even at the lowest momentum. The absence of the PF3 transition in the Bowler and Cashmore model could explain the lower inelasticity they observe in the P_{33} wave.

The results clearly do indicate the presence of resonance scattering in this wave, but seem to suggest sharper structure than seen by the CERN results.

(d) D_{33}

The inelasticity in this wave agrees well with the CERN results and is significantly higher than the Berkeley results. Together with the results of Bowler and Cashmore the results are consistent with a broad resonance in this partial wave.

(e) D_{35}

The fits show a surprisingly large inelasticity for this partial wave around 1 GeV/c. The inelastic cross-section goes through a peak of 5.15 mb. in this region. The Berkely results show a similar rise in the inelasticity followed by an even more dramatic fall to almost zero at 1 GeV/c. A similar energy behaviour is observed by the Saclay[7)] phase shift analysis in this partial wave. CERN results are in complete disagreement with these results.

It is clear that inelastic scattering in this wave has a striking structure not dissimilar to resonant behaviour. An eyeball fit to the inelastic cross-section (including the results of Bowler and Cashmore) suggests a resonance at 1640 MeV with a width of about 80 $\pm$ 20 MeV.

(f) F_{35}

The amplitude for this wave is small and as it is determined by fitting the Dalitz plot distributions alone the results are likely to be inaccurate. The fits require the amplitude to be zero below 1 GeV/c. At the highest momentum the inelasticity is small but significantly non-zero. This is in reasonable agreement with the CERN values of the inelasticity in this region. Over the present energy the inelasticities for this partial wave are in good agreement with the Saclay[7)] results. The Berkeley analysis, however, shows a high and rising inelasticity for this partial wave.

The rising P_{33} and D_{33} inelastic cross-sections over this energy region are consistent with the presence of resonances in these partial waves at around 1690 MeV, as reported by the elastic phase shift analyses. The inelasticities of these waves are well explained by the $\pi\Delta$ inelastic final state alone. The results for the S_{31} wave provide similar evidence for resonant behaviour. But the inelasticity in this wave is considerably lower than that determined by the analysis of elastic scattering. The reported S_{31} (1640) resonance is weakly coupled to the $\pi\Delta$ final state - a similar conclusion is reached by Bowler and Cashmore from their analysis of single pion production from 600 - 800 MeV/c. The present results also suggest the existence of considerable structure in the P_{31} and D_{35} waves over this energy region in agreement with the results of the Saclay and the 'Berkeley Path 1' phase shift analyses.

It should be pointed out again that the results described above have been determined by fitting the Dalitz plot distributions alone for the $\pi^+\pi^0p$ and $\pi^+\pi^+n$ final states and that fitting the (Θ, Φ) - see Figure 4.1 - distributions along with the Dalitz plots could be expected to result in slight adjustments to the amplitudes for the various transitions. Particularly, the smaller amplitudes would be more accurately fixed. The general conclusions, however, are not expected to be altered.

Table 5.1

Notations and Symbols

$\vec{q}_i$	Momentum of the incident pion in c.m. $OZ = \dfrac{\vec{q}_i}{\lvert\vec{q}_i\rvert}$ OX in the production plane
W	Total energy in the c.m.
J, M, L	Total angular momentum, its third component and relative orbital angular momentum in the initial state
m_i	Reduced mass in the initial state
$\vec{q}_{1(2)}$	Momentum of $\pi_{1(2)}$ in the c.m.
θ_1, ϕ_1	Polar angles of the $(\pi_2 N)$ subsystem in the c.m. relative to the OXYZ frame
$\omega_{1(2)}$	Invariant mass of the $(\pi_{2(1)} N)$ subsystem
j, λ	Spin and helicity of the 2-particle - (πN) - subsystem
ℓ, x	Orbital angular momentum of (πN) subsystem and its third component along OZ^*. $OZ^* = \dfrac{\vec{q}_{1(2)}}{\lvert\vec{q}_{1(2)}\rvert}$
$\vec{q}^{\,*}_{1(2)}$	Momentum of the nucleon in the $(\pi_{2(1)} N)$ subsystem rest frame.
$\theta^*_{1(2)}$, $\phi^*_{1(2)}$	Polar angles of the nucleon in the $OX^* Y^* Z^*$ frame. OX^* is in the X - Z plane.
L'	Relative orbital angular momentum of the recoil pion and the (πN) subsystem.
θ_{12}	Angle between π_1 and π_2 in c.m.
θ_{13}	Angle between π_1 and N in c.m.
I, N	Total I-spin and its third component.
i, $n_{1(2)}$	Isospin of the subsystem $(\pi_{2(1)} N)$ and its third component.
a	Third component of the nucleon isospin.
C^{abc}_{def}	Clebsch-Gordan Coefficients

Table 5.2

Angular Amplitudes

A) $\pi N \longrightarrow \pi\Delta$ $(I = 3/2,\ J^P = 3/2^+)$

	WAVE	SPIN FLIP OR NON-FLIP	AMPLITUDE $f_{\mu\nu}$ $(\theta^*, 0, \Theta, \Phi)$
1)	SD1	NSF	0
		SF	$\frac{1}{2\sqrt{2}}(i\sin\theta^* + 2\cos\theta^*)\, Y_0^0(\Theta, \Phi)$
2)	PP1	NSF	$-\frac{1}{2\sqrt{6}}(i\sin\theta^* + 2\cos\theta^*)\, Y_1^0$
		SF	$-\frac{1}{2\sqrt{3}}(i\sin\theta^* + 2\cos\theta^*)\, Y_1^{-1}$
3)	PP3	NSF	$-\frac{1}{2\sqrt{30}}(5i\sin\theta^* + \cos\theta^*)\, Y_1^0$
		SF	$\frac{1}{4\sqrt{15}}\left[(5i\sin\theta^* + \cos\theta^*)Y_1^{-1} + 3(i\sin\theta^* - \cos\theta^*)Y_1^1\right]$
4)	PF3	NSF	$\frac{3}{2\sqrt{30}}\cos\theta^*\, Y_1^0$
		SF	$-\frac{3}{4\sqrt{15}}\left[\cos\theta^* Y_1^{-1} - (2i\sin\theta^* + 3\cos\theta^*)\, Y_2^1\right]$
5)	DS3	NSF	$-\frac{3}{4\sqrt{15}}\left[(i\sin\theta^* + \cos\theta^*)Y_2^{-1} + (i\sin\theta^* - \cos\theta^*)Y_2^{+1}\right]$
		SF	$-\frac{1}{2\sqrt{5}}\left[\sqrt{3}(i\sin\theta^* + \cos\theta^*)Y_2^{-2} + \frac{1}{\sqrt{2}}(i\sin\theta^* - \cos\theta^*)Y_2^0\right]$
6)	DD3	NSF	$\frac{3}{4\sqrt{15}}\left[\cos\theta^* Y_2^{-1} - (2i\sin\theta^* + \cos\theta^*)\, Y_2^1\right]$
		SF	$\frac{1}{2\sqrt{5}}\left[\sqrt{3}\cos\theta^* Y_2^{-2} - \frac{1}{\sqrt{2}}(2i\sin\theta^* + \cos\theta^*)\, Y_2^0\right]$
7)	DD5	NSF	$\frac{1}{2\sqrt{35}}\left[(5i\sin\theta^* + \cos\theta^*)Y_2^{-1} - (2i\sin\theta^* + \cos\theta^*)Y_2^1\right]$
		SF	$-\frac{1}{2\sqrt{35}}\left[\frac{1}{2}(5i\sin\theta^* + \cos\theta^*)Y_2^{-2} + \frac{3}{\sqrt{6}}(2i\sin\theta^* + \cos\theta^*)Y_2^0\right]$
		NSF	$\frac{3}{4\sqrt{7}}\left[\frac{1}{\sqrt{3}}(i\sin\theta^* + \cos\theta^*)\, Y_3^{-2} - \frac{2}{\sqrt{10}}\cos\theta^* Y_3^0 + \frac{1}{\sqrt{3}}(i\sin\theta^* - \cos\theta^*)_3\right.$

	WAVE	SPIN FLIP OR NON-FLIP	AMPLITUDE $f_{\mu\nu}$ $(\theta^*, 0, Ⓗ, \Phi)$
8)	FP5	SF	$\frac{3}{2\sqrt{14}}\left[(i\sin\theta^* + \cos\theta^*)Y_3^{-3} - \frac{2}{\sqrt{15}}\cos\theta^* Y_3^{-1} + \frac{1}{\sqrt{15}}(i\sin\theta^* - \cos\theta^*)Y_3^{1}\right]$
B)	$\pi N \rightarrow \pi N^*$ $(I = 1/2,\ J^P = 1/2^+)$		
9)	SS1	NSF	0
		SF	$\frac{1}{2}(i\sin\theta^* - \cos\theta^*)Y_0^0$
C)	$\pi N \rightarrow \pi N^*$ $(I = 1/2,\ J^P = 1/2^-)$		
10)	PS1	NSF	$\frac{1}{2\sqrt{3}} \cdot Y_1^0$
		SF	$\frac{1}{\sqrt{6}} \cdot Y_1^{-1}$
D)	$\pi N \rightarrow N\rho$ $(I = 1,\ J^P = 1^-)$		
11)	SS1	NSF	0
		SF	$\frac{1}{2}(i\sin\theta^* - \cos\theta^*)\ e^{-i\theta_{13}}\ Y_0^0$

Table 5.3

Dalitz Plot Density Distributions

WAVE	DISTRIBUTION

A) $\pi N \to \pi\Delta$ waves

1) SD1

$$\propto |T(\omega_1)|^2(1+3\cos^2\theta_1^*)\left(\frac{q_1}{m_1}\right)^4+|T(\omega_2)|^2(1+3\cos^2\theta_2^*)\left(\frac{q_2}{m_2}\right)^4+$$
$$+2\mathrm{Re}\left[T^*(\omega_1)\,T(\omega_2)\right]\left[\cos(\theta_1^*+\theta_2^*+\theta_{12})+3\cos\theta_{12}\cos\theta_1^*\cos\theta_2^*-\right.$$
$$\left.-\sin\theta_{12}\sin(\theta_1^*+\theta_2^*)\right]\left(\frac{q_1q_2}{m_1m_2}\right)^2$$

2) PP1

$$\propto |T(\omega_1)|^2(1+3\cos^2\theta_1^*)\left(\frac{q_1}{m_1}\right)^2+|T(\omega_2)|^2(1+3\cos^2\theta_2^*)\left(\frac{q_2}{m_2}\right)^2+$$
$$+2\mathrm{Re}\left[T^*(\omega_1)\,T(\omega_2)\right]\left[3\cos\theta_1^*\cos\theta_2^*+\cos(\theta_1^*+\theta_2^*)\right]\left(\frac{q_1q_2}{m_1m_2}\right)$$

3) PP3

$$\propto |T(\omega_1)|^2(4+24\sin^2\theta_1^*)\left(\frac{q_1}{m_1}\right)^2+|T(\omega_2)|^2(4+24\sin^2\theta_2^*)\left(\frac{q_2}{m_2}\right)^2+$$
$$+2\mathrm{Re}\left[T^*(\omega_1)\,T(\omega_2)\right]\left[\cos(\theta_1^*+\theta_2^*)+3\cos(\theta_1^*+\theta_2^*-2\theta_{12})-\right.$$
$$\left.-24\sin\theta_1^*\sin\theta_2^*\right]\left(\frac{q_1q_2}{m_1m_2}\right)$$

4) PF3

$$\propto |T(\omega_1)|^2(4+8\cos^2\theta_1^*)\left(\frac{q_1}{m_1}\right)^6+|T(\omega_2)|^2(4+8\cos^2\theta_2^*)\left(\frac{q_2}{m_2}\right)^6+$$
$$+2\mathrm{Re}\left[T^*(\omega_1)\,T(\omega_2)\right]\left[\cos\theta_1^*\cos\theta_2^*(3+5\cos2\theta_{12})+4\cos(\theta_1^*+\theta_2^*+2\theta_{12})\right.$$
$$\left.-2\sin2\theta_{12}\sin(\theta_1^*+\theta_2^*)\right]\left(\frac{q_1q_2}{m_1m_2}\right)^3$$

5) DS3

$$\propto |T(\omega_1)|^2+|T(\omega_2)|^2+2\mathrm{Re}\left[T^*(\omega_1)\,T(\omega_2)\right]\cos(\theta_1^*+\theta_2^*-\theta_{12})$$

6) DD3

$$\propto |T(\omega_1)|^2\left(\frac{q_1}{m_1}\right)^4 + |T(\omega_2)|^2\left(\frac{q_2}{m_2}\right)^4 + 2Re\left[T^*(\omega_1)T(\omega_2)\right]\cdot$$

$$\cdot\left[\cos(\theta_1^* + \theta_2^* + \theta_{12}) + \cos\theta_{12}\cos(\theta_1^* + \theta_2^*)\right]\left(\frac{q_1 q_2}{m_1 m_2}\right)^2$$

---

7) DD5

$$\propto |T(\omega_1)|^2(8+30\sin^2\theta_1^*)\left(\frac{q_1}{m_1}\right)^4 + |T(\omega_2)|^2(8+30\sin^2\theta_2^*)\left(\frac{q_2}{m_2}\right)^4 +$$

$$+ 2Re\left[T^*(\omega_1)T(\omega_2)\right]\left[\cos(\theta_1^* + \theta_2^* - \theta_{12}) + 2\cos\theta_{12}\cos(\theta_1^* + \theta_2^*) -\right.$$

$$\left. - 30\cos\theta_{12}\sin\theta_1^*\sin\theta_2^* + 5\cos(\theta_1^* + \theta_2^* - 3\theta_{12})\right]\left(\frac{q_1 q_2}{m_1 m_2}\right)^2$$

---

8) FP5

$$\propto |T(\omega_1)|^2(3+\cos^2\theta_1^*)\left(\frac{q_1}{m_1}\right)^2 + |T(\omega_2)|^2(3+\cos^2\theta_2^*)\left(\frac{q_2}{m_2}\right)^2 +$$

$$+ 2Re\left[T^*(\omega_1)T(\omega_2)\right]\left[\cos\theta_1^*\cos\theta_2^* + 3\cos(\theta_1^* + \theta_2^* - 2\theta_{12})\right]\left(\frac{q_1 q_2}{m_1 m_2}\right)$$

Note:- $m_1 = m_2$

B) $\pi N \rightarrow \pi N^*$ $(I = \frac{1}{2},\ J^P = \frac{1}{2}^+)$

9) SS1

$$\propto |T(\omega_1)|^2 + |T(\omega_2)|^2 + 2Re\left[T^*(\omega_1)T(\omega_2)\right]\cos(\theta_1^* + \theta_2^* - \theta_{12})$$

C) $\pi N \rightarrow \pi N^*$ $(I = \frac{1}{2},\ J^P = \frac{1}{2}^-)$

10) PS1 $\quad \propto |T(\omega_1)|^2 + |T(\omega_2)|^2 + 2Re\left[T^*(\omega_1)T(\omega_2)\right]$

D) $\pi N \rightarrow \rho N$

11) SS1 $\quad \propto |T(\omega_3)|^2$

Table 5.4

$$R = \frac{(\pi^+ p \rightarrow \pi^+ \pi^0 p)}{(\pi^+ p \rightarrow \pi^+ \pi^+ n)} \quad \text{for } \pi^+ p \longrightarrow \pi\Delta \text{ Transitions}$$

Incident Momentum MeV/c ⟶	895	945	995	1040
Transition (L, L', 2J)				
SD1	7.53	7.51	7.48	7.46
PP1	5.59	5.65	5.68	5.71
PP3	12.00	11.67	11.38	11.15
PF3	7.55	7.53	7.51	7.50
DS3	5.77	5.77	5.76	5.76
DD3	6.89	6.89	6.89	6.89
DD5	6.87	6.87	6.87	6.87
FP5	3.74	3.86	3.95	4.04
Experimental	5.96 ± 0.21	5.69 ± 0.18	5.04 ± 0.16	4.76 ± 0.16

Table 5.5

Final Values of the Parameters

a) Moduli of the transition amplitudes

Incident Momentum / Transition	895	945	995	1040
SD1	1.05 ± 0.32	0.884 ± 0.152	0.987 ± 0.170	0.861 ± 0.136
PP1	2.30 ± 0.18	1.97 ± 0.18	1.04 ± 0.33	0.0 ± 0.63
PP3	1.33 ± 0.11	0.933 ± 0.105	1.60 ± 0.08	1.38 ± 0.05
PF3	0.191 ± 0.024	0.122 ± 0.017	0.162 ± 0.010	0.155 ± 0.011
DS3	1.01 ± 0.07	0.936 ± 0.006	1.09 ± 0.07	1.21 ± 0.11
DD3	0.122 ± 0.018	0.092 ± 0.013	0.052 ± 0.017	0.047 ± 0.13
DD5	0.158 ± 0.019	0.169 ± 0.008	0.127 ± 0.010	0.094 ± 0.008
FP5	0*	0*	0*	0.039 ± 0.007
SS1 (π^+N^{*+})	15.5 ± 1.0	16.6 ± 0.79	24.8 ± 0.8	23.7 ± 1.0
SS1 (ρ^+p)	22.5 ± 4.7	18.3 ± 1.5	16.5 ± 2.0	13.1 ± 1.3

b) Phase differences (in radians)

L_{2J} (Final states)	895	945	995	1040
S_1 $D(\pi\Delta/S(\pi^+N^{*+})$	π^*	π^*	π^*	π^*
S_1 $D(\pi\Delta/S(\rho^+p)$	π^*	π^*	π^*	π^*
D_3 $S(\pi\Delta)/D(\pi\Delta)$	$-\pi^*$	$-\pi^*$	$-\pi^*$	$-\pi^*$
P_3 $P(\pi\Delta)/F(\pi\Delta)$	-1.73 ± 0.22	-2.43 ± 0.18	-1.82 ± 0.15	-1.34 ± 0.12

* Fixed value

c) Goodness-of-Fit

Momentum (MeV/c)	895	945	995	1040
$G = \chi^2/ND$	2.11	1.70	1.96	1.92

Table 5.6

The Ratio ($R = \sigma_{\pi^+ p \pi^0} / \sigma_{\pi^+ \pi^+ n}$)

Incident Momentum in MeV/c	R (experimental)	R (from fit)
895	5.96 ± 0.21	5.95
945	5.69 ± 0.18	5.62
995	5.04 ± 0.16	5.05
1040	4.76 ± 0.16	4.88

Table 5.7

$\sigma_{inelastic}$ and η_l for the incident partial waves

Centre of mass energy (MeV) / $L_{2I,\,2J}$		1612	1641	1669	1694
S_{31}	σ	0.89 ± 0.10	1.03 ± 0.04	1.66 ± 0.08	1.52 ± 0.07
	η	0.896 ± 0.012	0.868 ± 0.055	0.758 ± 0.014	0.765 ± 0.012
P_{31}	σ	1.72 ± 0.19	1.51 ± 0.20	0.41 ± 0.18	0.0
	η	0.789 ± 0.026	0.798 ± 0.030	0.946 ± 0.024	1.0
P_{33}	σ	2.650 ± 0.21	1.59 ± 0.20	4.02 ± 0.21	3.88 ± 0.21
	η	0.840 ± 0.017	0.900 ± 0.013	0.696 ± 0.020	0.688 ± 0.021
D_{33}	σ	3.57 ± 0.34	3.20 ± 0.30	3.14 ± 0.29	3.94 ± 0.47
	η	0.777 ± 0.024	0.786 ± 0.023	0.772 ± 0.024	0.682 ± 0.047
D_{35}	σ	3.10 ± 0.53	5.15 ± 0.35	3.42 ± 0.36	2.41 ± 0.29
	η	0.839 ± 0.030	0.768 ± 0.018	0.840 ± 0.018	0.885 ± 0.015
F_{35}	σ	0.0	0.0	0.0	0.85 ± 0.20
	η	1.0	1.0	1.0	0.960 ± 0.009

Table 5.8

S_{31} Partial Wave

Inelasticity - $(1-\eta^2)$ - estimates including the 4-body contribution from the π^+N^{*+} (1470) intermediate state

Momentum (MeV/c)	Present Analysis			CERN Results*		
	σ_{in} (mb)	η	$1-\eta^2$	σ_{in} (mb)	η	$1-\eta^2$
895	1.18	0.86	0.26	3.6	0.45	0.80
945	1.42	0.82	0.33	3.5	0.41	0.83
995	2.41	0.62	0.62	3.1	0.46	0.79
1040	2.21	0.63	0.60	2.68	0.55	0.70

* η-values interpolated from values at near-by momenta

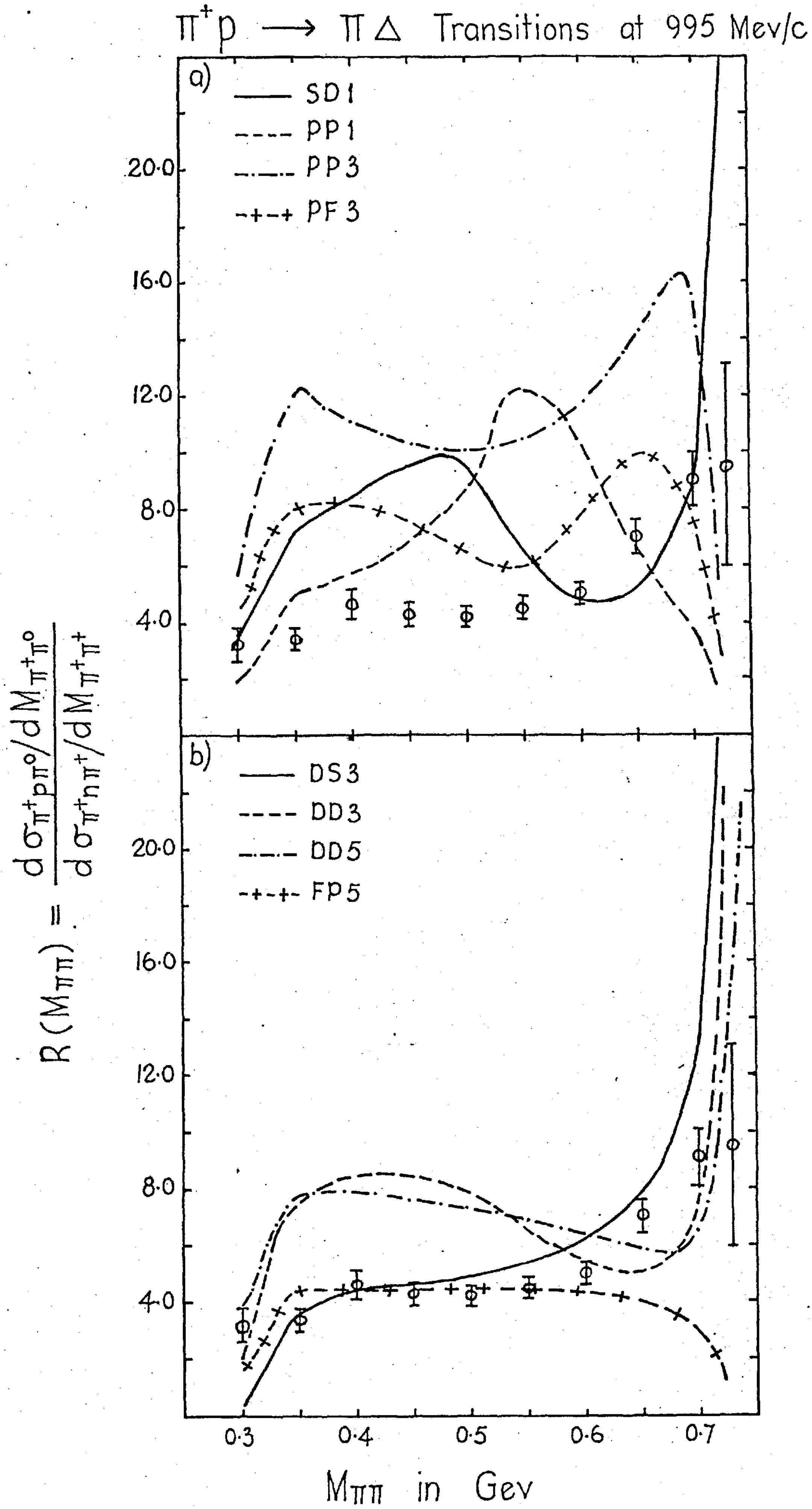

$\pi^+ p \longrightarrow \pi\Delta$ Transitions at 995 Mev/c
a)
SD1
PP1
PP3
PF3
b)
DS3
DD3
DD5
FP5
20·0
16·0
12·0
8·0
4·0
$R(M_{\pi\pi}) = \dfrac{d\sigma_{\pi^+ p\pi^0}/dM_{\pi^+\pi^0}}{d\sigma_{\pi^+ n\pi^+}/dM_{\pi^+\pi^+}}$
0·3
0·4
0·5
0·6
0·7
$M_{\pi\pi}$ in Gev

Fig. 5·1

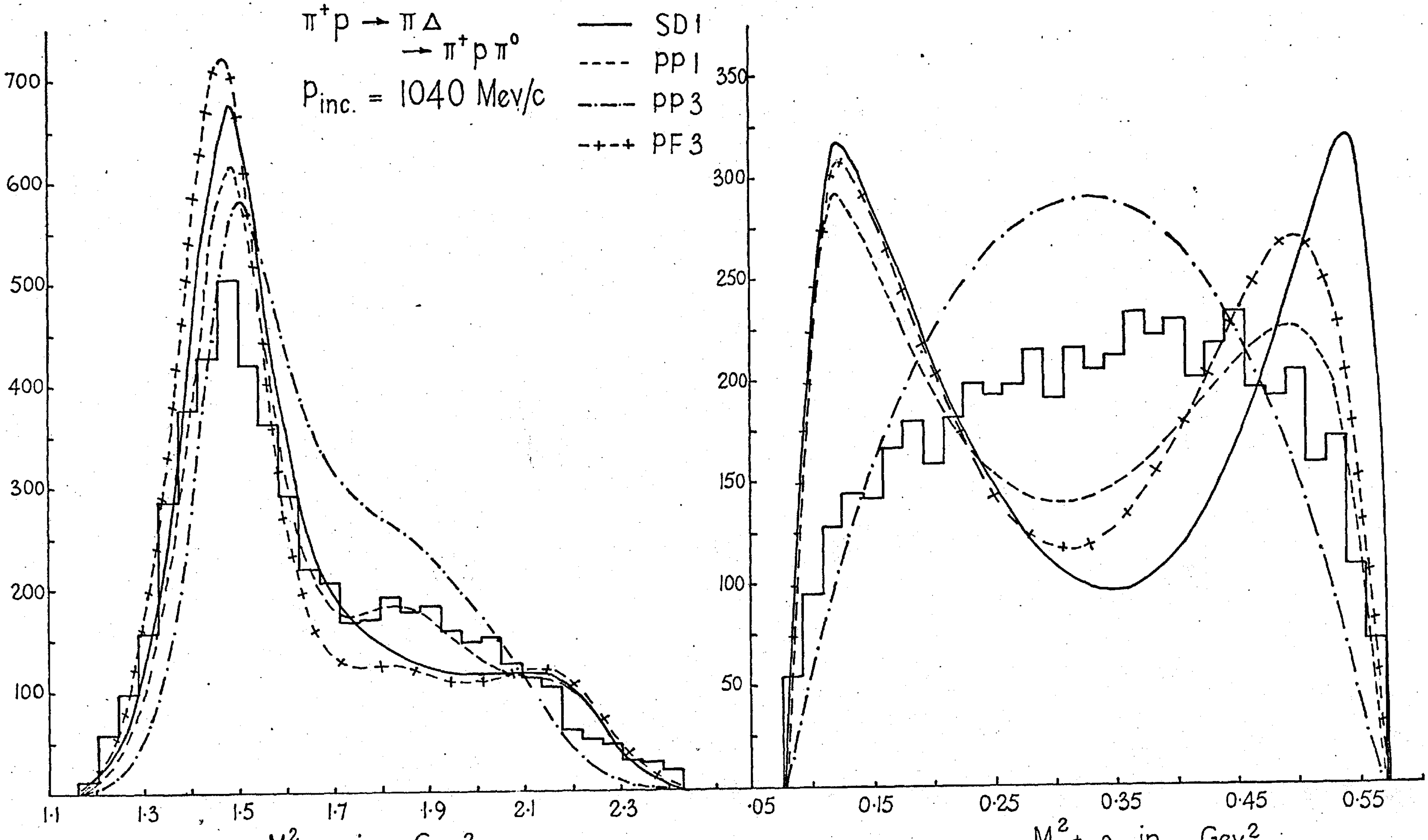
$\pi^+ p \to \pi \Delta$
$\to \pi^+ p \pi^0$
$p_{inc.} = 1040$ Mev/c
SD1
PP1
PP3
PF3
$M^2_{p\pi^+}$ in Gev^2
$M^2_{\pi^+\pi^0}$ in Gev^2

Fig. 5·2

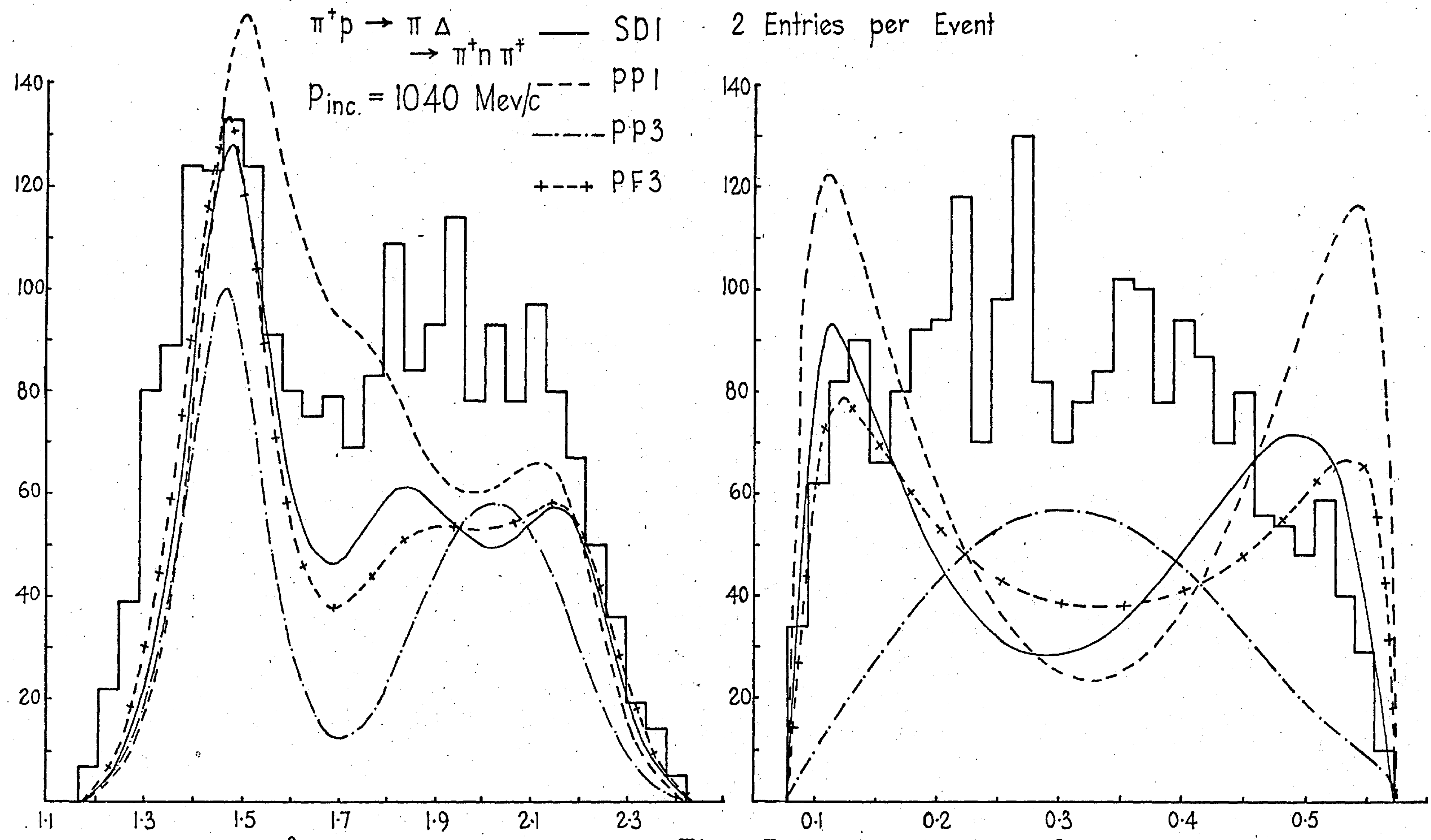

π⁺p → π Δ
→ π⁺n π⁺
P_inc. = 1040 Mev/c
SD1
pp1
pp3
PF3
2 Entries per Event
140
120
100
80
60
40
20
1·1
1·3
1·5
1·7
1·9
2·1
2·3
0·1
0·2
0·3
0·4
0·5
$M^2_{\pi^+ n}$ in Gev²
$M^2_{\pi^+\pi^+}$ in Gev²

Fig. 5·3

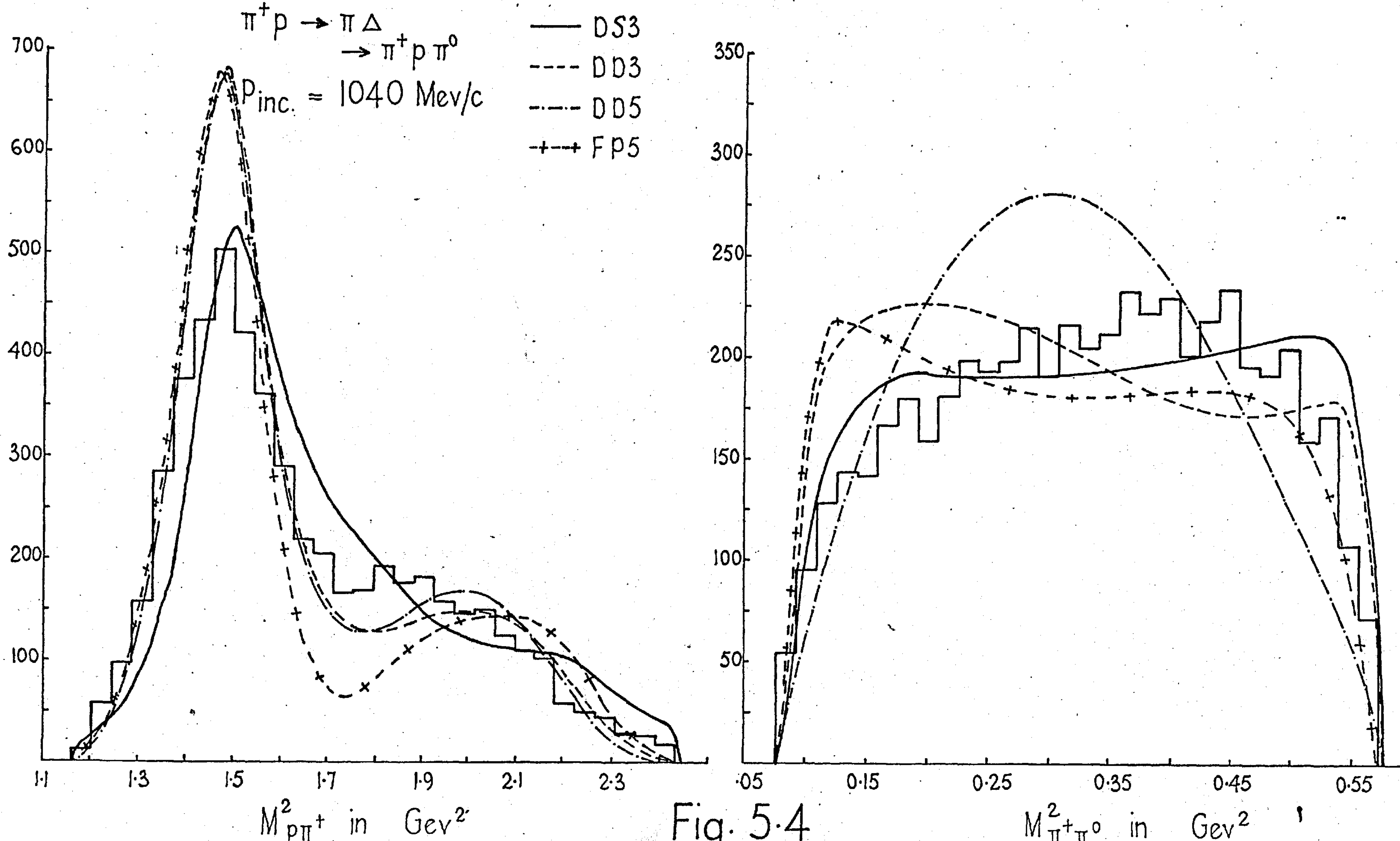

$\pi^+ p \rightarrow \pi \Delta$
$\rightarrow \pi^+ p \pi^0$
$P_{inc.} = 1040$ Mev/c
DS3
DD3
DD5
FP5
700
600
500
400
300
200
100
1·1
1·3
1·5
1·7
1·9
2·1
2·3
$M^2_{p\pi^+}$ in Gev^2
350
300
250
200
150
100
50
·05
0·15
0·25
0·35
0·45
0·55
$M^2_{\pi^+\pi^0}$ in Gev^2

Fig. 5·4

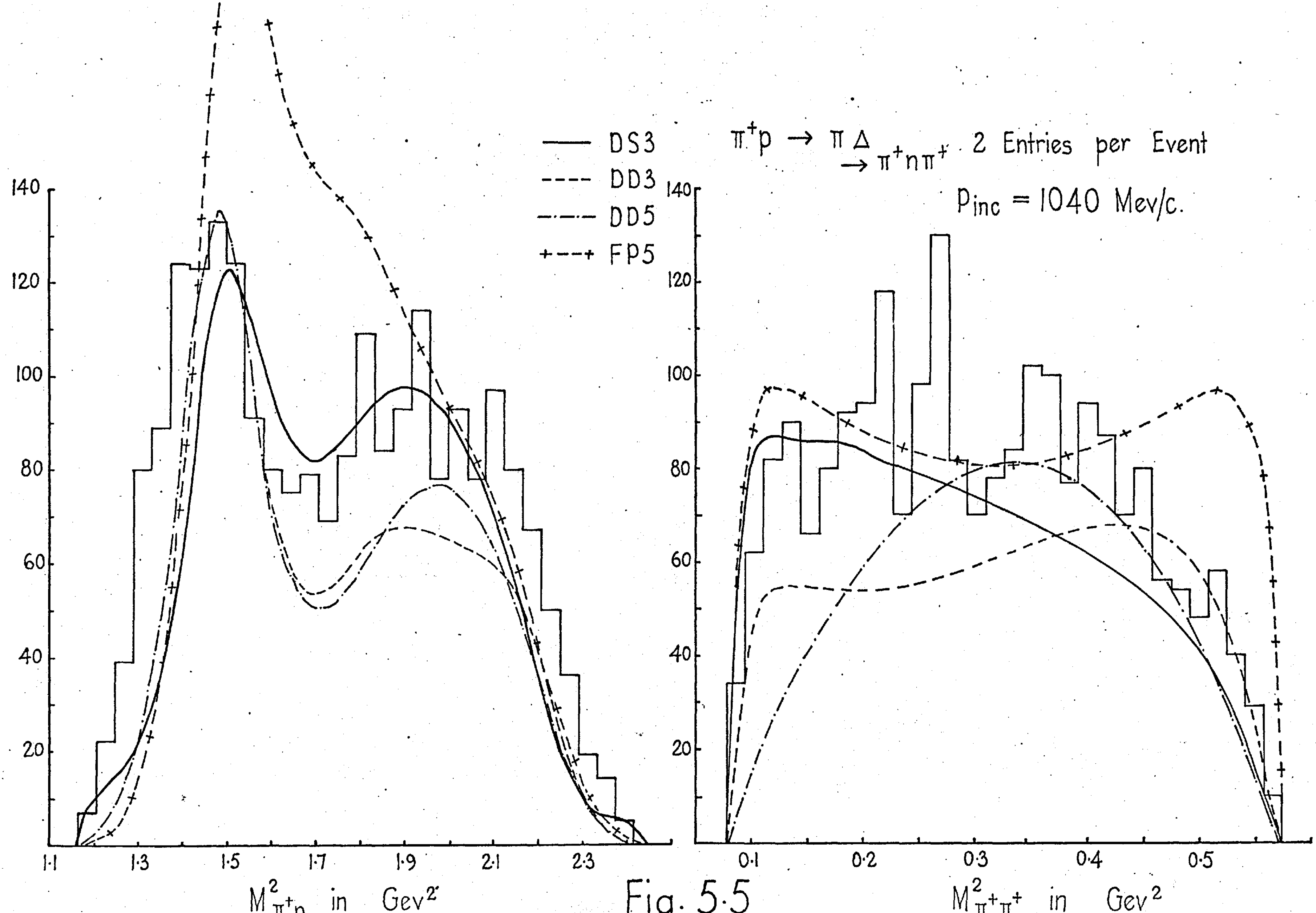

DS3
DD3
DD5
FP5
π⁺p → π Δ → π⁺nπ⁺ 2 Entries per Event
p_inc = 1040 Mev/c.
140
120
100
80
60
40
20
1·1
1·3
1·5
1·7
1·9
2·1
2·3
M²π⁺n in Gev²
0·1
0·2
0·3
0·4
0·5
M²π⁺π⁺ in Gev²

Fig. 5·5

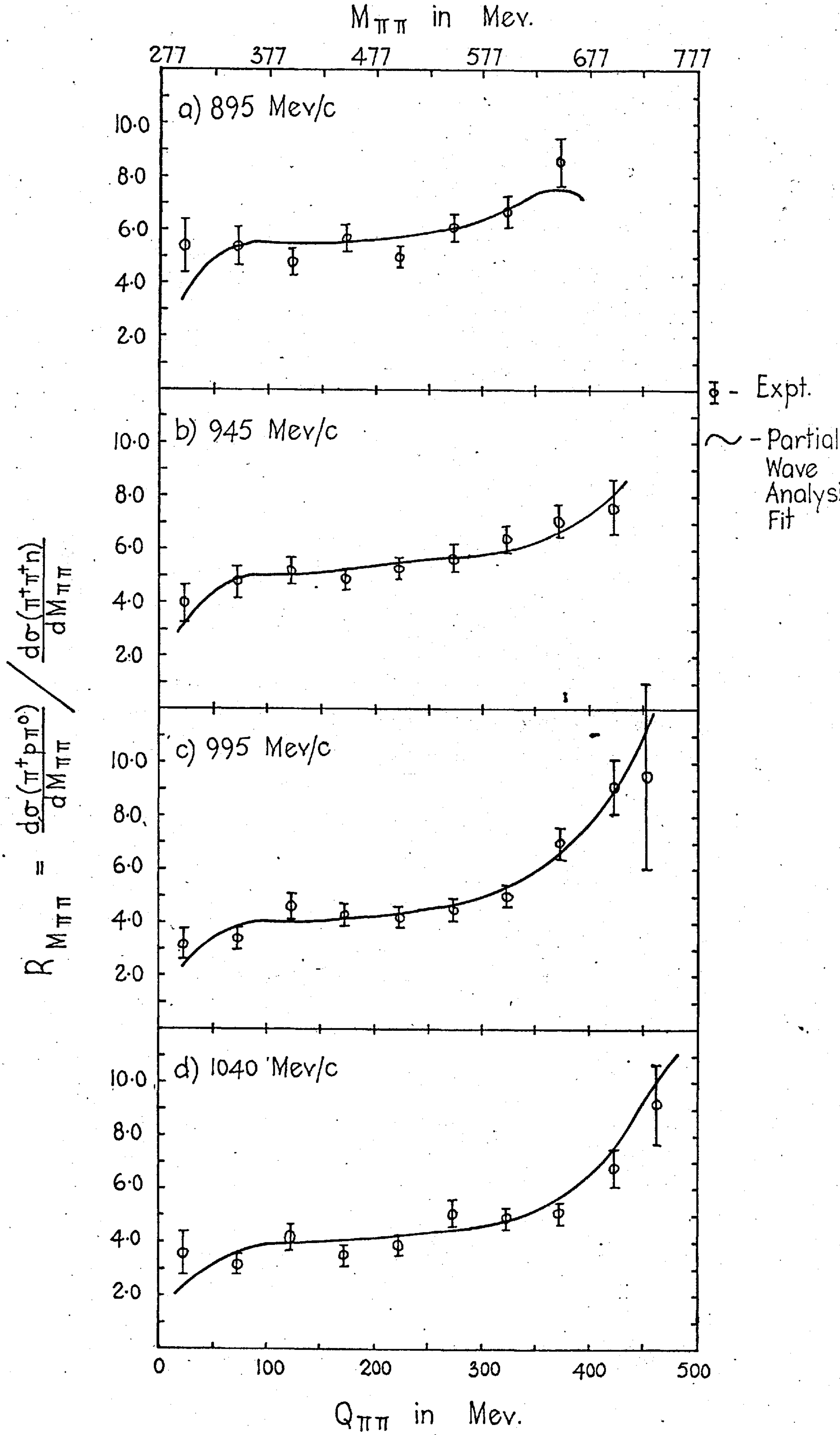

M_ππ in Mev.
277 377 477 577 677 777
a) 895 Mev/c
b) 945 Mev/c
c) 995 Mev/c
d) 1040 Mev/c
10·0
8·0
6·0
4·0
2·0
R_Mππ = dσ(π⁺pπ⁰)/dMππ / dσ(π⁺π⁺n)/dMππ
- Expt.
- Partial Wave Analysis Fit
0 100 200 300 400 500
Q_ππ in Mev.

Fig. 5·6

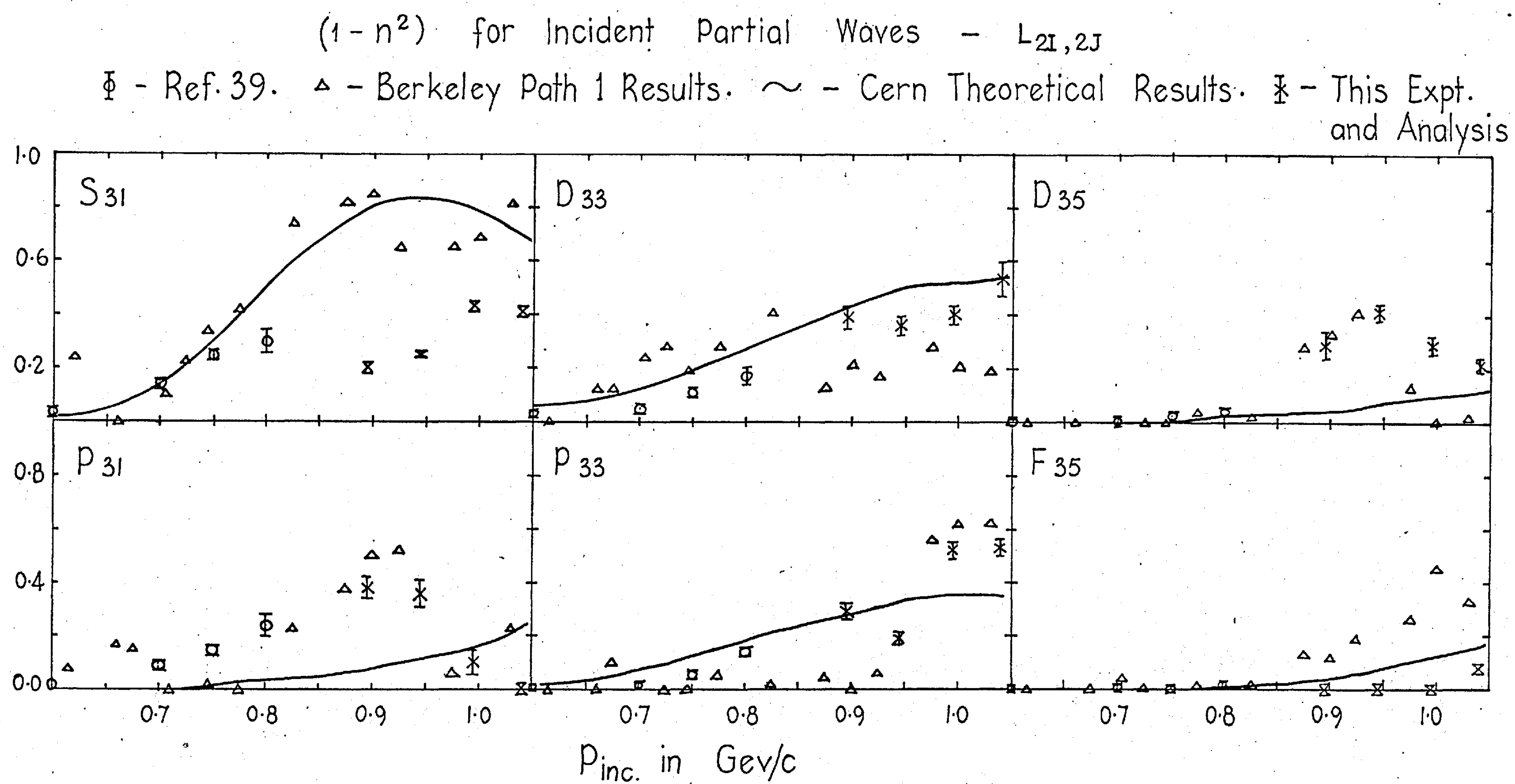
(1 - n²) for Incident Partial Waves - L2I,2J
Φ - Ref. 39. △ - Berkeley Path 1 Results. ~ - Cern Theoretical Results. X - This Expt. and Analysis
S 31
D 33
D 35
P 31
P 33
F 35
1.0
0.6
0.2
0.8
0.4
0.0
0.7
0.8
0.9
1.0
Pinc. in Gev/c

Fig. 5.7

References

1) D.P. Jones - Lecture Notes on Elementary Scattering Theory - RHEL/R108.

2) M. Ferro-Luzzi - CERN School 1968 - CERN 68 - 23 - Vol. II.

3) R.D. Tripp - Baryon Resonances - CERN 65 - 7 (Rev.)

4) L.D. Roper et al. - Phys. Rev. 138, B190 ('65).

5) J.S. Ball and W.R. Frazer - Phys. Rev. Lett. 7, 204 ('61).

6) A. Donnachie et al. - Phys. Lett. 26B, 161 ('68).
C. Lovelace - Rapporteur's talk - Heidelberg Conference 1967.
C. Lovelace - TH838 - CERN.

7) P. Bareyere et al. - Phys. Lett. 18 ('65), 342.
- Phys. Rev. 165 ('68), 1730.

8) C. H. Johnson and H.M. Steiner - UCRL 18001.
C. H. Johnson - Ph.D Thesis - UCRL 17683 ('67).

9) A.T. Davies and R.G. Moorhouse - Paper 925 at Vienna Conference 1968.

10) A. Donnachie - Scottish Universities Summer School - 1966.

11) C. Lovelace and A. Donnachie - TH 1055 - CERN.

12) S.J. Lindenbaum and R.J. Sternheimer - Phys. Rev. 109, 173 ('58)
- Phys. Rev. 123, 333 ('61).

13) S. Bergia et al. - Nuo. Cim. 16, 1073 ('60).

14) M. Olsson and G.V. Yodh - Phys. Rev. Lett. 10, 353 ('63).

15) S. Ciuli and J. Fischer - Nuo. Cim. 12, 1179, ('59).

16) M. Olsson and G.V. Yodh - Phys. Rev. 145, 1309 ('66).

17) M. Olsson and G.V. Yodh - Phys. Rev. 145, 1327 ('66).

18) J.M. Namyslowski et al. - Phys. Rev. 157, 1328 ('67).

19) G.C. Wick - Ann. Phys. 18, 65 ('62).

20) B. Deler and G. Valladas - Nuo. Cim. 45, 559 ('66).

21) P.J. Duke et al. - Phys. Rev. 149, 1077 ('66).
J.A. Helland et al. - Phys. Rev. 134B, 1062 ('64).

22) P. Newcomb - Phys. Rev. 132, 1283 ('63)
R. Barloutaud et al. - Nuo. Cim. 27, 238 ('63).
J. Kirz et al. - Phys. Rev. 126, 763 ('62).

23) CERN TC Program Library - THRESH Write-up.

24) K. Soop - Progress in Nuclear Technique and Instrumentation - Vol II
North - Holland Publishing Company.

25) CERN TC Program Library - GRIND Write-up.

26) A.A. Carter et al. - Phys. Rev. 168, 1457 ('68).

27) G. Giacomelli et al. - Stonybrook Conference 1966.

28) P. Bareyere et al. - Situation experimentale de la diffusion elastique π-nucleon en dessons de 2 GeV - Saclay Report CEA - R3401

G. Giacomelli et al.- Compilation of pion-nucleon scattering data - CERN - HERA - 69 - 1.

29) S.L. Baker et al. - Nuc. Phys. B18, 29 ('70).

30) J.A. Helland et al. - Phys. Rev. 134B, 1062 ('64).

31) P. Duke et al. - Phys. Rev. 149, 1077 ('66).

32) W.J. Metzger et al. - Phys. Rev. 164, 1680 ('67).

33) C. Tilger et al. - Phys. Rev. 142, 972 ('66).

34) J. Debaiseiux et al. - Nuc. Phys. B5, 147 ('68).

35) R.M. Heinz and H.M. Ross - Phys. Rev. Lett. 14, 1091 ('65).

36) S.W. Kormanyos et al. - Phys. Rev. Lett. 16, 709 ('66).

37) Barger and Cline - Phys. Rev. Lett. 16, 913 ('66).
- Phys. Rev. Lett. May '66, 828.

38) R. L. Rosenberg and L. D. Roper - Pion-proton Inelastic Data.
L.R.L. Internal Report - May '65

39) M. Bowler and R. Cashmore - Rutherford Laboratory Preprint - RPP/H/59.

40) M. Olsson - Ph.D Thesis - University of Maryland Technical Report 379.

41) J.D. Jackson - Nuo. Cim. 34 N.6, 1644 ('64).

42) S. Glashow and A.H. Rosenfeld - Phys. Rev. Lett. 10, 192 ('63).

43) L. Stodolsky and J.J. Sakurai - Phys. Rev. Lett. 11, 90 ('63).

44) B. Kehoe - Phys. Rev. Lett. 11, 93 ('66).

45) L. Stodolsky - Ph.D. Thesis - University of Chicago.

46) G. Tautfest and R. Willman - Purdue University Preprint COO - 1428 - 14

47) H.L. Kraybill et al. - Phys. Rev. Lett. 16, 863 ('66).

48) M. DeBeer et al. - Partial Wave Analysis of πN $\pi\pi$N below 1 GeV I and II - Saclay Preprints - April 1969.

49) M. Jacob and G.C. Wick - Ann. Phys. 7, 404, ('59).

50) CERN 6600 Program Library - MINUIT Write-up - D506.

51) D.J. Hendern et al. - πN Partial Wave Amplitudes - UCRL - 20030 ('70).

ACKNOWLEDGEMENTS

A high statistics bubble chamber experiment requires the continuous co-operation of a large number of people for a long period. I am extremely grateful to the members of the Imperial College Bubble Chamber Group for their diligent efforts.

The experimental processing was done in collaboration with Westfield College, London. I thank my colleagues in Westfield College and their scanning and measuring staff for their efforts.

I am particularly indebted to Dr. S.L. Baker for his continuous guidance and help throughout the course of this work. Thanks are due to Dr. R. Migneron whose contribution to the final analysis was invaluable. I am also grateful to Mr. A. Jamdagni for his efforts in debugging and running the final fitting program. I am obliged to Mr. G.J. Webster for his help in processing the Imperial College part of the experiment and to Dr. P.J. Dornan for useful discussions on the analysis.

I am indebted to Mrs. M.E. Robertson for her patient and skillful typing of this thesis and to Mr. H.S. Panesar for his efforts in producing the drawings for this thesis.

I would like to thank Professor C.C. Butler for the opportunity to carry out this research in the pleasant atmosphere of the Imperial College High Energy Nuclear Physics Group.

Finally, I wish to thank the Association of Commonwealth Universities for their financial support.